Università degli Studi di Salerno

DIPARTIMENTO DI FISICA "E.R. CAIANIELLO"

DOCTOR OF PHILOSOPHY IN PHYSICS

XIV CICLO, II SERIE

INFLUENCE OF GRAINS ON THE ELECTROMAGNETIC AC RESPONSE OF SUPERCONDUCTING MATERIALS

Davide Mancusi

TUTOR

Prof. Massimiliano Polichetti

COORDINATORE

Prof. Canio Noce

ANNO ACCADEMICO 2014/2015

Index

Introduction

After the discovering of the high critical temperature superconductors (HTS), many efforts have been dedicated to investigate their superconducting properties in order to understand the superconductivity mechanisms and to improve their electrical and magnetic properties for technological applications. Since HTS are type II superconductors, one of the most their crucial parameters in applications is the critical current density. In fact, magnetic flux penetrates this kind of superconducting materials in the form of quantized vortices which, in absence of impurities inside the material, form a periodic lattice. These vortices move in the presence of a current through the superconductor causing dissipation, and this limits the critical current density of the superconductor which is determined by the pinning of vortices.

One largely investigated issue has been the electromagnetic granularity of HTS which are in general not a homogeneous continuum but rather consist of a network of superconducting grains with intergranular weak links. The investigation of both the mechanisms of current flowing in the regions between adjacent grains and of vortex pinning inside the sample is useful in order to understand whether the superconductivity is a bulk or granular phenomenon, to separate the effects of the external parameters on the superconducting properties and flux dynamics of both the inter- and intragranular components, and to improve the fabrication processes for the application perspectives of these materials.

Two main families of materials belong to the class of high HTS, differing in some superconducting parameters and both exhibiting a layered crystal structure in which the superconductivity can become a two-dimensional phenomenon achieving high transition temperatures and unconventional order mechanisms. The first family of materials are the cuprate superconductors, whose crystal structure is composed by CuO_2 planes and spacer layers, with T_c as high as 134 K for the $HgBa_2Ca_2Cu_3O_8$ superconductor. The other popular group of layered HTS is family of the iron-based compounds, composed by a common block of FeX layers (where X = As, P, S, Se, or Te) and spacer layers, with T_c as high as 56 K for the $LnFeAsO_{1-x}F_x$ superconductor.

In particular, thermal fluctuations are very important in HTS due to the extreme material parameters characterizing these systems such as the large superconducting critical temperature T_c, resistivity ρ, and penetration depth λ, and the small coherence length ξ and Fermi velocity v_F, in addition to the uniaxial anisotropy due to the layered structure which strongly depends on the stacking composition. In fact, all these parameters increase the strength of the thermal disorder (Ginzburg number $G_i \sim 10^{-2}$) and quantum disorder that oppose the quenched disorder potential producing the pinning. Due

to the thermal motion of vortices, the disorder potential is sampled over an extended region by the vortex normal core, and then it results averaged and smoothed. This thermal depinning produces the reduction of the critical currents density j_c in the system, and affects both the field-temperature (H-T) phase diagram and the dynamical properties of vortices.

In particular, the more recently Fe-based superconducting materials are potentially very useful for applications, especially since their properties induce large thermal fluctuations and depressed grain boundary superconductivity. On the other hand, their order parameter symmetry is supposed to be *s*-wave, which is not as detrimental to current flowing across grain boundaries. Moreover, due to a high degree of quenched disorder, which corresponds to a high density of pinning centers, in Fe-based superconductors the thermally activated processes are the leading mechanisms driving the dynamic relaxation of the magnetic flux.

In this thesis, the investigation, by means of the magnetic complex susceptibility measurement, of the mechanisms of magnetic field penetration and the thermally activated flux dynamical regimes in Fe-based superconductors in presence of a time dependent magnetic field, will be treated. In fact, the inductive technique of AC susceptibility measurement is largely used to study the magnetic field distribution inside HTS and to investigate the flux dynamical regimes governing the AC magnetic response of these materials by accessing regions of the electrical field-current density characteristic which are not accessible by means of electrical transport measurements.

Most commonly, the fundamental harmonic of the AC susceptibility is measured as function of the temperature and, by considering its variations due to the external parameters, several superconducting parameters are extracted. On the other hand, the study of the AC susceptibility higher harmonics, which there exist in the AC magnetic response of the sample in the case of nonlinear magnetic response, can be used to extract information about the actual flux dynamical regimes of superconducting vortices. In particular, the third harmonic components of the AC susceptibility are the most widely investigated since their intensity is the highest and easily detectable, even in the absence of a DC field, after the fundamental harmonic components.

However, when considering granular superconducting systems, the magnetic interaction between the -inter and intragranular currents via demagnetizing effects could produce the existence of effective magnetic fields which are different from the applied field. This may affect the sample magnetic response and then the measured critical current density and pinning energy. Moreover, since in the AC magnetic response of a granular system is given by two contributions due to the superconducting grains and to the system of weak links interconnecting the grains, respectively, the investigation of

these two contributions is not always possible depending on their merging. In fact, some portions of the first and higher harmonics of the inter- and intragranular AC susceptibilities can be not accessible.

In this context, it will be proposed in this thesis an approach for analyzing the AC magnetic response of superconducting granular systems, measured by means of the AC susceptibility technique, taking into account the existence of demagnetizing effects. Since this method give also the possibility of separate the inter- and intragranular magnetic contributions to the sample response and the corresponding AC susceptibilities, it will be used to analyze the inter- and intragranular AC susceptibilities and extract several superconducting properties and flux dynamics information.

At this purpose, a description of the superconducting properties and vortex dynamics in the high-T_c superconductors will be first given in the Chapter I. Then, a detailed description of the complex susceptibility technique as tool for the investigation of the superconducting properties of HTS will be treated in the Chapter II. As an example, the method of estimation of the superconducting parameters and the extraction of flux dynamical information from the AC susceptibility of a homogeneous superconducting sample will be shown in the Chapter III. In particular, a bismuth-oxysulfide layered compound $Bi_4O_4S_3$ will be considered, which exhibits some characteristics of superconductivity mechanisms similar to cuprates and Fe-based compounds and then is designed to provide additional information for the comprehension of superconductivity in these compounds.

Beyond this preliminary description, the case of a granular system will be introduced in the following chapters. In particular, in the Chapter IV we will introduce a model, which takes into account the existence of effective magnetic fields at the whole sample's and grains's surfaces due to the demagnetizing factors of both the sample and the grains geometry, for the description of the measured AC magnetic response of a granular sample in terms of the inter- and intragranular AC magnetic contributions. Moreover, we will formulate an analytical method, for analyzing the sample magnetic response, consisting in the solution of a system of self-consistent "magnetization-field" equations which determine the AC susceptibilities harmonics of the inter- and intragranular volume fractions starting from the harmonics of the measured whole sample magnetization. This method will be used to analyze the AC magnetic response of a $FeSe_{0.5}Te_{0.5}$ sample exhibiting electromagnetic granularity and to obtain the inter- and intragranular superconducting parameters and investigate the corresponding flux dynamics mechanisms.

.

Chapter I
Vortex dynamics in type II superconductors

Two class of superconducting materials are distinguished as type-I and type II superconductors in terms of their magnetic and carrying-current properties. In fact, while the critical current density of the type-I superconductors is a consequence of the critical magnetic field H_c, which is low and then gives likewise low critical current densities j_c, the critical current is no longer simply related to the magnetic field in the type II superconductors. In fact, when a type II superconductor is in a magnetic field exceeding a value referred to as the lower critical field, H_{c1}, magnetic flux is able to penetrate in quantized units by forming cylindrically symmetric domains called vortices with elemental flux quantum ϕ_0. The flux tube diameter is approximately twice the coherence length, ξ , and at the core of the flux tube the material has reverted back to its normal non-superconducting state. For much higher applied fields the vortices tend to overlap and the field inside the superconductor becomes strong everywhere causing the transition to the normal state above the upper critical field H_{c2}[1-3].

The magnetic phase diagram for a conventional type II superconductor is shown in Fig.1a. In the mixed state the normal phase is confined to small local areas while it is still present a superconducting path through the material for the current to pass unimpeded as long as it does not disrupt the flux vortices. In fact, the mixed phase is still superconducting due to the existence of defects in the crystalline lattice which act as to pin the flux lines and prevent their motion. When the lattice starts to be free to deform, the flux lines are able to move then reducing the superconducting critical current density.

The flux lines in conventional II superconductors are considered to be rigid tubes with a mutual repulsion which tends to keep them apart. As the applied field is increased, they are forced closer together, and the state that minimizes the total free energy of the system is called an Abrikosov lattice[4], consisting in a two-dimensional hexagonal close-packed lattice. However, the lattice remains relatively well pinned and the material exhibit good superconducting properties.

On the other hand, different families of type II superconductors have been discovered and largely investigated, exhibiting a relatively high critical temperature and interesting superconducting properties. In fact, the magnetic phase diagram for these high-T_c superconductors (HTS) differs from that for the conventional superconductors in the existence of a melting transition of the Abrikosov lattice into a flux liquid phase, as shown in the Fig. 1b. The transition line is also named irreversible line since on the lower side of this line the magnetic behavior of the superconductor is reversible while it

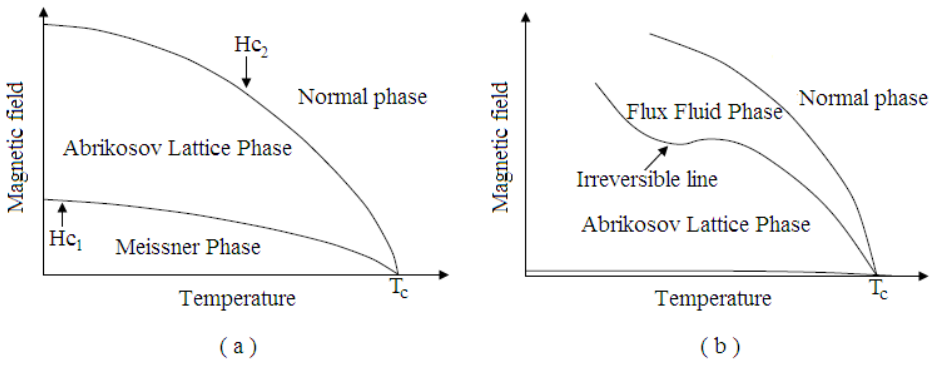

Figure 1. Magnetic phase diagram of (a) conventional and (b) high-T_c type II superconductors.

becomes irreversible above the line. Such melting transition is favorable in high-T_c superconductors due to the higher temperature involved, and highly affects the critical current density.

The first kind of discovered high-T_c superconducting materials were the Cu-oxide superconductors whose crystal structure is composed by CuO_2 planes and spacer layers. These cuprate superconductors have the highest critical temperature T_c observed up to now. In fact, after the discovery of the first high-T_c superconductors by Berdnoz and Muller in 1986, a large growth of the research and development activities in the field of the superconductivity started, which leaded to the highest critical temperature superconductivity observe for the $HgBa_2Ca_2Cu_3O_8$ compound[5-9]. In addition to the high values of the critical temperature T_c, extreme material parameters characterize these systems such as the large resistivity ρ and penetration depth λ, and the small coherence length ξ and Fermi velocity v_F, in addition to the uniaxial anisotropy due to their layered structure. In fact, all these parameters increase the strength of the thermal disorder (Ginzburg number $G_i \sim 10^{-2}$) and quantum disorder that oppose the quenched disorder potential producing the pinning[10]. Due to the thermal motion of vortices the disorder potential is sampled over an extended region by the vortex normal core resulting in an averaged potential and then in a smoothing of the disorder potential. This thermal depinning reduces the critical currents density j_c, and affects both the field-temperature (H-T) phase diagram and the dynamical propertied of vortices.

The other family of unconventional type II superconductors are the Iron-based superconductors, which are composed by a common block of FeX layers (where X = As, P, S, Se, or Te) and spacer layers, with T_c as high as 56 K for the $LnFeAsO_{1-x}F_x$ compound[11-19]. This new family of type II superconductors exhibits properties both of the conventional superconductors described by the Bardeen-Cooper-Schrieffer (BCS) theory[20], such as their lower critical temperature and anisotropy, and of the HTS such

as high upper critical field and low carrier density and effective mass, giving a $G_i \sim 10^{-4}$-10^{-2} due to thermal fluctuations which are the leading mechanism as in the cuprate superconductors[10]. Moreover, like the cuprate superconductors, the critical temperature T_c depends in particular on the on the composition of the stacking structure, which makes both the kinds of systems interesting to investigate for the complete understanding of their superconductivity mechanisms.

As a peculiar common characteristic of both the cuprate and the Fe-based superconductors, thermal fluctuations influence the dynamics of the superconducting vortices in response to the external current density j which lead the vortices to move with a finite velocity by opposing to the pinning force of the material. In particular, the phenomenology of the macroscopic magnetic response of these systems in presence of an external magnetic field varying in time can be studied in terms of the dynamical regimes of the virtices thermally activated around the critical state in which the vortex motion is hindered by the pinning force. Most commonly, the analysis of the AC magnetic response is made in terms of the complex magnetic susceptibility both in presence and in absence of a magnetic DC field superimposed to the AC field. In fact, measuring the complex susceptibility with varying the external parameters such as the temperature, the amplitude and the frequency of the AC field, and the strength of the DC field, allows one to obtain both several superconducting parameters and detailed information about the flux dynamical regimes governing the AC magnetic response[21-25].

This chapter is an attempt to systematize the theoretical background concerning the dynamics of the superconducting vortices of type II superconductors when they interact with an external magnetic field. This includes the expulsion of flux due to Meissner-Ochsenfeld effect, the flux pinning by a surface barrier, the pinning of the flux entering the bulk of superconductor in the form of flux lines, the diffusion of these flux lines across the sample and the reversible motion of pinned flux lines in potential wells. In particular, the physical models of these mechanisms can be used to describe the corresponding complex susceptibility in order to relate the measured curves of the complex susceptibility to the actual electrodynamics inside the superconductors[22].

I.1 Type II superconductors in an alternate magnetic field: the diffusion equation

In order to study the magnetization process of a type II superconductor in presence of an oscillating applied magnetic field, it may be necessary to study the nonlinear diffusion-like equation which governs the spatial-temporal evolution of the local magnetic field B[22],

$$\frac{\partial^2 B(x,t)}{\partial x^2} = \frac{\mu_0}{\rho(B,E)}\frac{\partial B(x,t)}{\partial t} = \frac{1}{D(B,E)}\frac{\partial B(x,t)}{\partial t}, \quad \text{(I.1)}$$

where $\rho(B,E)$ is the electrical resistivity depending on both magnetic field B and the electrical field E, together with the approximate current-voltage characteristic[26-28]

$$j(B,E) = j_c(B)\frac{E}{|E|}\left(\frac{|E|}{E_c}\right)^{\frac{1}{n}}. \quad \text{(I.2)}$$

Here the index n allows one to model the linear diffusion of the flux lines ($n = 1$), the critical state ($n = \infty$) and intermediate regime ($n > 1$). In the following, we will treat the solution of the diffusion equation in the different regimes of linearity.

I.1.1 Critical state

When the superconducting material is able to pin the flux lines into the pinning potential wells, the critical state is established. This state is obtained by setting $n = \infty$ in the Eq. (I.2), for which the flux density gradient is given by

$$\frac{\partial B}{\partial x} = \mp\mu_0 j_c(B), \quad \text{(I.3)}$$

and then the material has the critical current j_c. In fact, this regime is well described by different critical state models differing in the field dependence of the critical current density $j_c(B)$..

The Bean model[29,30] is the simplest critical state model, which assumes that wherever the current flows it has the critical value j_c and the internal field is given by $\boldsymbol{\nabla} \times \boldsymbol{B} = \mu_0 \boldsymbol{j}$. For a slab geometry of Fig. I.2a, in the case of low field B_0, one founds

$$\frac{\partial B_z(x)}{\partial x} = \mu_0 j_y(x), \quad \text{(I.4)}$$

with

$$j_y(x) = j_c\,, \quad -a \le x \le -a', \quad \text{(I.5a)}$$

$$j_y(x) = 0, \quad -a' \le x \le a', \quad \text{(I.5b)}$$

-

$$j_y(x) = -j_c, \quad a' \le x \le a, \quad \text{(I.5c)}$$

where we have considered that there is a field- and current- free region $(-a' < x < a')$. In this case, the boundary conditions for the field are

$$B_z(\pm a) = B_0, \tag{I.6a}$$

$$B_z(\pm a') = 0, \tag{I.6b}$$

with B_0 the applied field. Then, one obtains for the internal magnetic fields

$$B_z(x) = B_0\left(\frac{a'+x}{a'-a}\right), \quad -a \le x \le -a', \tag{I.7a}$$

$$B_z(x) = 0, \quad -a' \le x \le a, \tag{I.7b}$$

$$B_z(x) = B_0\left(\frac{x-a'}{a-a'}\right), \quad -a' \le x \le a, \tag{I.7c}$$

and the critical current density is give by

$$j_c = \frac{B_0}{\mu_0(a-a')}. \tag{I.8}$$

In the study of the high field case one defines the characteristic field $B^* = \mu_0 j_c a$ at which the field and current penetrate the center of the sample. In fact, the low field case discussed above corresponds to $B_0 < B^*$. On the other hand, for high fields $B_0 > B^*$, the currents and fields can be found

$$j_y(x) = j_c, \quad -a \le x \le 0, \tag{I.9a}$$

$$j_y(x) = -j_c, \quad 0 \le x \le a, \tag{I.9b}$$

$$B_z(x) = B_0 - B^*\left(\frac{a+x}{a}\right), -a \le x \le 0, \tag{I.10a}$$

$$B_z(x) = B_0 + B^*\left(\frac{x-a}{a}\right), 0 \le x \le a. \tag{I.10b}$$

The Fig. I.2b shows the variation of the field and current with varying the strength of the applied field starting at zero, increasing from to a maximum value and decreasing through zero to a negative maximum value as for an AC field cycle.

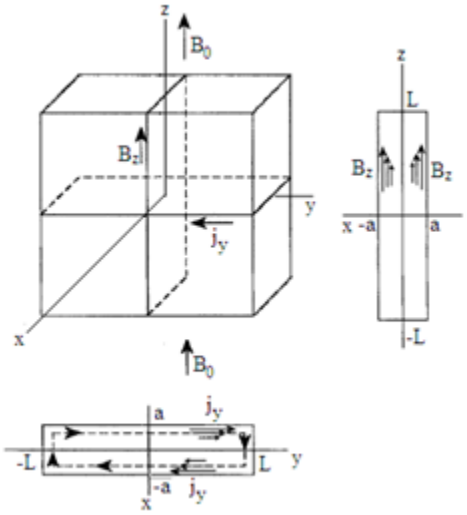

(a)

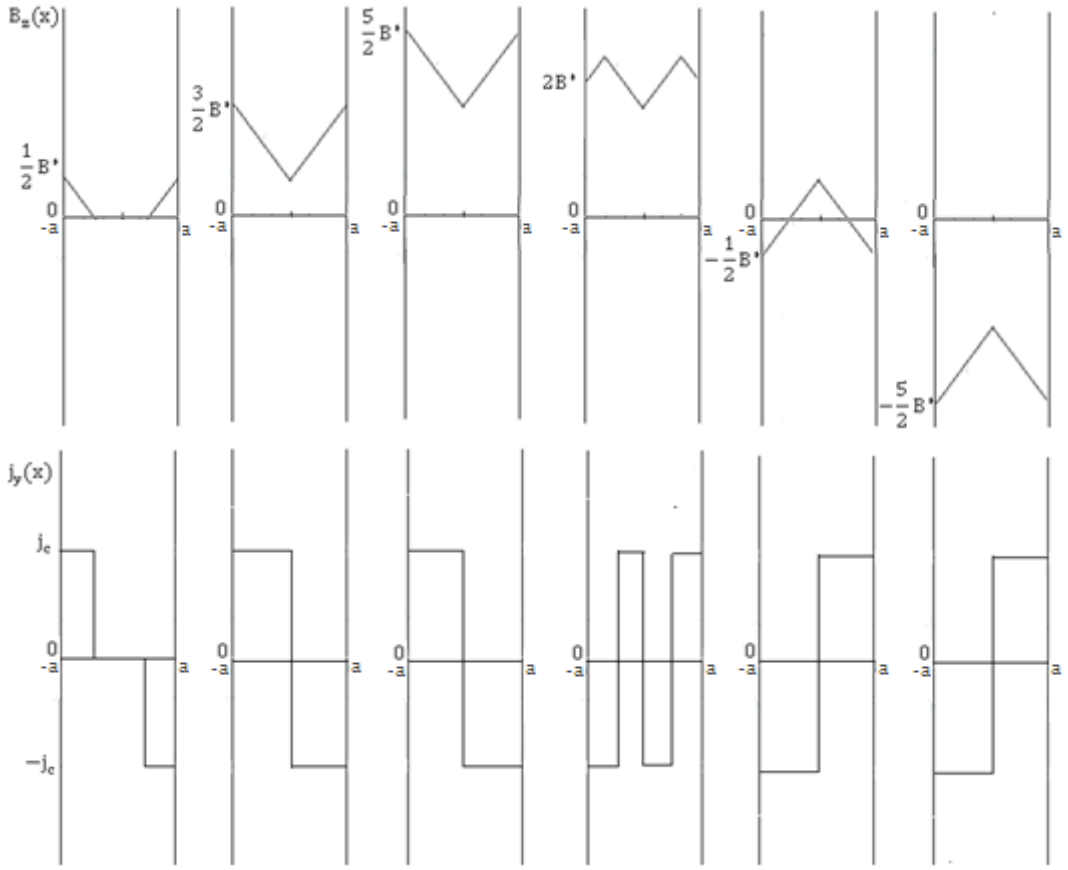

(b)

Figure I.2 (a) Superconducting slab of thickness $2a$ placed in the y, z plane, in an external magnetic field B_0 applied parallel to the z axis. This filed induces a shielding current j_y flowing around the sample in the x, y plane. (b) Schematic diagram of the magnetic field penetration and current density profiles with varying the external field.

$j = j_c$	Bean
$j = \frac{j_c}{\lvert B(x)\rvert / B_k}$	Fixed Pinning
$j = \frac{j_c}{\lvert B(x)/B_k\rvert^{1/2}}$	Square Root
$j = \frac{j_c}{1 + \lvert B(x)\rvert / B_k}$	Kim
$j = j_c e^{-\lvert B(x)\rvert / B_k}$	Exponential
$j = j_c - j_c{}' \lvert B(x)\rvert / B_k$	Linear
$j = \frac{j_c}{1 + [\lvert B(x)\rvert / B_k]^2}$	Quadratic
$j = j_c \left[1 - \frac{\lvert B(x)\rvert}{B_k}\right] \Theta[\lvert B\rvert - B_k]$	Triangular

Table I.1 Current-field relationship for different critical state models.

Unlike the Bean critical state model, more complex relationships between the internal field and the current density are assumed within the other critical state models. Typically, these relationships for the slab geometry are of the form

$$j_y(B_z) = \frac{j_k}{f(B_z)}, \tag{I.11}$$

where j_k is independent of the field and in most models corresponds to the critical value of the current density in the absence of the applied field, and $f(B_z)$ is a function of the magnetic field[3]. These relationships are reported in the Table I.1 for several critical state models. In fact, by substituting these current-field characteristics into Eq. (I.3) gives a differential equation whose solution is the corresponding spatial profile of the internal field $B(x)$.

I.1.2 Intermediate state

For finite values of n greater than 1 into the Eq. (I.2), intermediate regimes occur in type II superconductors. An example of this behavior is the flux creep (fc) regime, which is especially found in HTS since high temperature and low pinning are involved. In fact, this regime is met when in the sample, originally into the critical state, the flux lines start to be hopping over the pinning wells to reach metastable states with lower energy. The creep phenomenon was introduced by Anderson and Kim[31], where it is assumed that flux creep occurs by bundles of flux lines with a jump rate taken of the form

$$\nu = \nu_0 e^{-\frac{U_0}{k_B T}}, \tag{I.12}$$

where ν_0 is an attempt frequency and U_0 is the unperturbed pinning barrier energy. If the hopping rates are the same in both directions, there is no net motion of the flux lines. On the other hand, when a flux gradient is present an energy contribution U_L due to the action of the Lorentz force has to be taken into account which makes the pinning potential a washboard potential. This produce two different hopping rates in the forward and backward directions,

$$\nu_f = \nu_0 e^{-\frac{U_0 - U_L}{k_B T}}, \tag{I.13c}$$

$$\nu_b = \nu_0 e^{-\frac{U_0 + U_L}{k_B T}}, \tag{I.13b}$$

where

$$U_L = f_L V_c r_p, \tag{I.14}$$

with $f_L = (1/c)jB$ the Lorentz force density, V_c the volume of the flux bundles moving independently from the other ones, r_p the range of the pinning potential.
Then, the net hopping rate is given by

$$\nu = \nu_f - \nu_b = 2\nu_0 e^{-\frac{U_0}{k_B T}} \sinh\left[\frac{U_L}{k_B T}\right], \tag{I.15}$$

Such creep phenomenon occur at low temperature where flux pinning plays an important role, i.e. $U_0 \gg k_B T$ and $U_0(j/j_c) \gg k_B T$. In this case, a thermally activated very slow motion of the flux lines is established with a velocity from the Eq. (I.4)

$$\nu_{fc} = \nu_0 e^{-\frac{U_0[1-(j/j_{c0})]}{k_B T}}, \tag{I.16}$$

where the effective flux creep barrier energy has been assumed to be of the form $U_0[1-(j/j_c)]$ with j_c the critical current density in absence of creep. On decreasing the exponent n in the Eq. (I.2) one can model situations with increasing importance of the flux creep.

I.1.3 Linear diffusion

Setting $n = 1$ in the equation (I.2) yields the linear current-voltage characteristic

$$j(B,E) = j_c(B)\frac{E}{|E|}\left(\frac{|E|}{E_c}\right). \quad \text{(I.17)}$$

Inserting this linear current into the diffusion equation (I.1), converts it in a linear differential equation which solution is an AC magnetic flux profile decaying exponentially inside the superconductor, i.e.

$$B(x) = B_0 \exp[-x/\delta]. \quad \text{(I.18)}$$

Here the characteristic length scale is given by

$$\delta = (2D/\omega)^{1/2}, \quad \text{(I.19)}$$

and then it depends on both the frequency ω of the AC magnetic field, and on the magnetic diffusivity D of the material.

Flux dynamical regimes belonging to this linear behavior are normal-state eddy currents, linear flux flow and thermally assisted flux flow, differing in the value of the linear resistivity. In fact, in the range of temperature near T_c or for driving current densities well below the critical current density j_c, the magnetic flux penetration in form of flux lines inside the sample is due to the thermally assisted flux flow (taff) regime. For $j \ll j_c$ and $U_L \ll k_B T$ in the Eq. (I.15), the taff velocity is given by

$$v_{taff} = 2v_0\left(\frac{U_0}{k_B T}\right)\left(\frac{j}{j_c}\right)e^{-\frac{U_0}{k_B T}}. \quad \text{(I.20)}$$

When the Lorentz force density f_L exceeds the pinning force f_p, the flux lines lattice (FLL) starts to move as a whole with the flux-flow viscous velocity

$$v_{ff} = v_n\frac{B}{B_{c2}} \quad \text{(I.21)}$$

where v_n is the flux lines velocity in the normal state and B_{c2} is the superconducting upper critical field . In the Eq. (I.21) a generalized temperature dependence of the high-temperature limit velocity v_n may be considered corresponding to the normal resistivity $\rho_n(T) = (\rho_0 + \alpha T + \beta T^2)$, since a linear trend is typically observed at temperatures not

much higher than T_c, while a faster dependence can occur at higher temperatures, both in high-*Tc* and Fe-based superconductors[33-36]. This vortex motion corresponds to the electrical field $\boldsymbol{E} = \boldsymbol{B} \times \boldsymbol{v_{ff}}$ giving the finite resistivity

$$\rho_{ff} = \rho_n \frac{B}{B_{c2}} \tag{I.22}$$

which is the normal state resistivity ρ_n modulated by the ratio between the flux gradient and the upper critical field B_{c2}. In fact, the magnetic field tends to reach the upper critical field due both to the temperature decreasing of the upper critical field with increasing temperature and to the filed strength. Then, since ρ_n corresponds to the high-temperature limit value of the resistivity, it follows that $\nu_0 = \nu_n$ in the creep velocity (I.16) and taff velocity (I.20).

I.2 Pinning mechanisms in type II superconductors

In the previous paragraph we have analyzed the different solutions of the diffusion equation corresponding to the different regimes of flux dynamics. We have seen that motion of the flux lines in the mixed state of type II superconductors is hindered by the inhomogeneities of the material, which act as pinning centers since they change the energy of the flux lines. In fact, when this pinning force holds the flux lines in particularly favorable positions within the underlying material, the system is able to sustain the Lorentz force between the external magnetic field and the currents without flux motion and dissipation.

However, since in HTS thermally activated depinning and flux motion are pronounced, the intrinsic pinning of the material is less efficient than in the classical superconductors. Then, it is very crucial to investigate the nature of the pinning mechanisms in order to improve to raise the pinning strength and the critical current density.

In this paragraph we shall give a detailed description of the pinning mechanisms in type II-superconductors, with special reference to HTS. Most attention will be given to the collective pinning model of Larkin and Ovchinnikov[37-38], which is the most appropriate model for describing the pinning effects by randomly distributed weak point defects. However, also other pinning models will be treated which are appropriate to describe the effect of strong and correlated defects.

I.2.1 Larkin-Ovchinnikov theory of collective pinning

Once one allows for the elasticity of the flux lines lattice, individual flux lines can deviate their path from the ideal Abrikosov lattice to lower their energy by passing through favorable pinning sites. However, this occurs at the expense of increasing the elastic energy of the flux lines due to their deformation, and the equilibrium configuration is established by minimizing the pinning and elastic energies.

In order to obtain a prescription for estimating the critical current density resulting from a random distribution of weak point pinning centers in HTS, both the elastic properties and the thermal activated processes have to be taken into account. Although by definition, the activation energy for the flux motion has been taken $U_0[1-(j/j_c)]$, such form is not always appropriate in the practice. In fact, the classical flux creep theory discussed in the previous paragraph may to be generalized by taking into account more carefully the current dependence of the activation energy.

In this treatment we consider the case of flux density low enough and current density high enough to neglect the vortex-vortex interaction and to consider thermal activation of a single flux line, which is valid apply to the regime of small fields and temperature. One can start from the problem of a single vortex line of length Ldirected along the z axis and in the presence of a weak random pinning potential ε_{pin}. The vortex line is subject to the Lorentz force $f_L = (1/c)\boldsymbol{j}\times\boldsymbol{B}$ and the free energy density of the vortex is given by[1,10]

$$\mathcal{F}(\boldsymbol{u}) = \int dz \;\; \frac{\varepsilon_l}{2}\left[\left(\frac{\partial \boldsymbol{u}}{\partial x}\right)^2 + \varepsilon_{pin}(z,\boldsymbol{u}) - \boldsymbol{f_L}\cdot\boldsymbol{u}\right], \tag{I.23}$$

where $\boldsymbol{u}(z)$ is the displacement of the vortex and ε_l the vortex elasticity. A correlation function characterizing the random pinning potential can be introduced[1,10],

$$\left\langle \varepsilon_{pin}(z,\boldsymbol{u}) \middle| \varepsilon_{pin}(z',\boldsymbol{u}') \right\rangle, \tag{I.24}$$

which depends on the nature of the disorder. In fact, for extended pinning centers the pinning potential is correlated over the defects size r_p and the correlation function (I.24) decays along the r_p scale. On the other hand, when considering pinning point defects which perturb the superconductivity on a scale smaller than the coherence length ξ, the scale length for the correlation function can be assumed to be zero along the vortex and the smallest transverse scale length is $r_p \sim \xi$.

The basic idea of the collective pinning theory is to describe the FLL as a system of c0rrelation volumes within which the vortex line are pinning independently. In fact, in type II superconductors pinning results from spatial variations of the

Ginzburg-Landau (GL) coefficient due to both disorder in the transition temperature T, and/or from spatial variations in the charge carrier mean free path l near lattice defects. These two kinds of pinning are usually called δT_c pinning and δl pinning. In fact, in δT_c pinning spatial variations of T_c produce spatial modulations of the linear and quadratic terms of the GL free energy $\alpha|\psi|^2 + (\beta/2)|\psi|^4$, while in δl pinning variations in the free mean path influence the $|\nabla\psi|^2$. Within both the two pinning regimes the average pinning energy can be expressed as[1,10]

$$\langle \varepsilon_{pin}^2(L)\rangle = \int dz\ dz^{'}\ \langle \varepsilon_{pin}(z,0)\varepsilon_{pin}(z^{'},0)\rangle = \gamma\xi^2 L, \tag{I.25}$$

where γ is the disorder parameter which can be described in the Ginzburg-Landau model or determined from microscopic considerations.

In order to obtain the collective pinning length above which the vortex displacement increased beyond r_p, the following expression for the free energy density can be considered[1,10],

$$\mathcal{F}(\boldsymbol{u}, L) = \varepsilon_0 \frac{u^2}{L} - \gamma\xi^2 L^{\frac{1}{2}} - j\frac{\Phi_0}{c} Lu, \tag{I.26}$$

where $\varepsilon_0 u^2/L$ is the elastic energy due to the vortex distortion $\boldsymbol{u}$, $-\sqrt{\gamma\xi^2 L}$ is the pinning energy gain, and $j(\Phi_0/c)Lu$ the Lorentz force contribution. By minimizing this energy density one obtains the collective pinning length and energy

$$L_c \sim \left(\frac{\varepsilon_0\xi^2}{\gamma}\right)^{\frac{1}{3}}, \tag{I.27a}$$

$$U_c \sim (\gamma\xi^2 L)^{\frac{1}{3}} \sim T_c \left(\frac{1-t}{Gi}\right)^{\frac{1}{2}} \frac{\xi}{L_c}, \tag{I.27b}$$

where Gi denotes the Ginzburg number measuring the importance of thermal fluctuations,

$$Gi = \frac{1}{2}\left(\frac{T_c}{H_c^2(0)\xi^3(0)}\right)^2, \tag{I.28}$$

with H_c the thermodynamic critical field. The results (I.27a) and (I.27b) apply to the case of isolated vortex, and each segment of length L_c is pinned from the defects contained in the collective pinning volume $V_c = L_c\xi$ giving a pinning potential U_c. The corresponding critical current density can be obtained by equating the pinning and Lorentz forces, thus

giving

$$j_c = j_0 \left(\frac{\xi}{L_c}\right)^2. \tag{I.29}$$

where j_0 is the depairing current density. In terms of the critical current density, the collective pinning length L_c and U_c can be expressed as

$$L_c \sim \xi \left(\frac{j_0}{j_c}\right)^{\frac{1}{3}}, \tag{I.30a}$$

$$U_c \sim H_c^2 \xi^3 \left(\frac{j_c}{j_0}\right)^{\frac{1}{3}} \sim T_c \left(\frac{1-t}{Gi}\right)^{\frac{1}{2}} \left(\frac{j_c}{j_0}\right)^{\frac{1}{3}}, \tag{I.30b}$$

In the absence of disorder, and consequently of pinning, the Eqs. (I.29), (I.30a) and (I.30b) lead to $j_c = 0$, $U_c = 0$ and $L_c = \infty$. On the other hand, in the presence of pinning, for a current density near j_c the condition that the energy gain due to the driving Lorentz force is equal to the deformation and pinning energies of the vortex is fulfilled for the neighbouring metastable state which is at a distance near to the coherence length ξ away. With decreasing j the Lorentz force is reduced and the next favorable metastable state becomes more distant. Then, the thermal motion of the vortex will involve longer hopping distances for larger segments in order to reach the next optimal low-energy state, and a quantitative analysis requires to know about the low lying metastable states for the vortex in the pinning environment. Within such kind of approach it has been found, when considering an elastic string, that competing metastable states differing on a length scale $\sim L$ along the vortex are separated by a typical distance

$$u(L) \sim u_c \left(\frac{L}{L_c}\right)^{\zeta}, L > L_c, \tag{I.31}$$

and a typical energy barrier

$$\mathcal{E}(L) = U_c \left(\frac{L}{L_c}\right)^{2\zeta-1}, L > L_c, \tag{I.32}$$

with U_c denoting the scaling parameter for the energy. The free energy functional at low driving currents $j \ll j_c$ is given by

$$\mathcal{F}(L) \sim U_c \left(\frac{L}{L_c}\right)^{2\zeta-1} - j\frac{\Phi_0}{c} L_c \xi \left(\frac{L}{L_c}\right)^{\zeta+1}, \tag{I.33}$$

where the second term is the energy gain from the Lorentz force $j\,\Phi_0/c\,Lu$ of a vortex segment distorted with an amplitude u. Moreover, we have normalize the scaling laws (I.31) and (I.32) to take the values of the coherence length ξ and U_c, respectively, at $L{\sim}L_c$, $u(L){\sim}\xi(L/L_c)^{\zeta}$ and $\mathcal{E}(L){\sim}U_c(L/L_c)^{2\zeta-1}$. From the results (I.33) the energy of the displaced flux lines first increases and then decreases with increasing L. The maximum of $\mathcal{F}(L)$, which is the barrier energy, occurs for $L{\sim}L_c(j_c/j)^{1/2-\zeta}$. Inserting this results back into the Eq. (I.33) yields the minimum barrier energy for creep

$$U(j) = U_c\left(\frac{j_c}{j}\right)^{\mu}, \tag{I.34}$$

with

$$\mu = \frac{2\zeta-1}{2-\zeta}. \tag{I.35}$$

In fact, it has been found $\zeta = 2/3$ for $n = 1$ (a vortex moving in a plane), $\zeta = 3/5$ for $n = 2$ (a vortex in three-dimensional space), corresponding to $\mu = 3/4$ and $\mu = 1/7$, respectively. For more general models, it is thought that $\mu \leq 1$[1,10].

The current dependence (I.34) of U on the current j implies a nonlinear logarithmic time decay of the current density

$$j(T){\sim}j_c\left[1 - \frac{T}{U_c}\ln\left(1 + \frac{t}{t_0}\right)\right]. \tag{I.36}$$

with the microscopic time $t_0 = \tau_0 T/j_c\left|\partial_j U\right|$. This result is not appropriate for $j \ll j_c$, and a useful interpolation formula combining the two limit expressions (I.34) and (I.36) yields

$$j(T){\sim}j_c\left[1 + \frac{\mu T}{U_c}\ln\left(1 + \frac{t}{t_0}\right)\right]^{-\frac{1}{\mu}}, \tag{I.37}$$

which differs from the (I.36) in the barrier energy U_c/μ with respect to U_c at $j \approx j_c$.

I.2.2 The vortex-glass model

The possible existence within the Larkin and Ovchinnikov theory of a vortex-glass phase transition from a vortex-fluid phase with linear resistance to a vortex-solid phase with zero resistance was proposed by Fisher *et al*.[39]. Such approach was made in terms of scaling arguments. In fact, a continuous glass transition at a temperature T_g can be

assumed at which the vortex-glass correlation length and the characteristic correlation time both diverge as

$$\xi_G = \left|T - T_g\right|^{-\nu}, \tag{I.38a}$$

$$\tau_G \sim {\xi_G}^{z}, \tag{I.38b}$$

with ν and z the exponents describing the two divergences, respectively. In order to obtain a current-voltage characteristic at the transition, Fisher *et al*. started from the assumption of a hypothesis for the scaling behavior of the electric field and the current density. In fact, from the inverse length scale of the potential vector A, the electric field $E = \partial_t A$ was expected to scale as $1/\xi_G \tau_G$ .On the other hand, the current density $j = \partial_t \mathcal{F}$ was expected to scale as ${j\xi_G}^{d-1}$ with d the system dimension. Then, the scaling ansatz

$$E \propto {\xi_G}^{-(z+1)} e_{\pm} {j\xi_G}^{d-1}, \tag{I.39}$$

where $e_{\pm}$ are scaling functions for temperature above $(+)$ and below $(-)$ the glass temperature T_g. Above T_g one expects an ohmic behavior especially at low current densities. So the function $e_+(x \longrightarrow 0)$ vanishes linearly in x. On the other hand, below T_g a glassy response $e_-(x \longrightarrow 0) \sim e^{-const\,/\mu}$ is expected at low current levels. Finally, exactly at T_g Fisher et al. predicted to accomplished the divergence by means of scaling functions $e_{\pm}(x \longrightarrow \infty) \sim x^{\alpha}$, with $\alpha = (z+1)/(d-1)$. Then, the current-voltage characteristic near the glass temperature is given by

$$E \propto j^{(z+1)/(d-1)}, \tag{I.40}$$

while one expects

$$E \propto j, \text{ for } j < j^{+}, \text{ at } T > T_g, \tag{I.41a}$$

$$E \propto e^{-\left(\frac{j_T}{j}\right)^{\mu}}, \text{ for } j < j^{-}, \text{ at } T < T_g, \tag{I.41b}$$

where j^+ and j^- are crossover current densities. In particular, the form (I.41b) goes to zero as $j \longrightarrow 0$ with nonlinear resistance, consistently with the results (I.34).

I.2.3 Giant flux creep model

Another kind of pinning model accounts of the existence of the "giant" flux creep phenomenon observed in HTS, especially in the yttrium-based materials, due to the relatively low pinning energies and the higher critical temperatures. Yeshrun and Malozemoff[40] used the early theory of flux creep of Anderson-Kim[31] to describe the irreversible line characterizing the HTS. The basic equation of their model described the magnetization relaxation. For a slab geometry in parallel field they found

$$\frac{dM}{d\ln t} = \left(\frac{aj_c}{4c}\right)\left(\frac{k_B T}{U_0}\right), \tag{I.42}$$

where U_0 is the unperturbed pinning potential. Here a phenomenological scaling form for the temperature dependence of the critical current density can be used,

$$j_c(t) = j_c(0)(1-t)^n, \tag{I.43}$$

where the exponent n typically takes the values from 1 to $5/2$ in experiments.
On the other hand, since many theories were developed to describe the field and temperature dependences of the pinning energy U_0, a general scaling form was considered by Yeshrun and Malozemoff in order to describe the form of the irreversible line in HTS. In fact, near T_c and for low fields, they use the Anderson-Kim form $U_0 = H_c^2\xi^3/8\pi$ with the clean limit Ginzburg-Landau expressions

$$H_c \sim H_{c0}(1-t), \tag{I.43a}$$

$$\xi \sim \xi_0(1-t)^{-1/2}\,, \tag{I.43b}$$

thus giving

$$U_0 \sim (1-t)^{1/2}. \tag{I.44}$$

While this usually comes out to several electronvolts for conventional type II superconductors, it was found $U_0 \sim 0.1$ eV for the high-T_c yttrium-based materials, leading to the observed giant flux creep. In this case, the thermal activation was considered in the determination of the critical current density by considering the expression

$$j_c = j_c(0)\left[1 - \frac{k_B T}{U_0}\ln\frac{Bl\Omega}{E_c}\right], \tag{I.45}$$

where B is the magnetic induction, l is the lattice distance, Ω is some oscillation frequency of the pinned vortices, and E_c is a minimum measurements voltage per meter. In fact, the logarithmic term in the Eq. (I.45) is small and thermal activation is negligible for conventional type II superconductors, while thermal activation has to be taken into account for HTS materials. Moreover, when the lattice spacing becomes smaller than the penetration depth λ, a crossover to the collective pinning occurs at a field corresponding to the area of a unit cell of the flux lines lattice $a_0 = f\xi$, and one expects the following scaling law for the pinning energy

$$U_0 \sim H_c^2 a_0^2 \xi / 8\pi f^2 \sim (1-t)^{3/2}. \tag{I.43}$$

By substituting the results (I.46) in the Eq. (I.45) gives the condition for the irreversible line and it also yield $B^{2/3} \sim (1-t)$ which explain several experimental evidences.

I.2.4 Strong pinning by sparse point defects

Whereas weak point-like pinning centers produce what is called collective pinning within which vortices move with constraints from the interaction with their neighbors so that a relatively small number of pinning centers can restrain many nearby vortices, strong pinning due to extended defects can hold individual vortices independently from the weak interaction with from other vortices. Typical examples of these extended defects are one-dimensional screw dislocations and artificially produced columnar defect structures, or two-dimensional twin boundaries and layering in anisotropic compounds[1].

In order to obtain a description of strong pinning by large point defects and the corresponding critical current density, one can start by evaluating the energy gain per unit length for a vortex at a distance R from a cavity defect with radius r and $R > r$. At lower temperatures, where each vortex is pinned by its own individual rod and $\sqrt{2\xi} < r$, the pinning energy gain is given by[1,10]

$$\varepsilon_r(R) \approx -\varepsilon_0 \ln\left[1 - \left(\frac{r}{R}\right)^2\right], \tag{I.47}$$

from which, by equating the pinning force and the Lorenz force, one obtains for the critical current density $j_c \sim j_0$.

At high temperatures, where $r_r < \sqrt{2\xi}$, the pinning energy gain can be calculated from

the reduction in the order parameter as given in the δT_c pinning if one neglects the quasiparticle scattering probability, i.e.[1,10]

$$\varepsilon_r(R) \sim \frac{H_c^2}{8\pi}\pi r^2[1-|\psi(R)|^2] \sim \frac{\varepsilon_0}{2}\frac{r^2}{R^2+2\xi^2},\ 0<R<\lambda, \tag{I.48}$$

from which

$$j_c \sim \left(\frac{r}{2\xi}\right)^2 j_0. \tag{I.49}$$

The temperature dependence of j_c reflects the temperature dependences of the depairing critical current density and the coherence length. In fact, although experimental evidence exists suggesting temperature dependences for HTS other than the Gorter-Casimir[42,43]"two fluid model" this represents an useful starting point. In this case, the temperature dependence of the depairing current is given by

$$j_0 \sim \frac{H_c(T)}{\lambda(T)} \sim \frac{\left[1-\left(\frac{T}{T_c}\right)^2\right]}{\left[1-\left(\frac{T}{T_c}\right)^4\right]^{-\frac{1}{2}}}, \tag{I.50}$$

where we have considered the two fluid model expressions of the critical field $H_c(T) \sim [1-(T/T_c)^2]$ and the London penetration depth $\lambda(T) \sim [1-(T/T_c)^4]^{-1/2}$. Then, from the Eq. (I.47), and by considering the Pippard coherence length $\xi \sim [1-(T/T_c)^2]^{-1/2}$, one obtains the following results for the critical current density,

$$j_c \sim \begin{cases} \dfrac{\left[1-\left(\frac{T}{T_c}\right)^2\right]}{\left[1-\left(\frac{T}{T_c}\right)^4\right]^{-\frac{1}{2}}}, T \le T_{r\xi} \\ \dfrac{\left[1-\left(\frac{T}{T_c}\right)^2\right]^2}{\left[1-\left(\frac{T}{T_c}\right)^4\right]^{-\frac{1}{2}}}, T > T_{r\xi} \end{cases}, \tag{I.51}$$

where the crossover temperature $T_{r\xi}$ between the two regimes is given by the condition $\sqrt{2}\xi(T_{r\xi}) = r$, that is $T_{r\xi} = T_c[1-2\,\xi^2(0)/r^2]$. Correspondingly, from the Eq. (I.48) the temperature dependence of the pinning potential derives from the temperature dependence of $\xi \sim [1-(T/T_c)^2]^{-1/2}$.

I.2.5 The Generalize Inversion Schema (GIS)

The temperature, magnetic field and current density dependence of the activation energy for thermally activated vortex motion can be determined by means of the so-called generalized inversion schema (GIS). The GIS assumes that

$$U(j,T,B) = g(T,B)f(j/j_c\,(T,B),B), \tag{I.52}$$

and

$$g(T;B) = \left[\frac{j_c(T,B)}{j_c(0,B)}\right]^p G(T). \tag{I.53}$$

Moreover, since $j_c = j_c(T,B)$ is defined by the condition $U(j_c,T,B) = 0$, one has $f(1,B) = 0$. Finally, one can set arbitrarily $g(0,B) = 1$. Since from the GIS equation (I.52) it follows that

$$U_c(j_c,T,B) = g(T,B)f(1,B) = f(1,B), \tag{I.54}$$

the function $g(T,B)$ can be also expressed as

$$\frac{U_c(T,B)}{U_c(0,B)} = \frac{g(T,B)f(1,B)}{f(1,B)} = g(T,B). \tag{I.55}$$

Both the collective pinning energy and critical current density for a pinned single vortex can be calculated from the Eqs. (I.29) and (I.30) once a theoretical model has been chosen for the disorder parameter γ, depending on the kind of pinning. In fact, for δl pinning the disorder parameter is $\gamma = \xi^{-3}$ and one obtains from the Eqs. (I.29) and (I.30)

$$j_c(t) = j_c(0)(1-t^2)^{\frac{5}{2}}(1+t^2)^{-\frac{1}{2}}, \tag{I.56a}$$

$$g(t) = 1 - t^4. \tag{I.56b}$$

On the other hand, for the δT_c pinning, with $\gamma \sim \xi$, one has

$$j_c(t) = j_c(0)(1-t^2)^{\frac{7}{6}}(1+t^2)^{\frac{5}{6}}, \tag{I.57a}$$

$$g(t) = (1-t^2)^{\frac{1}{3}}(1+t^2)^{\frac{5}{3}}. \tag{I.57b}$$

Another kind of functional temperature dependences of the collective pinning energy and critical current density for a single pinned vortex (SV) can be considered by assuming the Ginzburg-Landau temperature dependences for the thermodynamic critical field, coherence length and penetration depth, i.e.[1,10]

$$B_c \sim (1 - t^2), \tag{I.58a}$$

$$\xi \sim \left[\frac{(1+t^2)}{(1-t^2)}\right]^{\frac{1}{2}}, \tag{I.58b}$$

$$\lambda \sim (1 - t^4)^{-\frac{1}{2}}. \tag{I.58c}$$

In this case, the pinning potential is estimated as the condensation energy density $B_c^2(t)$ times the volume ξ^3, corresponding to a small pinning site of volume equal to the vortex core. Then, from the Eqs.(I.29) and (I.30) one has

$$j_c(t) = j_c(0)(1 - t^2)(1 + t^2), \tag{I.59a}$$

$$g(t) = (1 - t^2)^{\frac{1}{2}}(1 + t^2)^{-\frac{1}{2}}, \tag{I.59b}$$

which have also been found to describe the behavior of yttrium-based compounds.

I.3 Evidence of two-band superconductivity in high-T_c superconductors

In the previous paragraph of this chapter the superconducting properties and vortex dynamics of type II superconductors have been reviewed starting from the description of the interaction of the superconductors with an external magnetic field in simple terms. This allowed one to deduce the temperature and field dependences of several superconducting parameters and to describe the dynamical regimes governing the flux penetration inside superconductors.

In this paragraph we will briefly give attention on the microscopic theories of superconductivity, namely the Bardeen-Cooper-Schrioeffer (BCS) theory[20], in order to evidence some characteristic properties of high-T_c and Fe-based superconductors depending on the mechanisms of superconductivity. The BCS theory is based on the existence of an attractive interaction, mediated by the lattice vibrations, the phonons, between electrons above the Fermi sea which then becomes instable with respect to the creation of bound states of two electrons. These states, so called Cooper pairs, have

antisymmetric wafefunctions, i.e. they are bosons, with antysimmetric spin part (s-wave superconductivity) and even orbital part, or symmetric spin part (d-wave superconductivity) and odd orbital part. The new ground state is a superposition of states built up from these pairs, and an energy gap there exist in the excitation of a quasiparticle by breaking a Cooper pair. Then, this energy gap is the energy difference between the ground state of the superconductor and the energy of the lowest quasiparticle excitation.

In general, the superconducting electrons originate from multiple bands crossing the Fermi surface with different superconducting. Usually, this is smeared out due to significant interband scattering and resulting in a single effective gap. However, if the superconducting gap for different bands differ significantly, multi-gap superconductivity becomes possible. This is experimentally evidenced in the result of measurements of different parameters, such as the magnetization, transport, heat capacity and magnetic penetration depth. In fact, for both high-T_c and Fe-based superconducting compounds these results have been found not to be explained by exclusively phonon-mediated mechanisms.

In the following, a theory of magnetic properties of two-gap superconductors in the dirty limit based on a weak-coupling BCS model will be summed in order to obtain the equations for the upper critical field B_{c2} which is one of the main experimental parameters evidencing the existence of multi-gap superconductivity mechanisms.

I.3.1 Superconducting upper critical field

By solving the linearized Gor'kov[44] equations in the case of a dirty one-gap superconductors with the assumption of a model of a superconductor in which electrons interact via the weal coupling BCS model potential with a spherical Fermi surface, the temperature behaviour of the upper critical field in conventional type II superconductors has been described by Werthamer, Helfand, and Hohenberg [45] (WHH theory). Here a simple universal relation there exists between the zero temperature-value $H_{c2}(0)$, the slope $H_{c2}^{'} = dH_{c2}(T)/dT$ at the critical temperature T_c and the normal state residual resistivity ρ_n, i.e.[45, 46]

$$H_{c2}(0) = 0.69 H_{c2}^{'} T_c, \tag{I.60a}$$

$$H_{c2}^{'} = \frac{4ec k_B}{\pi} N_F \rho_n, \tag{I.60b}$$

where N_F is the density of states at the Fermi sea and e is the electron charge. According to the Eqs. (I.60a) and (I.60b), adding nonmagnetic impurities can be used to increase

H_{c2}. However, $H_{c2}(0)$ in two-gap superconductors can be significantly much higher than what follows from the Eqs. (I.60a) and (I.60b). In fact, a theory o magnetic properties of the two-gap superconductors has developed by generalizing the well-known theory developed for dirty one-gap superconductors in describing the enhancement of $H_{c2}(0)$. In order to show this, we will consider a dirty two-gap anisotropic superconductor in the simplest case of two disconnected sheets 1 and 2, corresponding to two bands with constant values of the gap Δ_1 and Δ_2.

When considering the case of negligible interband scattering rate, for which nonmagnetic impurity scattering does not affect T_c, an equation for the upper critical field H_{c2} applied parallel to the c axis can be derived having the form[46]

$$\frac{2w}{\lambda_0}\left[\ln\left(\frac{T_c}{T_{c0}}\right)+U(h)\right]\left[\ln\left(\frac{T_c}{T_{c0}}\right)+U\left(\frac{D_2}{D_1}h\right)\right]+$$
$$+\left[1-\frac{\lambda_-}{\lambda_0}\right]\left[\ln\left(\frac{T_c}{T_{c0}}\right)+U\left(\frac{D_2}{D_1}h\right)\right]+\left[1+\frac{\lambda_-}{\lambda_0}\right]\left[\ln\left(\frac{T_c}{T_{c0}}\right)+U(h)\right]=0, \quad \text{(I.61)}$$

where, D_1 and D_2 are the intraband diffusivities, $h=H_{c2}D_1/2\phi_0T$ with ϕ_0 the flux quantum,, $\lambda_\pm=\lambda_{11}\pm\lambda_{22}$ quantify the intraband superconducting coupling ($\lambda_{12}=\lambda_{21}=0$ for negligible interband scattering), $\lambda_0=\left(\lambda_-{}^2+4\lambda_{12}\lambda_{21}\right)^{1/2}$, $T_{c0}=1.14\omega_D\exp[-(\lambda_+-\lambda_0)/2w]$ with ω_D frequency, $w=\lambda_{11}\lambda_{22}-\lambda_{12}\lambda_{21}$, and $U(x)=\psi(1/2+x)-\psi(1/2)$ with $\psi(x)$ the di-gamma function. For $T\sim T_c$ the Eq. (I.61) can be expanded in small terms $\sim h$, and then, solving for H_{c2}yields

$$H_{c2}=\frac{8\phi_0(T_c-T)}{\pi^2(a_1D_1+a_2D_2)}, \quad \text{(I.62)}$$

which reduces to the result of the one-band theory for $D_1=D_2$.

The zero-temperature value $H_{c2}(0)$ can be obtained by using the asymptotic behavior of $U(x)$ for $h\to\infty$. Then, the Eq. (I.61) reduces to

$$H_{c2}(0)=\frac{\phi_0T_c}{2\gamma\sqrt{D_1D_2}}\exp\left(\frac{g}{2}\right), \quad \text{(I.63a)}$$

$$g=\left[\frac{\lambda_0{}^2}{w^2}+\ln^2\left(\frac{D_2}{D_1}\right)+2\frac{\lambda_-}{w}\ln\left(\frac{D_2}{D_1}\right)\right]^{\frac{1}{2}}-\frac{\lambda_0}{w}, \quad \text{(I.63b)}$$

which predict a significant enhancement of $H_{c2}(0)$ as compared to the Eqs. (I.60a) and (I.60b) for $D_1=D_2$.

Bibliography

[1] J. B. Ketterson and S. N. Song, Superconductivity (Cambridge: Cambridge University Press, 1999).

[2] M. Tinkham, Introduction to Superconductivity (New York: McGraw-Hill, 1996).

[3] C. P. Poole Jr, H. A. Farach and R. J. Creswick, Superconductivity (London: Acadmemic, 1995).

[4] A. A. Abrikosov, Sov. Phys. JETP, **5**, 1174 (1957).

[5] J. Z. Bednorz, K.A. Müller, Phys. B Conden. Matter, 64 (1986) 189–193.

[6] M. K. Wu et al., Phys. Rev. Lett., 58 (1987) 908–910.

[7] H. Maeda et al., Jpn. J. Appl. Phys., 27 (1988) L209–L210.

[8] A. Schilling et al., Nature, 363 (1993) 56–58.

[9] L. Gao et al., Phys. Rev. B, 50 (1994) 4260.

[10] G. Blatter et al., Rev. Mod. Phys., 66 (1994) 1125.

[11] Y. Kamihara, T. Watanabe, M. Hirano, H. Hosono, J. Am. Chem. Soc., 130 (2008) 3296.

[12] X. H. Chen et al., Nature, 453 (2008) 761–762.

[13] Z. A. Ren et al., Chinese Phys. Lett., 25 (2008) 2215.

[14] M. Rotter, M. Tegel, D. Johrendt, Phys. Rev. Lett., 101 (2008) 107006.

[15] F. C. Hsu et al., Proc. Natl. Acad. Sci. USA, 105 (2008) 14262.

[16] X. C. Wang et al., Solid State Commun., 148 (2008) 538.

[17] K. W. Yeh et al., EPL, 84 (2008) 37002. 1–4.

[18] Y. Mizuguchi et al., Appl. Phys. Lett., 94 (2009) 012503. 1–3.

[19] J. Guo et al., Phys. Rev. B, 82 (2010) 180520I.

[20] J. Bardeen, L. N. Cooper, and J. R. Schrieffer, Phys. Rev. B,108, (1957) 1175.

[21] R. B. Goldfarb, M. Lelental, C.A. Thompson, in: R.A. Hein, T.L. Francavilla, D.H. Liebenberg (Eds.), Magnetic Susceptibility of Superconductors and Other Spin Systems (Plenum, New York, 1991), p. 49.and references therein.

[22] F. Gomory, Supercond. Sci. Technol., 10 (1997) 523. references therein.

[23] M. J. Qin, C.K. Ong, Phys. Rev. B, 61 (2000) 9786.

[24] M. Polichetti, M.G. Adesso, T. Di Matteo, A. Vecchione, S. Pace, Physica C, 332 (2000) 378.

[25] M. Polichetti, M.G. Adesso, S. Pace, Physica C, 401 (2004) 196.

[26] V. M. Vinokur, M. V. Feigelman and V. B. Geshkenbein, Phys. Rev. Lett., 67, (1991) 915.

[27] J. Gilchrist, Physica C, 219 (1994) 67.

[28] J. Gilchrist J and C. J. van der Beek, Physica C, 231(1994) 147.

[29] C. P. Bean, Phys. Rev. Lett., 8 (1962) 250.

[30] C.P. Bean, Rev. Mod. Phys., 36 (1964) 31.

[31] P. W. Anderson and Y. B. Kim, Rev. Mod. Phys., 36 (1964) 39.

[33] A. P. Mackenzie, S. R. Julian, D. C. Sinclair and C. T. Lin Phys. Rev. B, 53, (1996) 5848.

[34] Y. Nakamura and S. Uchida, Phys. Rev. B, 47 (1993) 8369(R)

[35] H. Okabe, N. Takeshita, K. Horigane, T. Muranaka and J. Akimitsu, arXiv:1002.1832v2 (2010).

[36] K. Ahilan, J. Balasubramaniam, F. L. Ning, T. Imai, A. S. Sefat, R. Jin, M. A. McGuire, B. C. Sales and D. Mandrus, J. Phys.: Condens. Matter., 20 (2008) 47220.

[37] A. I. Larkin, and Yu. N. Ovchinnikov, Sov. Phys. JETP, 27 (1978) 280.

[38] A. I. Larkin, and Yu. N. Ovchinnikov , J. Low Temp. Phys., 34, (1979) 409.

[39] D. S. Fisher, M. P. A. Fisher and D. A. Huse, Phys. Rev. B, 43 (1991) 130.

[40] Y. Yeshurun, and A. P. Malozemoff, Phys. Rev. Lett., 60 (1988) 2202.

[41] F. London, Superfluids, vol. 1 (New York: Dover,1961)

[42] C. J. Gorter and H. B. G. Casimir, Phys. Z., 35 (1934a) 963.

[43] C. J. Gorter and H. B. G. Casimir Physica 1, (1934b) 306.

[44] L.P. Gor'kov and A. I. Rusinov, Zh. Eksperim. i Teor. Fiz., 46 (1964) 1363.

[45] N. R. Werthamer, E. Helfand and P. C. Hohenberg,. Phys. Rev., 147 (1966) 295-302.

[46] A. Gurevich, Phys. Rev., 67 (2003) 184515.

Chapter II
Measurement of the AC magnetic susceptibility of type II superconductors

Superconducting and magnetic properties of type II superconductors are often investigated by analyzing their AC magnetic response. In particular, the complex AC magnetic susceptibility technique is a very useful inductive method for characterizing the superconducting materials, especially high-T_C and new Fe-based superconductors, since it allows both to investigate the superconducting properties of the sample and to obtain information about the pinning mechanisms and the flux dynamical regimes governing the AC magnetic response[1-9].

The AC magnetic susceptibility technique consists in applying a time dependent magnetic field on the sample, while acquiring, by the lock-in amplification technique, the in-phase and out-of-phase components of the sample AC magnetization which are directly related to the AC magnetic susceptibility. Although the same kind of investigation can be performed by using different methods such as direct AC transport measurements and mechanical oscillator measurements[10,11], the AC susceptibility technique is an inductive very highly sensitive method that gives the opportunity to estimate several superconducting parameters, to study the electromagnetic granularity of the sample, and to detect the changes in the flux dynamics, in particular from the higher harmonics, induced by the changes of the external parameters such as the frequency and the amplitude of the AC magnetic field, and the amplitude of a superimposed DC field[1,12-14].

II.1 The AC magnetic susceptibility

The magnetic susceptibility is the quantity of interest in AC magnetic measurements where a small AC drive magnetic field $H(t) = H_{ac}\sin(\omega t)$ is applied and the time-dependent magnetization $M(t)$ of the sample, that is the magnetic moment $m(t)$ per unit volume, is acquired. The AC field induces shielding currents circulating in the outer sample surface and above the low temperature diamagnetic state the flux penetrates the sample in form of flux lines which are forced to move towards the interior of the sample by the shielding currents. Since the generation of these currents depends on the magnetic state of the sample, information about the magnetic and superconducting properties of the system can be extracted by measuring the magnetic moment $m(t)$ generated by the currents.The slope of the $M(H)$ curves is called the magnetic susceptibility $\chi = dM/dH$ and, for applied magnetic field weak enough, it can be expressed as a power series expansion in the magnetic field, i.e.

$$M(t) = \sum_{n,} \mathrm{Im}[\mu_0 \chi_n H(t)^n], \tag{II.1}$$

where $n = 1,2,3,$ ... and χ_n are the magnetic susceptibility nonlinear n-th order harmonics with dimension of $[H]^{-(n-1)}$ thus giving a dimensionless χ.

Since in general the sample magnetization is a nonlinear signal with respect to the external field, the magnetic susceptibility has to be taken as a complex function $\chi = \sum_n [\chi_n{}' - i\chi_n{}'']$. In fact, by substituting into the Eq.(II.1) yields

$$M(t) = \sum_n M_{ac\,n} \sin[n\omega t + \varphi_n], \tag{II.2}$$

where the amplitude $M_{ac\,n}$ and the phase shift φ_n of the n-th harmonic are given by

$$M_{ac\,n} = \sqrt{[\mu_0 \chi_n{}' H_{ac}{}^n]^2 + [\mu_0 \chi_n{}'' H_{ac}{}^n]^2}, \tag{II.3a}$$

$$\varphi_n = \tan^{-1} \frac{\chi_n{}''}{\chi_n{}'}. \tag{II.3b}$$

From the Eq. (II.2) the magnetization n-th harmonic has an in-phase component $\mu_0 \chi_n{}' H_{ac}{}^n$ and an out-of-phase component $\mu_0 \chi_n{}'' H_{ac}{}^n$. In fact, the Eq. (II.2) can be also expressed in the form

$$M(t) = \sum_n \mu_0 \chi_n{}' H_{ac}{}^n \sin(n\omega t) + \mu_0 \chi_n{}'' H_{ac}{}^n \cos(n\omega t), \tag{II.4}$$

and, from the comparison of the Eqs. (II.2) and (II.4) it follows that the in-phase and out-of-phase components of the magnetization are related to the real and imaginary parts of the AC susceptibility harmonics, i.e.

$$\chi_n{}' = M_{ac\,n} \cos\varphi_n = \frac{1}{\pi \mu_0 H_{ac}{}^n} \int_0^{2\pi} M(,t) \sin(n\omega t)\ d\omega t, \tag{II.5a}$$

$$\chi_n{}'' = M_{ac\,n} \sin\varphi_n = \frac{1}{\pi \mu_0 H_{ac}{}^n} \int_0^{2\pi} M(t) \cos(n\omega t)\ d\omega t, \tag{II.5b}$$

In particular, even harmonics are expected to vanish due to the symmetry of the field-magnetization (H-M) loop of the system. In fact, one has

$$M'_{2n}(H) = \chi'_{2n} H_{ac}{}^{2n} \sin(2n\omega t), \tag{II.6a}$$

$$M'_{2n}(-H) = \chi'_{2n} {H_{ac}}^{2n} \sin(2n\omega t), \quad \text{(II.6b)}$$

$$M''_{2n}(H) = \chi''_{2n} {H_{ac}}^{2n} \cos(2n\omega t), \quad \text{(II.6c)}$$

$$M''_{2n}(-H) = \chi''_{2n} {H_{ac}}^{2n} \cos(2n\omega t), \quad \text{(II.6d)}$$

from which the symmetry $M(H) = -M(-H)$ implies $\chi'_{2n} = 0$ and $\chi''_{2n} = 0$. The absence of even harmonics is expected in the Bean critical state model[15,16] where the critical current density j_c is independent of the external magnetic field H. On the other hand, for field dependent critical current density, as in the Kim critical state model[17,18], nonzero even harmonics are expected if the H-M loop is no longer symmetric due to the $j_c(H)$ law. In fact, the existence of flux dynamical regimes producing nonlinear dissipation and governing the AC magnetic response of the sample can give asymmetric magnetization loops and then nonzero even harmonics of the AC susceptibility.

II.2 Principle of measurements of the AC magnetic susceptibility

The principle of measurement of the complex susceptibility involves the application of an alternate magnetic field, with or without a superimposed DC field, while a variation of the magnetic flux inside the sample is detected by means of the voltage induced in a pick-up coil surrounding the sample. The basic configuration of such kind of measurement system is shown in Fig. II.1, where the sample is represented in form of a rectangular prism with a time magnetization $M(t)$ corresponding to a time dependent magnetic flux through the turns of the pick-up coil. The time derivative of this magnetic flux induces a voltage in the pick-up coil which can be detected and is directly related to the sample magnetization. It is worth noting that the sample has to be much longer than the pick-up coil in order to neglect geometric edge effects on the acquired signal and to reduce the demagnetizing field effects. In fact, in such kind of geometry, demagnetizing fields, arising from the non-ellipsoidal shape and from the presence of sharp edges, can modify the effective magnetic field induction acting on the sample surface and governing the measured AC magnetic response.

In presence of an alternate magnetic field $\mu_0 H_{ac} \sin(\omega t) = \mathrm{Im}\left[\mu_0 H_{ac} e^{i\omega t}\right]$ the voltage induced in the pick-up coil of N turns with area S is given by

$$v(t) = -NS \frac{d}{dt} [\, \mu_0 H(t) + M(t)]. \quad \text{(II.7)}$$

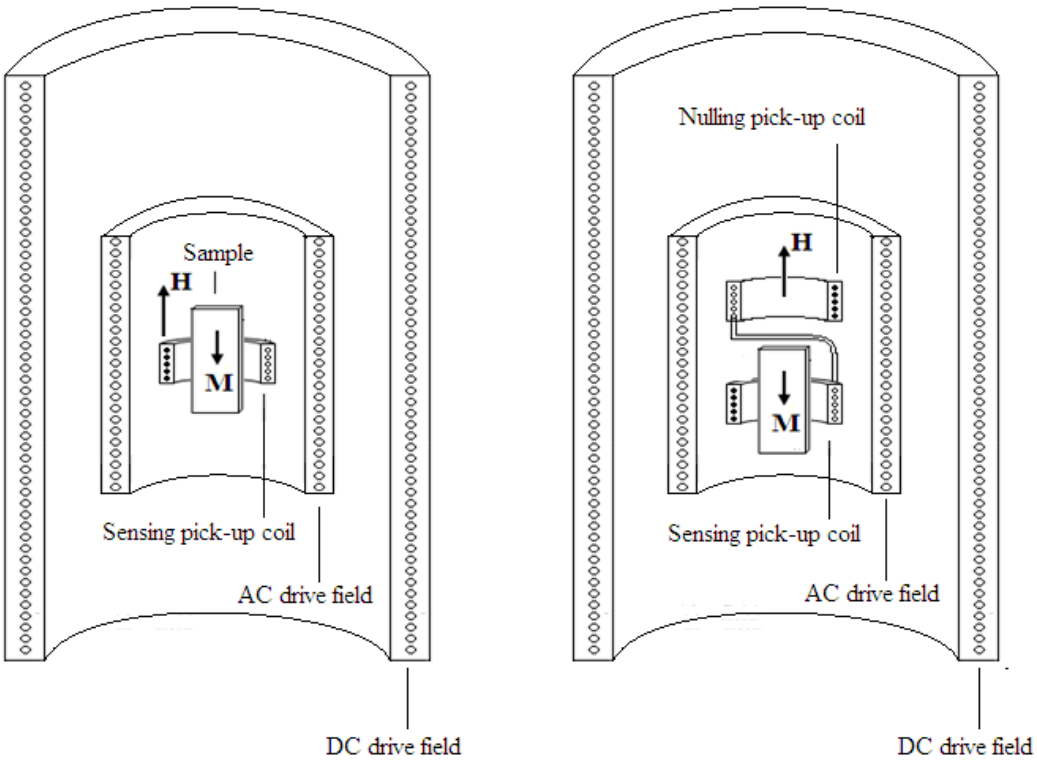

(a) (b)

Figure II.1 Schematic diagram of (a) the basic configuration with one pick-up sensing coil and (b) the two-coils configuration for the measurement of the AC magnetic susceptibility.

Here the signal contribution due to the flux of the external magnetic field $\mu_0 H(t)$could be high enough to cover the magnetic response $M(t)$ from the sample and then affecting the measurement. For this reason, several actual susceptometers are provided with a set of two identical pick-up coils connected in opposition, one of them surrounding the sample and then sensing (s) its magnetic response, the other one nulling (n) the external background, as shown in the Fig. 1b. In this case, the amplitude of the AC voltage induced in the peak-up coils is given by

$$v(T,t) = -\frac{1}{\gamma}\frac{d}{dt}[\Phi_s(t) - \Phi_n(t)], \tag{II.8}$$

where $\Phi_n(t) = NS\mu_0 H(t)$ and $\Phi_s(T,t) = NS[\mu_0 H(t) + M(t)]$, and a calibration factor γ has been also introduced. Then, the Eq. (II.27 becomes

$$v(t) = -\frac{1}{\gamma}\frac{d}{dt}[\Phi_s(T,t) - \Phi_n(T,t)] = -\frac{1}{\gamma}\frac{dM(t)}{dt}. \tag{II.9}$$

II.2.1 The Phase-Sensitive Detection (PSD)

The fundamental and the higher harmonics of the AC magnetization are measured by mean of a lock-in amplifier which usually use a "phase-sensitive detection" technique to reveal the signal accompanied by the noise. In modern susceptometers two kinds of detection technique can be usually accomplished. The more standard one is named "correlating technique" and allows one to acquire separately the in-phase and the out-of-phase components of the fundamental and higher harmonics of the magnetic response from the sample, corresponding to the real and imaginary part of the susceptibility harmonics according to the Eqs. (II.5a) and (II.5b). A band-pass filter can be set around the fundamental frequency in order to acquire only the fundamental complex susceptibility.

The second type of detection technique is named "integrating technique" and consists in the acquisition of the whole signal containing the sample magnetic response. This kind of measurement gives the so called "wide band susceptibility" which has a physical interpretation different from the susceptibility harmonics acquired by the standard acquisition. However, the two types of detection techniques can be also used together in the investigation of the magnetic properties of high-T_c superconductors.

II.2.1.1 Correlating detection technique

In this kind of detection technique the lock-in amplification consists in the multiplication of the magnetic signal $v(t)$ induced in the peak-up coil and a reference signal $r(t)$ which can be taken as

$$h(t) = \sin(\theta t - \phi), \tag{II.10}$$

where the reference frequency θ and phase ϕ can be tuned. In fact, by multiplying this reference signal and the signal $v(t)$ expressed from the Eq. (II.4), yields

$$v(t)h(t) = -\frac{1}{\gamma}\sum_n \frac{d}{dt}\left\{\mu_0 {H_{ac}}^n\left[\chi_n^{'}\sin(n\omega t) + \chi_n^{''}\cos(n\omega t)\right]\sin(\theta t - \phi)\right\}. \tag{II.11}$$

After the time derivative of the Eq. (II.11) one obtains the product signal

$$v(t)h(t) = \frac{1}{\gamma}\sum_n \frac{d}{dt} n\omega\mu_0 {H_{ac}}^n\left[-\chi_n^{'}\cos(n\omega t) + \chi_n^{''}\sin(n\omega t)\right]\sin(\theta t - \phi), \tag{II.12}$$

which is averaged over a many cycle of the AC field thus giving an output

$$K_{\theta,\phi} = \frac{1}{2\pi A}\int_0^{2\pi} v(t)h(t)\, d\omega t =$$

$$\frac{1}{2\pi A}\int_0^{2\pi}\frac{1}{\gamma}\sum_n n\omega\mu_0 {H_{ac}}^n\left[-\chi_n^{'}\cos(n\omega t) + \chi_n^{''}\sin(n\omega t)\right]\sin(\theta t-\phi)\; d\omega t, \quad \text{(II.13)}$$

where A is a factor taking into account the preliminary amplification.

When the frequency of the reference signal is different from the harmonic frequencies of the input signal $v(t)$, i.e. $n\omega \neq \theta$, the functions $\cos(n\omega t)\sin(\theta t-\phi)$ and $\sin(n\omega t)\sin(\theta t-\phi)$ in the Eq. (II.13) oscillate in time with a zero average value and then $K_{\theta,\phi} = 0$. On the other hand, when $n\omega = \theta_r$ and for $\phi = 0, \pi/2$, the Eq. (II.13) reduces to

$$K_{\theta,\phi} = \frac{n\omega\mu_0 {H_{ac}}^n}{2\pi A\gamma}\int_0^{2\pi}\chi_n^{''}(T)\sin(n\omega t)^2\, d\omega t = \frac{n\omega\mu_0 {H_{ac}}^n\chi_n^{''}(T)}{2A\gamma},$$
$$\theta = n\omega, \phi = 0, \quad \text{(II.14a)}$$

$$K_{\theta,\phi} = \frac{n\omega\mu_0 {H_{ac}}^n}{2\pi A\gamma}\int_0^{2\pi}\chi_n^{'}(T)\cos(n\omega t)^2\, d\omega t = \frac{n\omega\mu_0 {H_{ac}}^n\chi_n^{'}(T)}{2A\gamma},$$
$$\theta = n\omega, \phi = \frac{\pi}{2}. \quad \text{(II.14b)}$$

In fact, the measured quantities are given by

$$\mu_0 {H_{ac}}^n\chi_n^{'} = \frac{2A\gamma}{n\omega}K_{\theta=n\omega,\phi=0}, \quad \text{(II.15a)}$$

$$\mu_0 {H_{ac}}^n\chi_n^{''} = \frac{2A\gamma}{n\omega}K_{\theta=n\omega,\phi=\frac{\pi}{2}}, \quad \text{(II.15b)}$$

$$\mu_0 H_{ac}\sqrt{{\chi_n^{'}}^2 + {\chi_n^{''}}^2} = \frac{2A\gamma}{n\omega}\mu_0 {H_{ac}}^n\sqrt{{K_{\theta=n\omega,\phi=0}}^2 + {K_{\phi=n\omega,\phi=\frac{\pi}{2}}}^2}, \quad \text{(II.15c)}$$

$$\varphi_n = \tan^{-1}\frac{\chi_n^{''}}{\chi_n^{'}} = \tan^{-1}\frac{K_{\theta=n\omega,\phi=\frac{\pi}{2}}}{K_{\theta=n\omega,\phi=0}}. \quad \text{(II.15d)}$$

It is worth noting that an alternative definition of the harmonic susceptibility is for an applied field $\mu_0 H_{ac}\cos(\omega t) = \mathrm{Re}\left[\mu_0 H_{ac}\, e^{i\omega t}\right]$. In this case the Eq. (II.1) becomes

$$M(t) = \sum_n \mathrm{Re}[\mu_0\chi_n H(t)^n] = \sum_n \mu_0 {H_{ac}}^n\left[\chi_n^{'}\cos(n\omega t) - \chi_n^{''}\sin(n\omega t)\right], \quad \text{(II.16)}$$

and then the susceptibility harmonics real and imaginary parts can be evaluated by

$$\chi_n{}' = \frac{1}{\pi\mu_0 {H_{ac}}^n}\int_0^{2\pi} M(,t)\cos(n\omega t)\ d\omega t, \tag{II.17a}$$

$$\chi_n{}'' = -\frac{1}{\pi\mu_0 {H_{ac}}^n}\int_0^{2\pi} M(t)\sin(n\omega t)\ d\omega t, \tag{II.17b}$$

Then, by taking the reference signal as

$$r(t) = \cos(\theta t - \phi), \tag{II.18}$$

the Eq. (II.13) becomes

$$K_{\theta_r,\phi_r} = \frac{1}{2\pi A}\int_0^{2\pi} v(t)\cos(\theta t - \phi)\ d\omega t =$$

$$\frac{1}{2\pi A}\int_0^{2\pi}\sum_n n\omega\mu_0 {H_{ac}}^n\left[\chi_n' \cos(n\omega t) + \chi_n'' \sin(n\omega t)\right]\cos(\theta t - \phi)\ d\omega t, \tag{II.19}$$

from which

$$K_{\theta,\phi} = \frac{n\omega\,\mu_0 {H_{ac}}^n}{2\pi A\gamma}\int_0^{2\pi}\chi_n''\sin(n\omega t)^2\,d\omega t = \frac{n\omega\,{H_{ac}}^n\chi_n''}{2A\gamma},$$

$$\theta = n\omega, \phi = 0, \tag{II.20a}$$

$$K_{\theta,\phi} = \frac{n\omega\,\mu_0 {H_{ac}}^n}{2\pi A\gamma}\int_0^{2\pi}\chi_n'(T)\cos(n\omega t)^2\,d\omega t = \frac{n\omega\,{H_{ac}}^n\chi_n'}{2A\gamma},$$

$$\theta = n\omega, \phi = 0, \tag{II.20b}$$

which coincide with the results (II.5a) and (II.5b). However, for interlaboratory comparisons of the harmonic susceptibilities as for as theoretical calculations it is necessary to take into account the relations between the susceptibility harmonics parts expressed by the Eqs. (II.5) and (II.17) for the sine (s) and cosine (c) lock-in reference signal, respectively. One can relate them as[18]

$$\chi_{s}{}'_{4n-3} = \chi_{c}{}'_{4n-3}, \chi_{s}{}''_{4n-3} = \chi_{c}{}''_{4n-3}, \tag{II.21a}$$

$$\chi_{s}{}'_{4n-2} = -\chi_{c}{}''_{4n-2}, \chi_{s}{}''_{4n-2} = \chi_{c}{}'_{4n-2}, \tag{II.21b}$$

$$\chi_{s}{}'_{4n-1} = -\chi_{c}{}'_{4n-1}, \chi_{s}{}''_{4n-1} = -\chi_{c}{}''_{4n-1}, \quad \text{(II. 21c)}$$

$$\chi_{s}{}'_{4n} = \chi_{c}{}''_{4n}, \chi_{s}{}''_{4n} = -\chi_{c}{}'_{4n}. \quad \text{(II. 21d)}$$

In fact, the use of the two different reference signals explains why the same harmonics parts from the samples measured on different equipments show difference in sign. Moreover, this is very crucial when considering the theoretical simulation of the magnetic response of granular superconductors, due to the composition of two contributions coming from the inter- and intragranular volume fractions.

II.2.1.2 Integrating detection technique

In this second type of detection technique a square wave is taken as lock-in reference signal, $r(\omega t - \phi)$. Then, the output signal for the input field $\mu_0 H_{ac} \sin(\omega t)$ can be expressed as

$$R_\phi = -\frac{1}{2\pi A\gamma}\int_0^{2\pi} \sum_n n\omega\mu_0 {H_{ac}}^n [-\chi_n' \cos(n\omega t) + \chi_n'' \sin(n\omega t)]\ r(\omega t - \phi)\, d\omega t. \quad \text{(II.22)}$$

By considering the Fourier expansion of the square wave,

$$r(\omega t) = \sum_m \frac{1}{2m+1} \sin[(2m+1)\omega t],\ \ \phi = 0, \quad \text{(II.23a)}$$

$$r\left(\omega t - \frac{\pi}{2}\right) = \sum_m \frac{4(-1)^m}{(2m+1)\pi} \cos[(2m+1)\omega t], \phi = \frac{\pi}{2}, \quad \text{(II.23a)}$$

it is easy to show that the Eqs. (II.22) reduces to

$$R_\phi = -\frac{2}{\pi A\gamma} \sum_n \omega\mu_0 {H_{ac}}^{2n+1} \chi_{2n+1}'', \phi = 0, \quad \text{(II.24a)}$$

$$R_\phi = \frac{2}{\pi A\gamma} \sum_n (-1)^n \omega\mu_0 {H_{ac}}^{2n+1} \chi_{2n+1}', \phi = \frac{\pi}{2}. \quad \text{(II.24b)}$$

In particular, when the input signal $v(t)$ contains only the first harmonic, the Eqs. (II.24a) and (II.24b) reduce to

$$R_\phi = -\frac{2}{\pi A\gamma}\omega\mu_0 H_{ac}\chi_1^{''} = -\frac{2\omega}{\pi A\gamma}M_{ac\,1}\sin\varphi_1 \propto M_r(T),\ \phi = 0, \qquad \text{(II.25a)}$$

$$R_\phi = -\frac{2}{\pi A\gamma}\omega\mu_0 H_{ac}\chi_1^{'} = -\frac{2\omega}{\pi A\gamma}M_{ac\,1}\cos\varphi_1 \propto M_a(T), \phi = \frac{\pi}{2}, \qquad \text{(II.25b)}$$

where $M_r(T) = M(T, \omega t = 0)$ and $M_a(T) = M(T, \omega t = \frac{\pi}{2})$ are the values of the sample magnetization when the external drive AC field has the values of zero and of its amplitude H_{ac}. If one defines the "remanent susceptibility" χ_r and the "amplitude susceptibility" χ_a as

$$\chi_r = \frac{M_r(T)}{\mu_0 H_{ac}}, \qquad \text{(II.26a)}$$

$$\chi_a = \frac{M_a(T)}{\mu_0 H_{ac}}, \qquad \text{(II.26b)}$$

the measured quantities are given by

$$\mu_0\chi_r H_{ac} = M_r(T) = -\frac{\pi A\gamma}{2\omega}R_{\phi=0}, \qquad \text{(II.27a)}$$

$$\mu_0\chi_a H_{ac} = M_a(T) = -\frac{\pi A\gamma}{2\omega}R_{\phi=\frac{\pi}{2}}. \qquad \text{(II.27b)}$$

II.3 Demagnetizing effects on the measurement of the AC susceptibility

Demagnetizing field arises from the non-ellipsoidal shape of the sample and from the presence of sharp edges on its surface. In general, the effective magnetic field induction B acting on the sample corresponding to the external applied field $\mu_0 H(t)$ is given by

$$B(t) = \mu_0[H(t) - \mathcal{D}M(t)], \qquad \text{(II.28)}$$

where $\mathcal{D}$ is the demagnetizing factor $(0 < \mathcal{D} < 1)$ and $M(t)$ is the sample magnetization. The demagnetizing factor is $\mathcal{D} = 0$ for thin films with plane parallel to the applied field while $\mathcal{D} = 1$ for thin films in a perpendicular field. Otherwise, experimental and theoretical works on demagnetizing factors for several shape of the sample can be found in literature which provide values of $\mathcal{D}$. Since the demagnetizing field is not uniform, its value can be numerically calculated and averaged values of demagnetizing factors over the sample volume should be considered. In fact, two types of averaging can be used to determine the effective value of $\mathcal{D}$[19]: the "fluxmetric" average, which is an average

over the cylinder cross section located in the mid-plane of the sample, and the "magnetometric" average, which is an average over the entire cylinder volume.

For a sinusoidal applied field $H(t) = \mu_0 H_{ac} \sin(\omega t)$ the effective magnetic field induction accounting of the demagnetizing effects is shown in the Fig. II.2a together with the curve of the measured magnetization amplitude as function of the applied field amplitude. The difference between the applied field and the effective field is the time dependent demagnetization field which is constant between the time of full penetration field B_{fp} and the time of maximum value of the applied field. Then, the Bean model of the critical state has to be modified as shown in the Fig. II.2b at a fixed temperature.

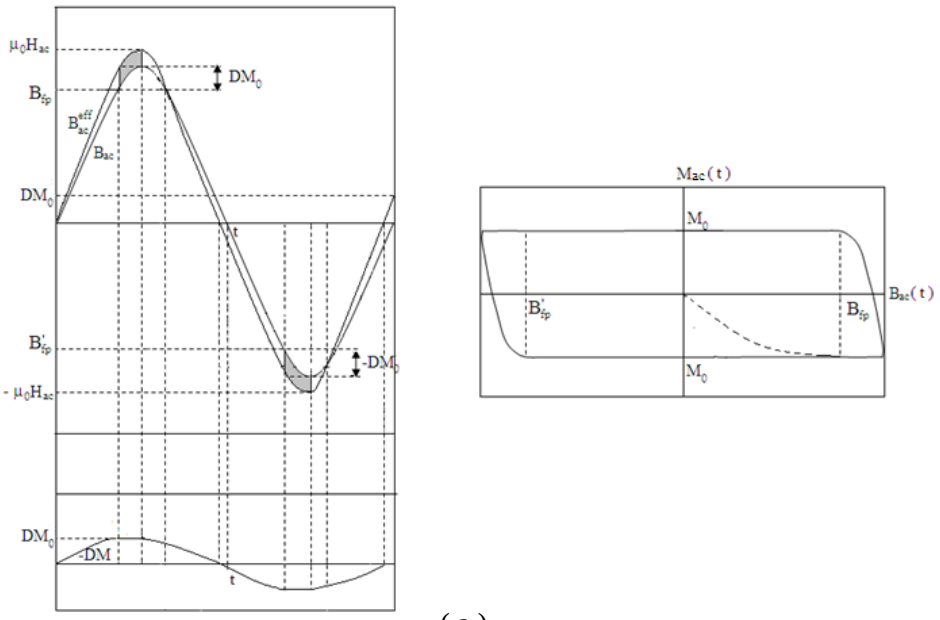

(a)

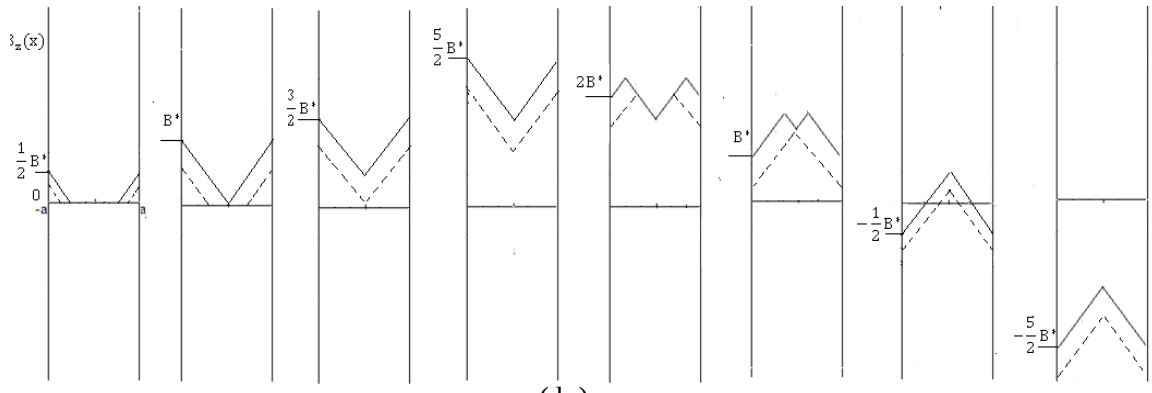

(b)

Figure II.2 (a) Schematic diagram of (left) time dependence of the effective AC field due to the applied field and the demagnetizing field corresponding to (right) the field-magnetization curve. (b) Schematic diagram of Bean model penetration of (dash line) the applied field and (solid line) the effective magnetic field corresponding to the curves in (a).

When demagnetizing effects have to be taken into account, the measured magnetic susceptibility χ_{m} has to be converted into the true internal susceptibility χ_{in}. The intrinsic susceptibility is obtained from the measured one as

$$\chi_{\mathrm{in}} = \frac{1-\mathcal{D}\chi_{\mathrm{m}}}{\chi_{\mathrm{m}}}. \tag{II.29}$$

For the complex case, the real and imaginary parts of the n-th harmonic of the intrinsic susceptibility can be obtained as

$$\chi_{\mathrm{in}}{}'_n = \frac{\chi_{\mathrm{m}}{}'_n - \mathcal{D}\left\{\left(\chi_{\mathrm{m}}{}'_n\right)^2 + \left(\chi_{\mathrm{m}}{}''_n\right)^2\right\}}{\left(1-\mathcal{D}\chi_{\mathrm{m}}{}'_n\right)^2 + \left(4\mathcal{D}\chi_{\mathrm{m}}{}''_n\right)^2}, \tag{II.30a}$$

$$\chi_{\mathrm{in}}{}''_n = \frac{\chi_{\mathrm{m}}{}''_n}{\left(1-\mathcal{D}\chi_{\mathrm{m}}{}'_n\right)^2 + \left(4\mathcal{D}\chi_{\mathrm{m}}{}''_n\right)^2}. \tag{II.30b}$$

and in the following we will as χ to the intrinsic susceptibility.

It is worth noting that a demagnetizing field correction by using the Eqs. (II.30a) and (II.30b) is not true correct in the case of a granular superconductor sample. In this case, two contributions to the magnetic response from the individual grains and the intergranular matrix, respectively, are expected, which should be separately corrected by applying the rules (II.30a) and (II.30b) with different demagnetizing factors for the shapes of the whole sample and of the individual grains, respectively. However, this is not always possible due both to the overlap of the inter- and intragranular contributions in the magnetic response and to the not known actual boundary conditions at grains's surfaces. An alternative procedure of demagnetizing correction of the magnetic response from granular samples will be introduced in the following.

II.4 Physical interpretation of the AC susceptibility

II.4.1 Real and imaginary parts of the first harmonic

The Eq. (II.4) is consistent with the physical meaning of the first harmonic of the complex magnetic susceptibility. In fact, according to Eq. (II.5a), there is a close connection between χ_1' and the time average of the magnetic energy stored in the volume of the sample which is given by

$$W_m = \frac{\chi_1' \mu_0 H_{ac}}{2}. \tag{II.31}$$

Since $W_m < 0$ in the superconducting state due to the field expulsion, it follows that $\chi_1^{'} < 0$. On the other hand, according to the Eq. (II.5b), the energy converted into heat during a cycle of the AC field is

$$W_q = -\pi \chi_1^{''} \mu_0 {H_{ac}}^2, \tag{II.32}$$

from which $\chi_1^{''} > 0$ since $W_q < 0$.

Most commonly, the components of the AC susceptibility $\chi = \sum_n (\chi_n^{'} - i\chi_n^{''})$ are measured as function of the temperature T. For example, the behavior of $\chi_1^{'}$ and $\chi_1^{''}$ with varying the temperature, deduced from the Eqs. (II.5a) and (II.5b), is shown in the Fig. II.3a for the critical state.

Since the phase $\varphi_1(T)$ represents the time lag in the flux penetration inside the superconducting sample as response to the external field due to different reasons such as the pinning, the flux viscosity and the geometric barriers, it is expected $\varphi_1 = 0$ both in the Meissner state where the flux does not penetrate $\left(M_{ac\,1} = -\mu_0 H_{ac}\right)$ and at temperature $T \geq T_c$ where the flux is not trapped in the superconductor $\left(M_{ac\,1} = 0\right)$. Then, from the Eq. (II.5a), it follows that $\chi_1^{'}(T) = M_{ac\,1}(T)/\mu_0 H_{ac} = -1$ at $T = 0$ and $\chi_1^{'}(T) = M_{ac\,1}(T)/\mu_0 H_{ac} = 0$ at $T \geq T_c$ (see the Fig. II.3a). In the intermediate region of temperature both $\varphi_1(T)$ and $M_{ac\,1}(T)$ decrease as moving away from the superconducting transition and assume negative values. Correspondingly, $\chi_1^{'}(T)$ is negative and decreases with decreasing temperature, with a minimum between the two extremes of the transition.

On the other hand, from the Eq. (II.5b) $\chi_1^{''}(T) = 0$ both in the Meissner state and at $T \geq T_c$, while in the intermediate region of temperature it assumes positive values and reaches a maximum in correspondence of the maximum value of $\sin\varphi_1(T)$, corresponding to the maximum dissipation inside the superconductor.

There have been three main types of models suggested in literature for the description of AC susceptibility of high-T_c and more recently discovered Fe-based superconductors. The first model provides for the solution of the diffusion equation of the magnetic flux in the linear case, where the superconductor shows a linear resistivity corresponding to the frequency-dependent length scale δ (see the Fig. II.3b). For a slab of width $2R$ in a parallel magnetic field one finds[20]

$$\chi^{'} = \chi_a = u\frac{\sinh(u)+\sin(u)}{\cosh(u)+\cos(u)} - 1, \tag{II.33a}$$

$$\chi^{''} = \chi_r = u\frac{\sinh(u)+\sin(u)}{\cosh(u)+\cos(u)}, \tag{II.33b}$$

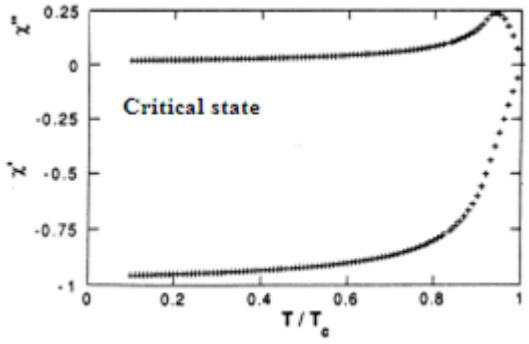

(a)

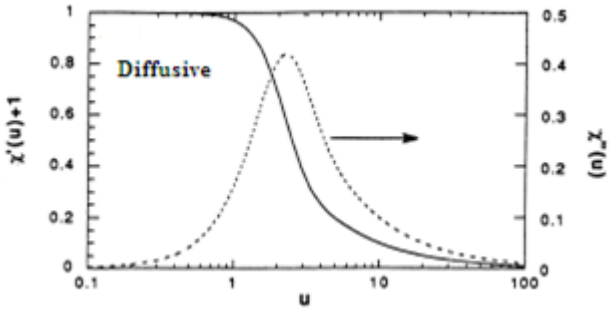

(b)

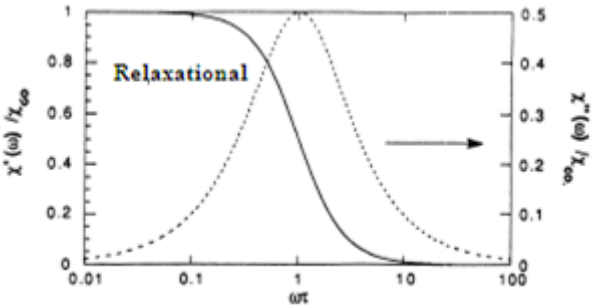

(c)

Fig. II.3 Theoretical plots of $\chi'$and $\chi''$for (a) the Bean critical state, (b) the diffusive and (c) the relaxational models for a slab geometry[9].

where $u = \delta/2R$ with δ the frequency-dependent length scale of the magnetic flux profile decaying exponentiallyinside the sample. This linear regime is dissipative and the peak in χ'' and χ_r is reached when $\delta \approx 0.887\,L$ for a cylinder and $\delta \approx 0.556\,L$ for a slab. Moreover, a model combining different mechanisms has been used, based on the penetration depth of the AC field[1,9,21,22]

$$\lambda = \lambda_L^2 + \lambda_c^2 \frac{1+i\omega\tau}{1+i\omega\tau_0}, \tag{II.34}$$

where λ_L is the London[21] penetration depth, $\lambda_c = (c^2 B^2/\alpha_L)^{1/2}$ is the Campbell[22] penetration depth with α_L the elastic restoring force density on flux-lattice (the Labusch[22] parameter) defined in terms of a relaxation time τ, which measures how fast the flux penetration approaches the equilibrium, as[23]

$$\tau = \frac{\alpha_L}{\eta_{ff}}, \tag{II.35}$$

where η_{ff} is the flux flow viscosity.

However, many practical applications require the determination of the superconducting properties in the conditions of a strongly non-linear regime. An example of strongly non-linear current-voltage equation is the critical state in which the superconducting material is able to pin the flux lines. In this case, higher harmonics appear in the pick-up coil voltage. Then, χ_a and χ_r are no longer equal to χ' and χ'', respectively. The formulas for the fundamental susceptibilities of a slab are (see the Fig. II.3a)[24]

$$\chi' = \begin{cases} \frac{y}{2} - 1, \ 0 \le y \le 1 \\ \frac{1}{\pi}\left(\frac{y}{2} - 1\right)\frac{1}{\cos(1-2y)} + \left(-1 + \frac{4}{3y} - \frac{4}{3y^2}\right), \ 1 \le y \end{cases}, \tag{II.36a}$$

$$\chi'' = \begin{cases} \frac{2y}{3\pi} \\ \frac{1}{3\pi}\left(\frac{y}{2} - 1\right)\left(\frac{6}{y} - \frac{4}{y^2}\right), \ 1 \le y \end{cases}, \tag{II.36b}$$

with $y = H_{ac}/(j_c\, R)$, while the components of the wide band susceptibility are given by[16]

$$\chi_a = \begin{cases} \frac{y}{2} - 1, \ 0 \le y \le 1 \\ -\frac{1}{2y}, \ 1 \le y \end{cases}, \tag{II.37a}$$

$$\chi_r = \begin{cases} \frac{y}{4}, 0 \le y \le 1 \\ 1 - \frac{y}{4} - \frac{1}{2y}, \ 1 \le y \le 2, \\ \frac{1}{2y}, 2 \le y \end{cases} \tag{II.37b}$$

The flux creep regime is often taken as a small perturbation in the pinning mechanism of the critical state by considering the value of j corresponding to the general solution of the diffusion equation in place of the critical value j_c.

The third main type of model assumes a field and temperature relaxation time with a general expression of the AC susceptibility[9,25,26]

$$\chi = \chi' - i\chi'' = \chi_\infty + \frac{\chi_0 - \chi_\infty}{[1+(i\omega\tau)^\alpha]^\beta}, \tag{II.38}$$

where $\chi_\infty = -1$ and $\chi_0 = 0$ are the values of the AC susceptibility in the high-frequency (full diamagnetic shielding) and low-frequency (full field penetration) limits, respectively. On the other hand, the two parameters α and β describe the distribution of the relaxation time τ around its spatial average value (nonlocality) and the asymmetry of the frequency spectrum as a nonlinear effect (nonlinearity), respectively. The formula (II.38) is called the Havriliak-Negami[25] (H-N) formula and it reduces to the standard Debye relaxation for $\alpha = \beta = 1$, to the Cole–Cole form for $\alpha \neq 1$ and $\beta = 1$, and to the Davidson–Cole formula for $\alpha = 1$ and $\beta \neq 1$.In particular, at given frequency ω a peak in the imaginary part of the Eq. (II.38) is expected for α and β given by

$$\tau = f(\nu) = \left[\frac{\sin\left(\frac{\pi\alpha}{2(\beta+1)}\right)}{\sin\left(\frac{\pi\alpha\beta}{2(\beta+1)}\right)}\right]^{\frac{1}{\alpha}} (2\pi\nu)^{-1}. \tag{II.39}$$

It is worth noting that since the magnetic flux diffusion time satisfies the relation $\tau \sim L^2/D$, with $2L$ the characteristic specimen dimension, according to the Eq. (I.19) the function $f(\nu)$ in the Eq. (II.39) is related to the frequency dependent skin-depth of the taff regime δ, i.e. $f \sim \delta^{-2}$. In particular, the case of $f = (2\pi\nu)^{-1}$ corresponds to the existence of a resonance between the frequency of the external exciting AC field and the hopping frequency of the flux lines inside a superconductor between pinning sites.

Although this relaxational model has been found not appropriate[1] to describe superconductors high-T_c superconductors with respect to the diffusive and Bean critical state models, it has been found to be adapt to describe the magnetic response of Fe-based superconductors[27-31].

Another model for the susceptibility first harmonic refers to the reversible screening regime, where the system passes through equilibrium states. Two typical examples of reversible vortex motion are the Campbell's[32] reversible screening and the screening by Meissner currents. The reversible behavior corresponds to the absence of dissipation, i.e. $\chi'' = \chi_r = 0$. Moreover, the signal does not contain higher harmonics and then $\chi' = \chi_a$.

This reversible motion of vortices is well described by using the London equation $\boldsymbol{\nabla} \times \Lambda \boldsymbol{j} = -\boldsymbol{B}$ with the penetration scale length.

The Campbell regime occurs when the amplitude of the exciting field is small and the Abrikosov vortices are not displaced but they oscillate around their equilibrium positions producing a quasi-elastic response. The Campbell penetration depth is $\lambda_c^2 = \alpha_L^{-1} C_{xx}$, with C_{xx} is the relevant elastic modulus of the vortex lattice and α_L the Labusch parameter defined above. On the other hand, in the Meissner state shielding currents try to expel the magnetic flux from the superconducting volume to reach thermodynamical equilibrium. The characteristic space scale is the London penetration depth λ_L. The susceptibilities for a slab of width $2L$ in a parallel field are[22]

$$\chi' = \chi_a = -\left(1 - \frac{\lambda}{L}\tan\frac{L}{\lambda}\right), \tag{II.40}$$

Finally, the existence of barriers preventing the flux lines entering or leaving the sample has been considered in order to explain some experimental evidences. A model describing such kind of phenomenon is equivalent to the existence of a layer with thickness δ_b and high critical current density j_b on the surface of the sample, producing the irreversible barrier[1]

$$B_b = \mu_0 j_b \delta_b. \tag{II.41}$$

The susceptibilities are[33]

$$\chi' = \frac{1}{\pi}(\Theta - \sin\Theta\cos\Theta), \tag{II.42a}$$

$$\chi'' = \frac{4\frac{B_b}{\mu_0 H_{ac}}}{\pi\left(1-\frac{B_b}{\mu_0 H_{ac}}\right)}, \tag{II.42b}$$

with $\cos\Theta = 1 - 2\,B_b/\mu_0 H_{ac}$. The corresponding wide band susceptibilities are[33]

$$\chi_a = \begin{cases} -1, 0 \le \mu_0 H_{ac} \le B_b \\ 1 - \frac{B_b}{\mu_0 H_{ac}}, B_b \le \mu_0 H_{ac} \end{cases}, \tag{II.43a}$$

$$\chi_r = \begin{cases} 0, 0 \le \mu_0 H_{ac} \le B_b \\ 1 - \frac{B_b}{\mu_0 H_{ac}}, B_b \le \mu_0 H_{ac} \le 2B_b \\ \frac{B_b}{\mu_0 H_{ac}}, 2B_b \le \mu_0 H_{ac} \end{cases}, \tag{II. 43b}$$

II.3.2 Real and imaginary parts of the third harmonic

While the physical meaning of the real and imaginary parts of the fundamental susceptibility is well known, the interpretation of the higher harmonics is still object of discussion. In fact, the existence of higher harmonics, due to hysteretic losses, was first predicted by C.P. Bean[15,16] in his frequency independent critical state model. In particular, within this model, the critical current density is independent of the magnetic field giving zero even higher harmonics of the AC magnetic susceptibility. On the other hand, nonzero even higher harmonics are predicted in the Kim[17,18] critical state model within which a magnetic field dependent critical current density is considered. Moreover, the general shape of both the first and the higher AC magnetic susceptibility harmonics is independent of the AC field frequency.

A combined analysis, based on the comparison of both the fundamental and higher harmonics of the AC magnetic susceptibility has been used to investigate the actual pinning mechanisms and geometric barriers to the flux motion, the flux dynamical regimes governing the magnetic response, and the phase of the vortex matter[13,14,34].

In particular, the third harmonic components of the AC magnetic susceptibility were the most widely investigated since their intensity is the highest and easily detectable even in the absence of a DC field after the fundamental harmonic components. The strong differences in the shape of the third harmonic curves measured in different conditions have been largely investigated.

In particular, The Bean results for the temperature dependence of the third harmonics critical state model for a slab geometry is reported in the Fig. II.4. The real part of the third harmonic $\chi_3'(T)$ is zero below the $\chi_1''(T)$ peak temperature T_p, and shows a positive peak above T_p. On the other hand, the imaginary part $\chi_3''(T)$ shows an oscillatory behaviour displaying a positive peak at about T_p and a negative one at higher temperatures[34]. In general, variation in the temperatures of the peak maxima of $\chi_1''(T)$ and $|\chi_3(T)|$ can be reproduced in a critical state model by considering a critical current density $j_c(\nu)$ that increases with the frequency ν of the AC field, corresponding to the existence of relaxation phenomena. Moreover, also non-zero even harmonics can be predicted when a magnetic field dependence of j_c is considered, as in the Kim critical state model. However, the general shape of both the first and the higher ACS harmonics is independent of the frequency of the AC field in all the critical state models.

Besides these variation induced by different AC frequencies that can be explained by modifying the critical state models, variations in the height of the $\chi_1''(T)$ and $|\chi_3(T)|$ peaks, and in the shape of the $\chi_3'(T)$ and $\chi_3''(T)$ components, cannot be explained by using any critical state model, and they can be interpreted by means of the comparison

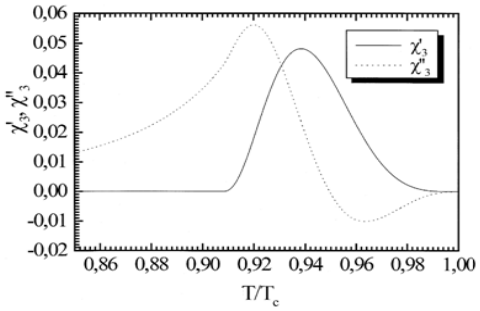

Figure II.4. Temperature dependence of $\chi_3^{'}(T)$ and $\chi_3^{''}(T)$ calculated within the critical state model for a slab geometry[34].

with the numerically calculated by solving the diffusion equation of the magnetic field in the sample with for various flux dynamical regimes and pinning mechanisms. In fact, the frequency and temperature dependent curves of $\chi_3^{'}(T)$ and $\chi_3^{''}(T)$ for the flux flow, taff, flux creep and creep-flow parallel regimes have been numerically calculate by solving the diffusion equation[34]. These curves are reported in the Fig. II.5a-h, respectively, together with the critical state results, within the collective pinning.

In the case of flux creep (Fig. II.5a-b), the $\chi_3^{'}(T)$ curves show large difference from the critical state prediction at lower temperature. In fact, while $\chi_3^{'}(T)$ is expected to be always positive for the critical state, it can assume negative value at temperatures T smaller than the peak temperature in the corresponding $\chi_1^{''}(T)$ curve. In particular, a negative peak appears and shift towards higher temperature with increasing frequency together with the following larger positive maximum. On the other hand, the $\chi_3^{''}(T)$ curve is very similar to the critical state prediction with the presence of a positive maximum followed by a negative smaller peak which are shifted to higher temperatures with increasing frequency.

For the taff (Fig. II.5c-d) and flux flow (Fig. II.5e-f) and regimes, the $\chi_3^{'}(T)$ curves display negative values and bell-like shapes, with the peak temperatures increasing as the frequency increases. On the other hand, the $\chi_3^{''}(T)$ curves show an oscillatory behavior, displaying positive values on approaching T_c and negative values at lower temperature. As the frequency increases, such behavior of occurs closer and closer to T_c.

Finally, we discuss the curves of $\chi_3^{'}(T)$ and $\chi_3^{''}(T)$ for the parallel resistor model between the flux creep and the flux flow regime (Fig. II.5g-h). Here, the $\chi_3^{'}(T)$ curve shows large deviation from the critical state prediction both at lower and higher temperature, and this occurs more with increasing frequency. In particular, a negative peak appears at lower temperature due to the flux creep contribution, while the flux flow contribution produces the lowering of the higher temperature positive maximum which tend to become a double negative peak with increasing frequency. Correspondingly, the

$\chi_3''(T)$ curve deviates from the critical state prediction for the lowering of the lower temperature positive peak and the rising of the higher temperature positive peak near T_c.

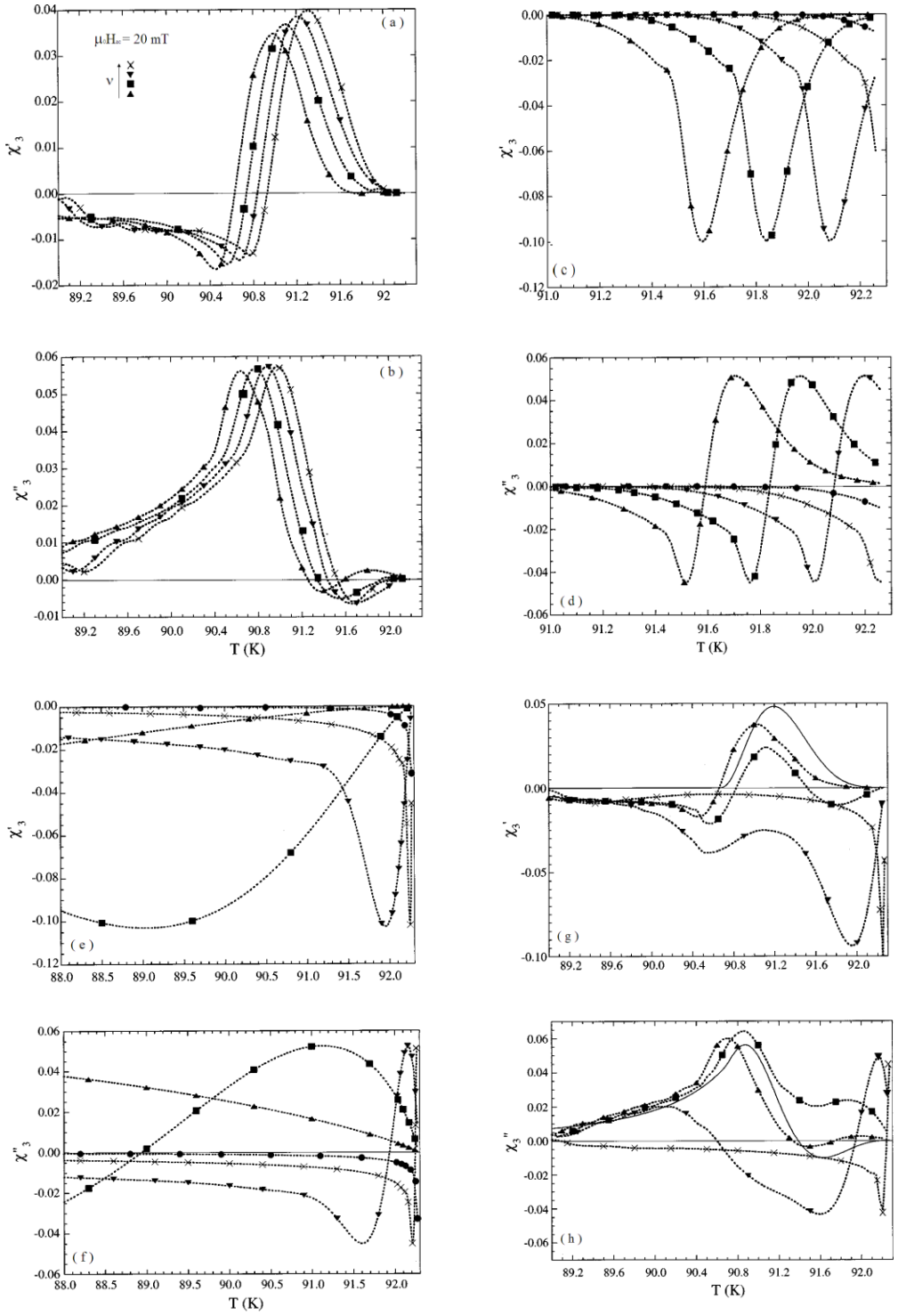

Figure. II.5 Plot of the curves of (up) $\chi_3'(T)$ and (down) $\chi_3''(T)$ numerically calculated for a YBCO slab by solving the diffusion equation where the flux diffusivity has been determined by using the (a,b) flux creep, (c,d) taff, (e,f) flux flow and (g,h) creep-flow parallel resistivities, in absence of DC field (from Ref.[35]). These curves have been acquired with the cosine reference of the lock-in.

Bibliography

[1] F. Gomory, Supercond. Sci. Technol., 10(1997) 523 and references therein.

[2] A. M. Campbell, J. Phys. C: Solid State Phys., 2 (1969) 1492.

[3] R. W. Rollins, H. Kupfer and W. Gey, J. Appl. Phys., 45 (1974) 5392.

[4] D. J. Griffiths, C. C. Koch and J. P. Charlesworth, Phil.Mag., 33 (1976) 505.

[5] E. Maxwell M. Strongin, Phys. Rev. Lett., 10 (1963) 212.

[6] T. Ishida and H. Mazaki, Phys. Rev. B, 20 (1979) 131.

[7] J. R. Clem in Magnetic Susceptibility of Superconductors and Other Spin Systems (New York: Plenum, 1991) p. 177.

[8] A. M. Campbell, IEEE Trans. Appl. Supercond., 5 (1995) 682.

[9] R. A. Hein, T. L. Francavilla and D. H. Liebenberg, Magnetic Susceptibility of Superconductors and Other Spin Systems (New York: Plenum, 1991) and references therein.

[10] P. L. Gammel, L.F. Schneemeyer, J.V. Wasczak, D.J. Bishop, Phys. Rev. Lett., 61 (1998) 1666.

[11] D. E. Farrel, J.P. Rice, D.M. Ginsberg, Phys. Rev. Lett., 67 (1991) 1165.

[12] M. Polichetti, M.G. Adesso, S. Pace, Eur. Phys. J. B, 36 (2003) 27. [30] M.J. Qin, C. K. Ong, Phys. Rev. B, 61 (2000) 9786.

[13] M. Polichetti, M.G. Adesso, T. Di Matteo, A. Vecchione, S. Pace, Physica C, 332 (2000) 378.

[14] M. Polichetti, M.G. Adesso, S. Pace, Physica C, 401 (2004) 196.

[15] C. P. Bean, Phys. Rev. Lett., 8 (1962) 250.

[16] C. P. Bean, Rev. Mod. Phys., 36 (1964) 31.

[17] Y. B. Kim, C. F. Hempstead, A.R. Strnad, Phys. Rev., 129 (1963) 528.

[18] Y. B. Kim, Phys. Rev. Lett., 9 (1962) 306.

[19] R. Prozorov, A. Shaulov, Y. Wolfus and Y. Yeshurun, Phys. Rev. B, 52 (1995) 1254.

[20] P. H. Kes, J. Aarts, J. van den Berg, C. J. van der Beek and J. A. Mydosh, Supercond. Sci. Technol., 1 (1989) 242.

[21] F. London, Superfluids vol 1 (New York: Dover,1961)

[22] A. M. Campbell , J. Phys. C: Solid State Phys., 4 (1971) 3186.

[23] R. Labusch Cryst. Lattice Defects, 1 (1969) 1.

[24] R. B. Goldfarb, M. Lelental, C. A. Thompson, in: R. A. Hein, T. L. Francavilla, D. H. Liebenberg (Eds.), Magnetic Susceptibility of Superconductors and Other Spin Systems (Plenum, New York, 1991), p. 49.and references therein.

[25] R. Kubo, M. Toda and N. Hashitsume, Statistical PhysicsII: Nonequilibrium Statistical Mechanics (Berlin: Springer, 1991) pp. 120–5.

[26] S. Havriliak and S. Negami, J. Polym. Sci., C (1966) 14 99.

[27] G. Prando et al., J. Phys.: Condens. Matter, 25 (2013) 505701.

[28] G. Prando, P. Carretta, R. De Renzi, S. Sanna , A. Palenzona, M. Putti and M. Tropeano, Phys. Rev. B, 83 (2011) 174514.

[29] G. Prando, P. Carretta, R. De Renzi, S. Sanna , H. J. Grafe, S.Wurmehl and B. Büchner, Phys. Rev. B, 85 (2012) 144522.

[30] D. Mancusi, M. Polichetti, M. R. Cimberle and S. Pace, Supercond. Sci. Technol., 28 (2015) 095017.

[31] A. Rydh, Ö. Rapp and M. Andersson, Phys. Rev. Lett., 83 (1999) 1850.

[32] A. M. Campbell, Magnetic Susceptibility of Superconductors and Other Spin Systems ed R A. Hein, T. L. Francavilla and D. H. Liebenberg (New York: Plenum, 1991) p. 129.

[33] J. R. Clem, J. Appl. Phys., 50 (1979b) 3518.

[34] R. Grissen, W. Hai-hu, A.J.J. van Dalen, B. Dam, J. Rector, H.G. Schnack, S. Libbrecht, E. Osquiguil, Y. Bruynseraede, Phys. Rev. Lett.,72 (1994) 1910.

[35] D. Di Gioacchino, F. Celani, P. Tripodi, A.M. Testa, S. Pace, Phys. Rev. B, 59 (1999) 11539.

Chapter III

Analysis of the temperature dependent AC susceptibility harmonics of the $Bi_4O_4S_3$ bulk sample

In this chapter we will illustrate the method for analyzing the temperature dependent AC susceptibility harmonics and investigate the superconducting and magnetic properties of a superconducting sample. At this aim, we analyze the experimental curves of the first and third harmonics of the superconducting bismuth-oxysulfide layered compound $Bi_4O_4S_3$[1]. This material has a layered crystal structure based on stacking layers of BiS_2 and $Bi_4O_4(SO_4)_{1-x}$, where x indicates the deficiency of SO_4^{2-} ions at the interlayer sites[1-4]. The T_c of $Bi_4O_4S_3$ was found to be around 4.5 K, and other compounds with a layered structure based on the BiS_2 layer and $ReO_{1\_x}F_x$ (La, Ce, Pr, Nd) block layers have been discovered with $T_c \sim 10$ K[6-11]. The doping mechanism in these systems is similar to those of cuprates and Fe-based pnictides, suggesting that the BiS_2 plays the role of the CuO_2 layer in the cuprates and of the FeX layer in the Fe-based pnictides. This explains the interest of investigate the BiS_2-based superconductors which could be designed also to provide additional information for the comprehension of the superconductivity mechanisms in both cuprates and iron based superconductors.

The temperature dependence of both the first and the third AC susceptibility harmonics have been measured on a $Bi_4O_4S_3$ sample in form of a slab by using the AC insert of a 9 T Quantum Design PPMS. This sample was prepared by the solid state reaction method starting from Bi_2S_3, Bi_2O_3 powders and S grains and by using thermal treatments up to 510 °C[2]. The AC susceptibility measurements were performed by applying magnetic fields parallel to the sample surface, at different AC field frequencies (ν = 107, 1077, 5385, 9693 Hz) and amplitudes ($\mu_0 H_{ac} = 0.05, 0.1, 0.2, 0.4, 0.8, 1.2$ mT), both in absence and in presence of a DC field ($\mu_0 H_{dc} = 2, 5, 10, 100$ mT).

III.1 Analysis of the temperature dependent AC susceptibility first harmonic

The curves of χ_1' and χ_1'' as function of temperature are reported in the Figs.II.1a and II.1b in absence of a DC field with varying the amplitude of the AC field and at a fixed AC field amplitude with varying the superimposed DC field, respectively. The superconducting transition of the $\chi_1'(T)$ curve broadens and its step-like transition becomes smoother as the AC field amplitude is increased, as expected in the critical state models due to the effect of the field which tends to destroy the superconductivity[14,15]. However, the broadening of the transition in the curve of $\chi_1'(T)$ is accompanied by a shift

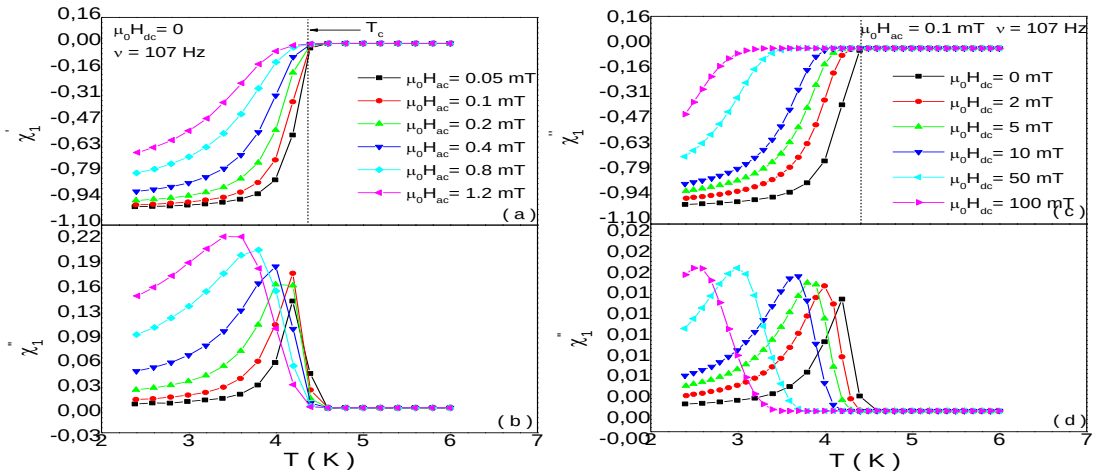

Figure. III.1 Experimental curves of the $\chi_1^{'}(T)$ and $\chi_1^{''}(T)$ curves of the $Bi_4O_4S_3$ sample: (a), (b) plots show the $\mu_0 H_{ac}$ dependence of the real $\chi_1^{'}(T)$ and imaginary $\chi_1^{''}(T)$ part, respectively, in absence of DC field and at a fixed AC frequency with the vertical line indicating the critical temperature determined as the onset temperature of the transition in the $\chi_1^{'}(T)$ at the lowest value of $\mu_0 H_{ac}$; (c), (d) plots show the $\chi_1^{'}(T)$ and $\chi_1^{''}(T)$ curves at fixed AC field amplitude and frequency, and with varying the superimposed DC field, with the horizontal line indicating the transition to the normal state[1].

to lower temperature and a rise of the dissipation peak in the curve of $\chi_1^{''}(T)$. In fact, the peak is expected when the external field penetrates the center of the sample. Then, as the AC field is increased this can occur in correspondence to a stronger pinning that is at a lower temperature. This suggests the existence of nonlinear flux dynamical regimes governing the AC responses in both the intergranular links and the individual grains. The effect of the DC field is the further broadening of the superconducting transitions in the $\chi_1^{'}(T)$ curves and the larger shift of both the $\chi_1^{'}(T)$ and $\chi_1^{''}(T)$ curves towards lower temperatures.

III.1.1 Estimation of the superconducting critical temperature T_c and field H_c

First of all, information about the superconducting transition of the $Bi_4O_4S_3$ sample can be extracted from the analysis of the temperature dependent real part of the susceptibility first harmonic. In fact, crossing the $H_{c1}(T)$ line towards higher temperature and fields destroy the full shielding of the Meissner state observed in absence of field. Then, it is expected

$$\chi_1{}^{'} = -1, H \leq H_{c1}(T), \quad \text{(III.1a)}$$

$$\chi_1{}^{'} = -\frac{H_{c1}}{H_{dc}}, H \geq H_{c1}(T), \quad \text{(III.1b)}$$

$$\chi_1{}^{''} = 0, \quad \text{(III.1c)}$$

where H is the external magnetic field containing a static and an alternate field components. Then, according to the Eq. (II.5a), the superconducting transition is accompanied by a drop in the curve of the temperature dependence of $\chi_1'(T)$ from the value -1 in the full shielding state to the zero value in the normal state with increasing temperature from $T = 0$ towards T_c and magnetic field from $H = 0$. towards H_{c1}. On the other hand, since crossing H_{c2} should be accompanied by a sharp change in the linear resistivity, H_{c2} can be determined by analyzing the shift of the onset temperature in the linear regime (see the Figs. III.2a and III.2b).

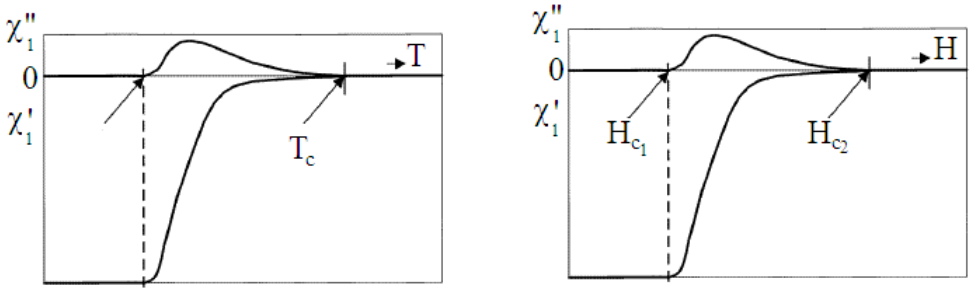

(a) (b)

Figure. III.2 Schematic diagram of the dependence of the first harmonics susceptibilities on (a) temperature and (b) the external DC field for determining the lower and upper critical fields.

Although most precise superconducting critical temperature and the fields may be estimated from the AC susceptibility first harmonic measured as function of temperature and magnetic field, respectively, both them can be also estimated from the temperature dependent AC susceptibility. The critical temperature of the $Bi_4O_4S_3$ sample has been taken T_c~4.5 K from the onset of the temperature derivative of the $\chi_1'(T)$ in absence of DC field in the Fig. III.1a at the lowest amplitude of the applied AC field. Since T_c increases with increasing H_{dc} and H_{ac} the DC and AC H-T lines have been constructed from the Figs. I.1a and I.1c, respectively, by taking the values of T_c from the curves of $\chi_1'(T)$ and the corresponding value of the AC and DC field amplitudes. The plot of $\mu_0 H_{dc}(T_c)$ is reported in the Fig. III.3a and exhibits the negative rate expected for a type II superconductor described in the Chapter I. However, there is an upward curvature at lower temperatures in the plots of Fig. III.3a which cannot be described within neither the conventional power law expressions described nor the WHH theory[12] described in the Chapter II. On the other hand, such kind of enhanced upper critical field could be related to a two-gap superconductivity in the $Bi_4O_4S_3$ compound which also exhibits some properties typical of nonconventional coupling mechanisms. In fact, the data of $\mu_0 H_{dc}(T_c)$ in the Fig. II.3a have been described within the dirty two-gap

superconductivity theory treated in the Chapter II, with parameters values $\eta \approx 10^{-4}$, $\lambda_{11} \approx \lambda_{22} \approx 0, \lambda_{12} \approx \lambda_{21} \approx 0.8$ [12,13].

It is worth noting that in absence of DC field the curves of $\mu_0 H_{ac}(T_c)$ have been taken as the effective AC field amplitudes determining the superconducting transition and so playing the role of effective upper critical fields[14]. The plot of $\mu_0 H_{ac}(T_c)$ for the $Bi_4O_4S_3$ sample are reported in the Fig. III.3b and exhibits a double behavior which could indicate both the existence of two different phases in the superconducting sample consisting of strongly superconducting grains not completely coherent but joined by weakly superconducting links having a smaller critical field or a change in the flux dynamical regime governing the AC response.

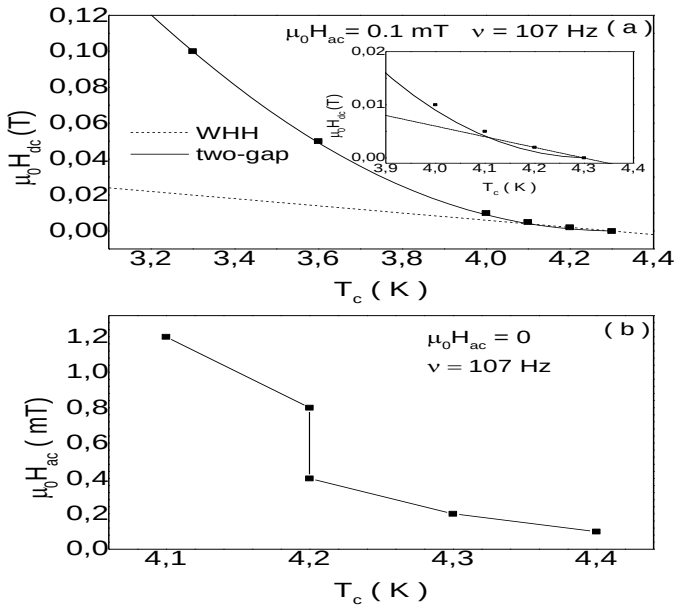

Figure. III.3 The *H-T* lines constructed by taking the values of T_c and the corresponding value of (a) H_{dc} and (b) H_{ac} in the curves of $\chi_1'(T)$ of the Figs. II.1a and II.1c, respectively. The lines in (a) are the data fit within (dash) the dirty one-gap theory (WHH) model in the region near T_c and (solid) the dirty two-gap theory, with an enlargement of this area reported in the inset.

III.1.2. Estimation of the critical current density j_c

When considering a constant current-carrying capability through the superconducting sample, a rough method to estimate the critical current density j_c can be performed by analyzing the curves of the temperature dependent susceptibility first harmonic imaginary part $\chi_1''(T)$ measured at different amplitudes of the AC field. In fact, within the Bean model[15,16] the dissipation peak in the $\chi_1''(T)$ is expected to occur at a particular value of the AC field penetration depth, i.e.

$$\mu_0 H_{ac} = \sqrt{2}\mu_0 j_c L, \qquad \text{(III.2)}$$

for a slab of width $2L$. Then, the temperature dependence of j_c can be obtained by taking the temperature T_p of the peak position in the $\chi_1''(T)$ curves measured at different AC field amplitudes, and the corresponding values of the AC field amplitude. As an example, the estimation of the $j_c(T)$ curve of the $Bi_4O_4S_3$ sample, based on the analysis of the corresponding $\chi_1''(T)$ curves measured at different AC field amplitudes and shown in the Fig. III.1b, is reported in the Fig. III.4a for different DC fields. The j_c decrease with increasing temperature as expected for a type II superconductor and described in the Chapter I. In particular, an exponential decay law has been found to describe the data rather than the different power law dependences described in the Chapter I. Moreover, by taking isothermal cuts of the $j_c(T)$ curves at different DC field amplitudes in the Fig. III.4a allowed us to construct the AC field dependence of the critical current density. These curve of $j_c(H_{dc})$ are reported in the Fig. III.4b for different temperatures and have been fitted with a power law $j_c(H_{dc}) \sim {H_{dc}}^{-\beta}$. This is compatible with the existence of

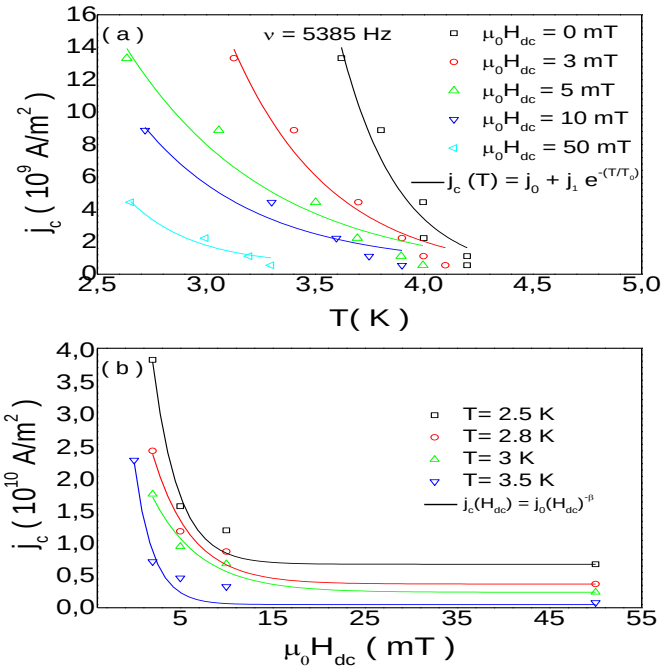

Figure. III.4 (a) Plot of $\mu_0 j_c$ as function of the temperature at different DC fields, for the $Bi_4O_4S_3$ sample, extracted from the curves of Fig. III.1b by taking the value of the temperature of the dissipation peak position and the value of the j_c for the corresponding value of H_{dc} according to the Eq. (III.2). The line are the fit with an exponential decay. (b) Dependence of j_c on the DC field obtained by performing isothermal cuts of the curves of the Fig. III.3a at different temperature. The lines are the fit with the power law $j_c(H_{dc}) \sim {H_{dc}}^{-\beta}$ [1].

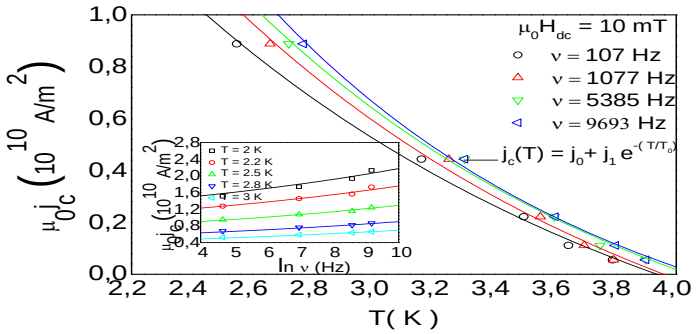

Figure. III.5 Plot of $\mu_0 j_c$ as function of the temperature at different frequencies, for the $Bi_4O_4S_3$ sample, constructed as in the Fig. III.4a at different AC field frequencies and at a fixed DC field. The lines are the fit with an exponential decay. Inset: Dependence of j_c on $\ln \nu$ obtained by taking isothermal cuts of the curves of $j_c(T)$ at different temperatures. The lines are the fit with the Eq. (III.3)[1].

flux creep phenomena and the field dependence of the $\chi_1^{'}(T)$ and $\chi_1^{''}(T)$ curves discussed above. Moreover, the existence of creep phenomena is confirmed from the frequency dependence of the critical current density obtained by taking isothermal cuts of the $j_c(T)$ curves constructed at different AC field frequencies and at a fixed DC field shown in the Fig. III.5. The curves of $j_c(\ln \nu)$ at different temperatures are reported in the inset of the Fig. III.5 and have been described with a collective creep law[17]

$$j_c(\nu) = j_c(T, H_{dc}) \left[\frac{k_B T}{U(T,H_{dc})} \ln \frac{\nu_0}{\nu}\right]^{\frac{1}{\mu}}, \qquad \text{(III.3)}$$

with the exponent $\mu \approx 0.6$ as expected for the creep of large flux bundles[18].

III.1.3. Vortex activation energy U_a

Generally, an effective activation energy for thermally activated motion of vortices inside a superconducting sample is defined as $U_a = U_a(T, H_{dc}, j)$. In particular, it has been said in the Chapter I that in the linear thermally activated flux flow regime the magnetic flux inside the sample decays exponentially with a frequency-dependent length scale $\delta(T) = [2D(T)/\omega]^{1/2}$, where $D(T)$ is the magnetic diffusivity. This produces the occurrence of a peak in the imaginary part of the temperature dependent AC susceptibility first harmonic $\chi_1^{''}(T)$ when δ matches the typical dimensions of the sample. Since the magnetic flux diffusion time satisfies the relation $\tau \sim L^2/D$, with $2L$ the characteristic specimen dimension, it turns out that the maximum in the $\chi_1^{''}(T)$ is reached at frequencies $\tau \sim \nu^{-1}$ with ν the measuring frequency, that is the flux relaxation velocity of the form (I.12) matches the measured frequency. This gives the Arrhenius[18] law

$$\nu = \nu_0 e^{-\frac{U_a}{k_B T}}. \quad \text{(III.4)}$$

where ν_0 is a constant with dimension of frequency. In the case of taff regime, the activation energy U_a meanly depends on the temperature. On the other hand, when flux creep phenomena are present, U_a depends on both temperature, and magnetic field and driving current. In fact, the flux line are typically considered as a particle moving in a force field created by the potential wells at pinning sites, and the unperturbed pinning potential U_0 becomes the effective activation energy $U_a = U_0(1 - j/j_c)$ due to the magnetic flux gradient. In this case, the creep velocity is considered to match the inverse of the AC field frequency in correspondence of the dissipation peaks in the $\chi_1''(T)$ curves, thus giving the Arrhenius behavior of the Eq. (III.4). Although such resonance between the frequencies of the driving AC field and the microscopic vortices oscillation in the pinning wells reveals very useful for the extraction of the activation energy and flux dynamical information from the analysis of the AC susceptibility data by means of the Arrhenius law Eq. (III.6), it is worth noting that the oscillation frequencies of vortices in the wells of the pinning sites are very high thus requiring very high measuring frequencies of the external AC field.

However, the Eq. (III.6) achieves a method for the estimation of U_a, for the taff and flux creep regimes, from the analysis of the frequency behavior of the temperature dependent AC susceptibility first harmonic imaginary part. According to the Eq. (III.6), since the velocity is expected to match the AC field frequency at the temperature T_p of the dissipation peak in the $\chi_1''(T)$ curves, the effective activation energy U_a can be estimated from the slope of the Arrhenius plot of $\ln(\nu)$ as function of $1/T_p$. These plots can be constructed starting from the curves of $\chi_1''(T)$ measured at different AC field frequencies ν by taking the temperature of the peak position T_p and the corresponding value of $\ln(\nu)$.

As example, the Arrhenius plots for the $Bi_4O_4S_3$ sample at different DC fields are shown in the Fig. III.6. The DC field dependence of U_a, constructed by taking slopes of the Arrhenius plots at different DC fields, is shown in the Fig. III.7a, for different values of the AC field amplitude. A power law dependence $U_a \sim (\mu_0 H_{dc})^{-\alpha}$, characteristic of the collective flux creep, is observed at higher AC and DC fields with $\alpha \approx$ 0.3-0.6, while an exponential decay law is observed in the lower AC and DC fields region. On the other hand, the intercept $\ln(\nu)$ of the Arrhenius fits as function of U_a at different values of the AC field amplitude $\mu_0 H_{ac}$, are shown in the Fig. III.7b, where a linear dependence of $\ln(\nu)$ on (U_a) is clearly visible. According to the Eq. (III.6), this linear dependence implies a linear temperature dependence of U_a with a law $U_a(T) \sim 1 - T/T_c$. By considering the Arrhenius plots at different AC fields, the dependence of U_a $\mu_0 H_{ac}$ can

be also extracted. The curves of $U_a(\mu_0 H_{ac})$ at different DC fields are reported in the Fig. III.8. The figure shows that U_a decreases with increasing $\mu_0 H_{ac}$ with a power law $U_a \sim (\mu_0 H_{ac})^{-\mu}$ and $\mu = 0.4$-0.6, expected in the collective flux creep of large flux bundles and in agreement with the previous results.

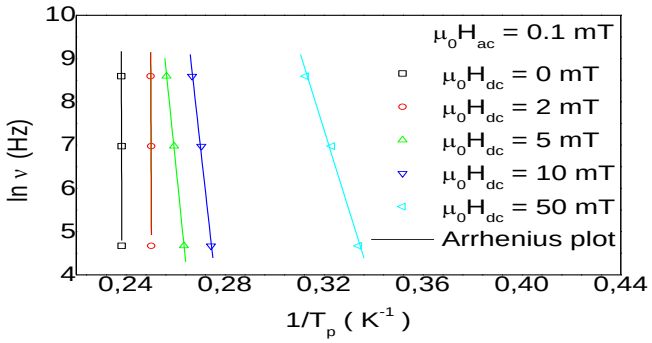

Figure. III.6 Plot of $\ln(\nu)$ as function of the inverse of the peak position temperature T_p in the $\chi_1''(T)$ curves for the $Bi_4O_4S_3$ sample. obtained from the curves at different frequencies by taking T_p and the value of the frequency. The lines are the fit of the data to an Arrhenius[23] law of the Eq. (III.6) with slope U_a and intercept $\ln(\nu_0)$[1].

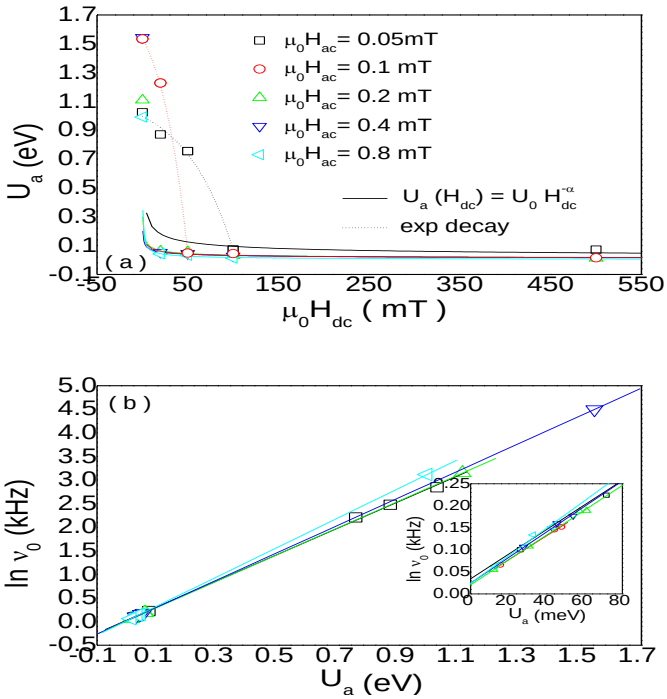

Figure. III.7 (a) Dependence of the effective activation energy U_a on $\mu_0 H_{dc}$, for the $Bi_4O_4S_3$ sample, obtained from the slopes of the Arrhenius plots at different $\mu_0 H_{dc}$ values in the Fig. III.6, for different AC field amplitudes. The lines are the fit with (solid) a power law $U_a \sim (\mu_0 H_{dc})^{-\alpha}$ with $\alpha = 0.3$-0.6 and (dashed) an exponential decay. (b) Variation of the intercept $\ln \nu_0$ of the Arrhenius fit lines with the slopes U_a. The linear behaviour implies a linear dependence of U_a with the temperature. Inset: zoom at low U_a values[1].

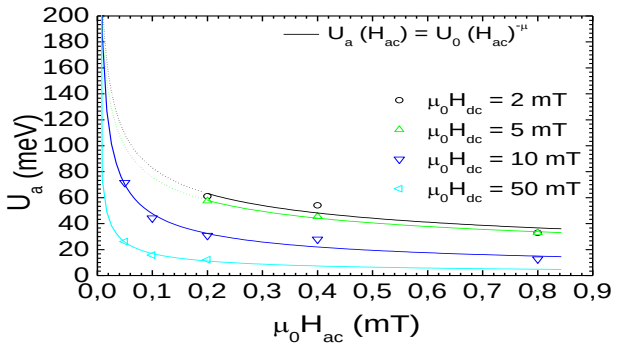

Figure. III.8 Dependence of the effective activation energy U_a on $\mu_0 H_{ac}$, for the $Bi_4O_4S_3$ sample, obtained from the slopes of the Arrhenius plots at different $\mu_0 H_{ac}$ values. The data are fitted with a power law $U_a \sim (\mu_0 H_{ac})^{-\mu}$ with μ = 0.4-0.6[1].

III.2 Analysis of the temperature dependent AC susceptibility third harmonic

As discussed in the Chapter II, a combined analysis, based on the analysis of both the fundamental and higher harmonics of the AC magnetic susceptibility can be used to detect information about the pinning mechanisms, the existence of geometric barriers to the flux penetration, and the dynamical regimes, governing the magnetic response and the phase of the vortex matter of a type II superconducting sample [19-21]. In the following, the temperature dependent AC susceptibility third harmonic of the $Bi_4O_4S_3$ sample will be analyzed in order to obtain information about the flux dynamics and pinning mechanisms governing the sample AC response by means of the comparison of the field and frequency behaviours of the measured third and first harmonics curves, and of the measured third harmonics curves with the theoretical curves of bulk samples reported in literature for different flux dynamical regimes[19].

First of all, we repeat that in the Bean[15,16] critical state mode, for a slab geometry, the real part of the third harmonic $\chi_3'(T)$ is zero below the $\chi_1''(T)$ peak temperature T_p, and shows a positive peak above T_p, while the imaginary part $\chi_3''(T)$ shows an oscillatory behaviour displaying a positive peak at about T_p and a negative one at higher temperatures[20] (see the Fig. II.4). Moreover, variations in the temperatures of the peak maxima of $\chi_1''(T)$ and $|\chi_3(T)|$ can be reproduced in the critical state model by considering a critical current density $j_c(\nu)$ that increases with the frequency ν of the AC field, due to the existence of relaxation phenomena. However, the general shape of both the first and the higher AC susceptibility harmonics is independent of the frequency of the AC field in all the critical state models. On the other hand, variations in the shape of the $\chi_3'(T)$ and $\chi_3''(T)$ and in the height of $\chi_1''(T)$ and $|\chi_3(T)|$ components induced by varying the frequency can be interpreted by means of the comparison with the curves

numerically calculated by solving the diffusion equation of the magnetic field in the sample with for various flux dynamical regimes and pinning mechanisms (see the Figs. II.5a-h)[19-22].

III.2.1 Third harmonic at different AC amplitudes

As an example, Figs. III.9a and III.9b show the curves of $\chi_3'(T)$ and $\chi_3''(T)$ for the $Bi_4O_4S_3$ sample, respectively, measured in absence of DC field, at a fixed AC field frequency and with varying the amplitude $\mu_0 H_{ac}$. It is worth noting that the sign of the measured curves have been inverted since in order to compare them with the theoretical curves reported in literature and according to the sign inversion rules for different acquisition lock-in reference signals discussed in the Chapter II (see the Eqs.(II.21a)-(II.21d)).

The curves of $\chi_3'(T)$ and $\chi_3''(T)$ of the $Bi_4O_4S_3$ sample exhibit a noticeable dependence on $\mu_0 H_{ac}$.. In particular, non zero values are present in the $\chi_3'(T)$ curves for $T < T_p(\chi_1'')$, which indicates the existence of flux dynamical regimes governing the AC magnetic response. Moreover, the curves of $\chi_3'(T)$ exhibit a positive maximum closer to T_c at lower H_{ac}. values, which shifts towards lower temperatures with increasing H_{ac} with a nonmonotonic variation of the peak height. Correspondingly, a minimum tends to emerge with at lower temperatures. This confirms the existence of flux dynamic effects in the AC magnetic response, together with the frequency dependence of the shape of the $\chi_3'(T)$ and $\chi_3''(T)$ curves which will be discussed later.

On the other hand, the curves of $\chi_3''(T)$ exhibit a small negative minimum close to the temperature $T_{on}(\chi_3')$ of the onset of $\chi_3'(T)$, as it is expected from the Bean critical state model[20,21]. Then, more detailed information about the coexistence of the critical state and flux dynamical regimes has been obtained by analyzing the AC amplitude behavior of the $\chi_3'(T)$ and $\chi_3''(T)$ curves measured in presence of a DC field $H_{dc} \gg H_{ac}$. In fact, since the taff and flux flow regimes are both linear (AC field independent) in presence of a DC field $H_{dc} \gg H_{ac}$, the evidence of non linearity in the $\chi_3'(T)$ and $\chi_3''(T)$ curves in presence of strong DC field, when the field is almost constant, could suggest the exclusion of the two regimes effects in the AC magnetic response thus due only to the nonlinear creep regime and to hysteretic phenomena[17]. In fact, the curves of $\chi_3'(T)$ and $\chi_3''(T)$ for the $Bi_4O_4S_3$ sample are shown in the Figs. III.10a and III.10b, respectively, measured in presence of different strong DC fields, at fixed AC frequency and AC field amplitude. Both the $\chi_3'(T)$ and $\chi_3''(T)$ curves depend on the DC field confirming the existence of flux creep phenomena. It is worth noting that also a nonlinear contribution

due to the flux flow regime could contribute to the nonlinearity of the AC magnetic response by means of the interaction between vortices if the DC field is close to the upper critical field of the sample[22].

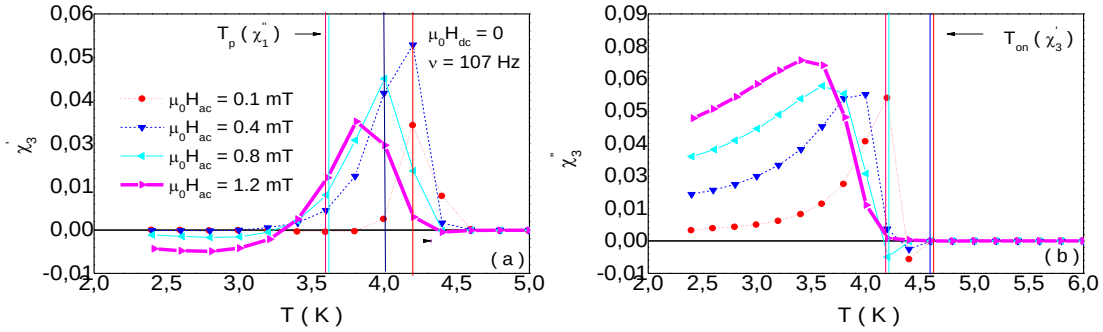

Figure. III.9 Plot of the experimental curves of (a) $\chi_3^{'}(T)$ and (b) $\chi_3^{''}(T)$, for the $Bi_4O_4S_3$ sample, measured in absence of DC field, at a fixed AC frequency with varying the AC amplitude $\mu_0 H_{ac}$. The sign of the curves has been inverted in order to compare them with theoretical curves for a different acquisition reference signal according to the Eqs. (II.21a)-(II.21d). The vertical lines indicate the temperatures T_p of the peaks in the corresponding curves of $\chi_1^{''}(T)$ in the Fig. II.1b[1].

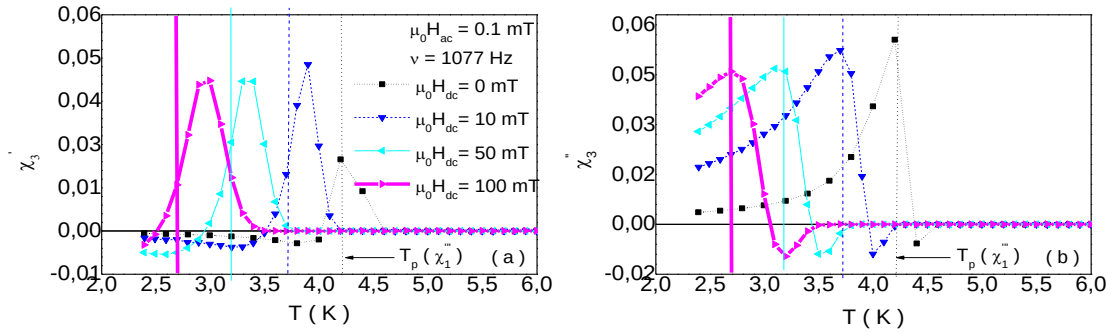

Figure. III.10 Plot of the experimental curves of (a) $\chi_3^{'}T)$ and (b) $\chi_3^{''}(T)$, for the $Bi_4O_4S_3$ sample, measured at fixed AC frequency and amplitude, in presence of a DC field $H_{dc} \gg H_{ac}$. The sign of the curves has been inverted in order to compare them with theoretical curves for a different acquisition reference signal according to the Eqs. (II.21a)-(II-21d). The vertical lines indicate the temperatures T_p of the peaks in the corresponding curves of $\chi_1^{''}(T)$ in the Fig. II.1d[1].

III.2.2 Third harmonic at different ac frequencies

In order to complete the study of the flux dynamical and pinning regimes governing the AC magnetic response of the $Bi_4O_4S_3$ sample from the third harmonic susceptibility curves, the AC field amplitude dependence of these curves can be usefully combined with the analysis of their frequency behavior. At this aim, the $\chi_3^{'}(T)$ and $\chi_3^{''}(T)$ curves for the

$Bi_4O_4S_3$ sample in absence of DC field, at a fixed AC field amplitude with varying the AC field frequency are shown in the Figs. III. 11a and III.11b, respectively. The frequency behavior of these curves can be compared with the frequency dependence of the corresponding curves numerically calculated by solving the diffusion equation for different flux dynamical regimes. These curves for the flux flow, taff, flux creep and creep-flow parallel regimes have been discussed in detail in the Chapter II and are reported in the Figs. III.12a-h[19]. From the comparison of the curves of the Figs. (III.11) and (III.12) the evidence of the existence of a regime of parallel between the flux creep and flux flow inside the sample has been found. In fact, as observed in the theoretical curves, a negative peak occurs in the experimental $\chi_3'(T)$ and $\chi_3''(T)$ curves at lower temperatures, followed by a positive peak at the peak temperature of $\chi_1'(T)$, with the negative peak height and position increasing and the positive peak height decreasing with increasing frequency. Accordingly, the shape and frequency behavior of the experimental $\chi_3''(T)$ curve is very close to the theoretical prediction for the parallel model at the lower frequency. This result is also in good agreement with the results of the analysis AC susceptibility first harmonic discussed above.

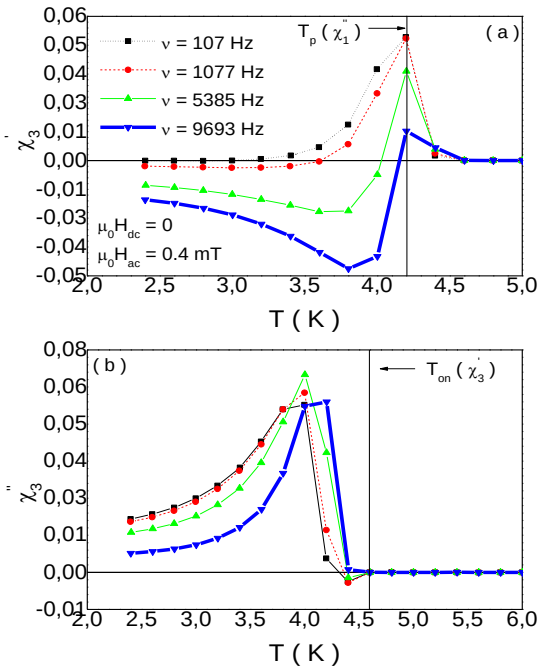

Fig. III.11 Plot of the experimental curves of (a) $\chi_3'(T)$ and (b) $\chi_3''(T)$, for the $Bi_4O_4S_3$ sample, measured in absence of DC field, at a fixed AC amplitude and with varying the AC frequency ν. The sign of the curves has been inverted in order to compare them with theoretical curves for a different acquisition reference signal. The vertical lines indicate the temperatures T_p of the peaks in the corresponding curves of $\chi_1''(T)$[1].

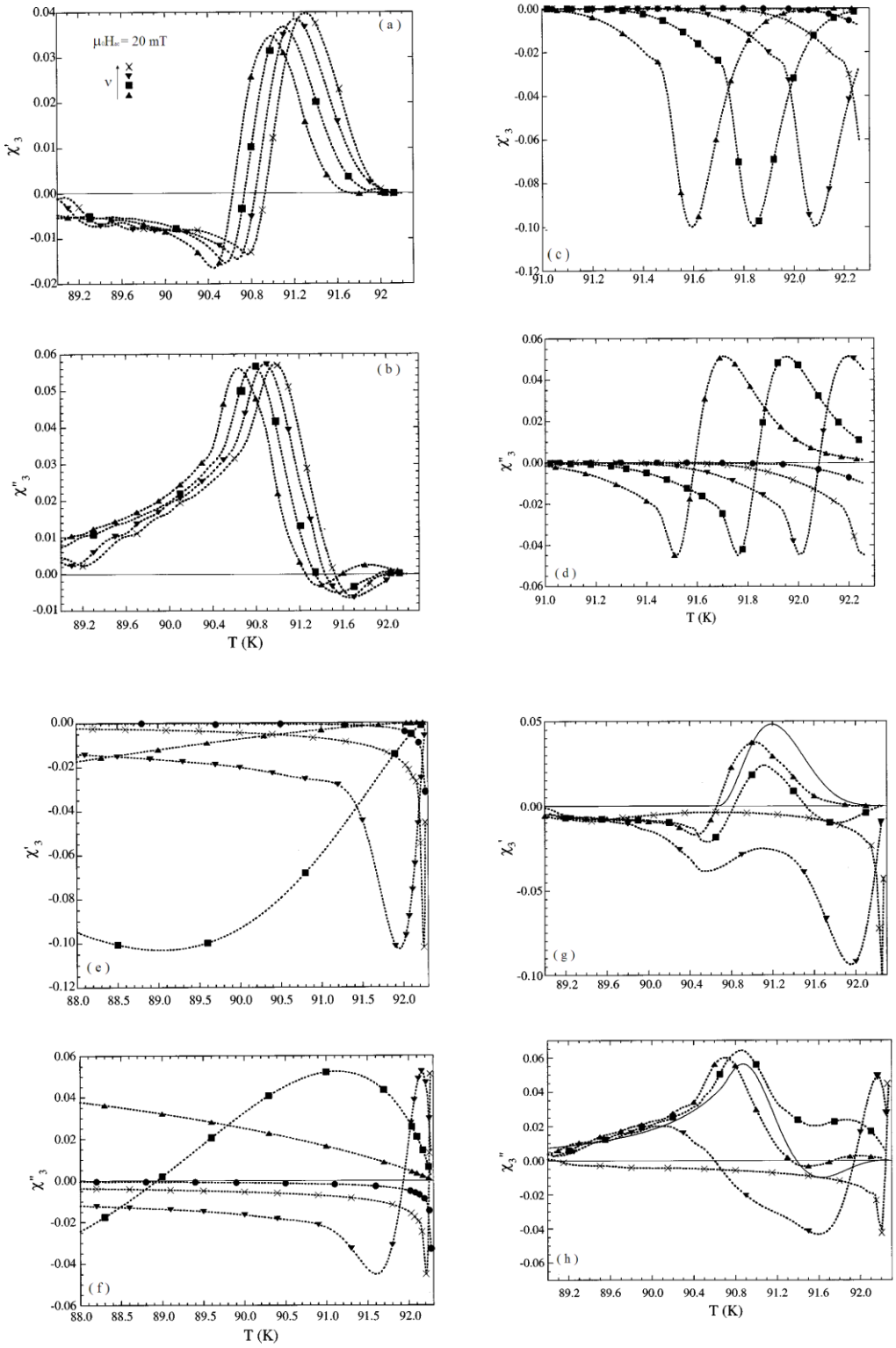

Figure. III.12 Plot of the curves of (up) $\chi_3^{'}(T)$ and (down) $\chi_3^{''}(T)$ numerically calculated for a YBCO slab by solving the diffusion equation where the flux diffusivity has been determined by using the (a,b) flux creep, (c,d) taff, (e,f) flux flow and (g,h) creep-flow parallel resistivities, in absence of DC field (from Ref.[19]). These curves have been acquired with the cosine reference of the lock-in.

Bibliography

[1] D. Mancusi, F. Giubileo, Y. Mizuguchi, S. Pace, M. Polichetti, Physica C, 507 (2014) 47-54.

[2] Y. Mizuguchi, H. Fujihisa, Y. Gotoh, K. Suzuki, H. Usui, K. Kuroki, S. Demura, Y.Takano, H. Izawa, O. Miura, Phys. Rev. B, 86 (2012) 220510(R).

[3] S. K. Singh, A. Kumar, B. Gahtori Shruti, G. Sharma, S. Patnaik, V.P.S. Awana, J. Am. Chem. Soc., 134 (2012) 16504–16507.

[4] R. Jha, V.P.S. Awana, Physica C, 498 (2014) 45–49.

[5] Y. Mizuguchi, S. Demura, K. Deguchi, Y. Takano, H. Fujihisa, Y. Gotoh, H. Izawa, O. Miura, J. Phys. Soc. Jpn., 81 (2012) 114725.

[6] S. Demura, Y. Mizuguchi, K. Deguchi, H. Okazaki, H. Hara, T. Watanabe, S.J.Denholme, M. Fujioka, T. Ozaki, H. Fujihisa, Y. Gotoh, O. Miura, T. Yamaguchi, H. Takeya, Y. Takano, J. Phys. Soc. Jpn., 82 (2013) 033708.

[7] R. Jha, A. Kumar, S.K. Singh, V.P.S. Awana, J. Supercond. Nov. Magn. 26 (2013) 499.

[8] J. Xing, S. Li, X. Ding, H. Yang, H.H. Wen, Phys. Rev. B, 86 (2012) 214518.

[9] C. I. Sathish, H. L. Feng, Y. Shi, K. Yamaura, arXiv:1208.2818v3 (2013).

[10] W. A. Phelan, D. C. Wallace, K. E. Arpino, J. R. Neilson, K. J. Livi, C. R. Seabourne, A. J. Scott, T. M. McQueen, J. Am. Chem. Soc., 135 (2013) 5372.

[11] C. Morice, E. Artacho, S.E. Dutton, D. Molnar, H.J. Kim, S.S. Saxena, arXiv:1305.1201v1 (2013).

[12] N. R. Werthamer, E. Helfand and P. C. Hohenberg,. Phys. Rev., 147 (1966) 295-302.

[13] A. Gurevich, Phys. Rev., 67 (2003) 184515.

[14] D. Mancusi, M. Polichetti, M. R. Cimberle and S. Pace, Supercond. Sci. Technol. 28 (2015) 095017.

[15] C. P.. Bean, Rev. Mod. Phys., 36 (1964) 31.

[16] R. B. Goldfarb, M. Lelental, C.A. Thompson, in: R. A. Hein, T. L. Francavilla, D. H. Liebenberg (Eds.), Magnetic Susceptibility of Superconductors and Other Spin Systems, (Plenum, New York, 1991), p. 49. and references therein.

[17] G. Blatter et al., Rev. Mod. Phys., 66 (1994) 1125.

[18] M. Nikolo, R. B. Goldfarb, Phys. Rev. B, 39 (1989) 6615.

[19] D. Di Gioacchino, F. Celani, P. Tripodi, A.M. Testa, S. Pace, Phys. Rev. B, 59 (1999) 11539.

[20] M. Polichetti, M.G. Adesso, T. Di Matteo, A. Vecchione, S. Pace, Physica C, 332 (2000) 378.

[21] M. Polichetti, M. G. Adesso, S. Pace, Physica C, 401 (2004) 196.

[22] Y. B. Kim, C. F. Hempstead, A. R. Strnad, Phys. Rev., 129 (1963) 528.

Chapter IV

The AC magnetic response of granular samples

In the previous chapter the fundamental harmonic of the temperature dependent AC magnetic response of a superconducting homogeneous sample has been analyzed in order to extract several superconducting parameters of the sample and investigate these parameters with varying the external AC and DC fields. Moreover, detailed information about the flux dynamics and the pinning mechanisms which determine the AC magnetic response of the sample have been obtained from the combined analysis of the fundamental and third harmonics of the temperature dependent AC susceptibility and the comparison with the corresponding curves numerically calculated by solving the diffusion equation of the magnetic flux for different flux dynamical and pinning regimes.

However, most high-T_C superconducting materials are in general not a homogeneous continuum but rather consist of a network of superconducting grains with intergranular weak links. In this case, the AC magnetic response of the sample, measured by means of the AC susceptibility technique, consists in the composition of two contributions due to the individual grains and the intergranular links, respectively. In fact, in the case of a sample consisting of superconducting grains representing elementary volumes of the phase coherence of the order parameter, interconnected by a system of weak links[1-4], two shielding currents flow in the plane perpendicular to the external field through paths around the whole sample via the intergranular links and paths around the individual grains, respectively. Then, two steps are expected in the curve of the temperature dependent real part of the AC susceptibility first $\chi_1'(T)$ and two peaks in the curve of the corresponding imaginary part $\chi_1''(T)$, which can be ascribed to the inter. and intragranular magnetic responses, respectively. Since generally the intergranular critical current density is smaller than the intragranular critical current density and because of the smaller dimensions of grains with respect to the whole sample, the peak at lower temperature in the $\chi_1''(T)$ curve has to ascribed to the penetration of the external magnetic field in the centre of the sample accompanied by a corresponding step in the $\chi_1'(T)$ curve, while the field penetrates the centre of the grains in correspondence of the peak at higher temperature in the $\chi_1''(T)$ accompanied by a corresponding step in the $\chi_1'(T)$ curve.

The calculation of the temperature dependent AC magnetic susceptibilities of the inter- and intragranular volume fractions from the whole sample's magnetic response and the analysis of each of the two AC susceptibilities as described in the previous chapter could be useful in order to investigate whether the superconductivity is a bulk or granular

phenomenon and to separate the effects of the external parameters on the superconducting properties and flux dynamics of both the inter- and intragranular components.

In general, the inter- and intragranular magnetic contributions could be extracted from the whole sample magnetization and normalized to the magnetic field in order to determine the corresponding AC susceptibilities. This separation is not always possible due to the overlap of the two magnetic response which are the close the more similar the curves of temperature dependent superconducting critical fields. In this case, the actual magnetic field inductions governing the inter- and intragranular magnetic responses may be considered in order to determine the corresponding AC susceptibilities. In fact, the magnetic interaction between the inter- and intragranular magnetizations due to the demagnetizing factors of both the whole sample and the grains give the existence of effective magnetic field inductions acting on the sample's and grains's surfaces which are different from the applied one. Then, the demagnetizing correction rules expressed from the Eqs. (II.30a) and (II.30b) are not still valid in order to determine the intrinsic magnetizations and AC susceptibilities of the inter- and intragranular volume fractions.

In this chapter, a model will be developed for describing the AC magnetic response of a granular sample in terms of the magnetic contributions due to the individual grains and the intergranular regions of the sample. In particular, such model will take into account the existence of effective magnetic field inductions governing the inter- and intragranular magnetic responses due to both the corresponding demagnetizing factors. This kind of approach will give the possibility of separate the actual inter- and intragranular magnetic contributions first and higher harmonics to the magnetic response measured by means of the AC susceptibility technique, and of determine the corresponding intrinsic susceptibilities.

IV.1 Principle of measurement of the AC response of a granular sample

Granular systems in presence of an external AC field, with and without a superimposed DC field, exhibit a magnetic response containing two contributions due to the individual grains and to the intergranular links, respectively. In fact, these magnetic contributions correspond to two currents shielding the external field, which flow the plane perpendicular to the external field through paths around the whole sample via the intergranular links and around the individual grains, respectively[1-4]. The sample magnetic response can be detected as a whole by means of the AC susceptibility technique described in the Chapter II and whose schematic diagram is reported in the Fig. IV.1a. Here we consider the interior of the sample consisting of an arrangement of rectangular prism-like grains, with the external magnetic field applied parallel to the

broader surface of the sample and of the grains. In this configuration demagnetizing effects on the measured magnetic response of the sample have been taken into account. In fact, due to the non-ellipsoidal shape of the both the sample and the individual grains and to the presence of sharp edges on their surfaces, demagnetizing fields produce a distortion of the applied magnetic field at the sample's surface and grains's surfaces, which can influence the sample AC magnetic response itself.

IV.1.1 Demagnetizing effects on the inter- and intragranular magnetic responses

In the Fig. IV.1a the magnetic field induction acting on the surface of the whole sample is given by

$$B^i(t) = \mu_0\left[H(t) + D^i M(t)\right], \tag{IV.1}$$

where the superscript i indicates that this field is shielded by the intergranular currents, and $D^i M(t)$ is the demagnetizing field due to the reversal of the sample magnetization $M(t)$ with the demagnetizing factor D^i characteristic of the sample geometry. Although this demagnetizing factor depends on position on the sample's surface its average value on the sample's surface can be taken thus giving an average value of the effective field $B^i(t)$[5,6].

On the other hand, in the regions connecting adjacent grains the profile of flux penetration can be modified be the demagnetizing fields arising from adjacent grains due to their demagnetizing factors. In order to determine the effective field induction at the grains's surfaces we consider the diagram of the right side of the Fig. IV.1b, showing a slab of the sample containing a single layer of rectangular prism like grains. The magnetic flux is expected to penetrate a finite depth of the slab due to the shielding currents flowing around the sample. Within this depth individual gains feel a nonzero magnetic field induction thus producing intragranular screening currents. The magnetic field induction acting on the surfaces of the grains around the position $\boldsymbol{r}$ can be expressed as

$$B^g(t, \boldsymbol{r}) = B^i(t) + \frac{m(t,\boldsymbol{r})}{V}, \tag{IV.2}$$

where $m(t, \boldsymbol{r})$ is the total magnetic moment produced at position $\boldsymbol{r}$ by the currents flowing in the sample and shielding the external field, normalized to the sample volume V. In absence of demagnetizing effects due to the shape of the grains, the total magnetic moment $m(t, \boldsymbol{r})$ can be taken as sum of the moments $m^i(t, \boldsymbol{r})$ produced by the

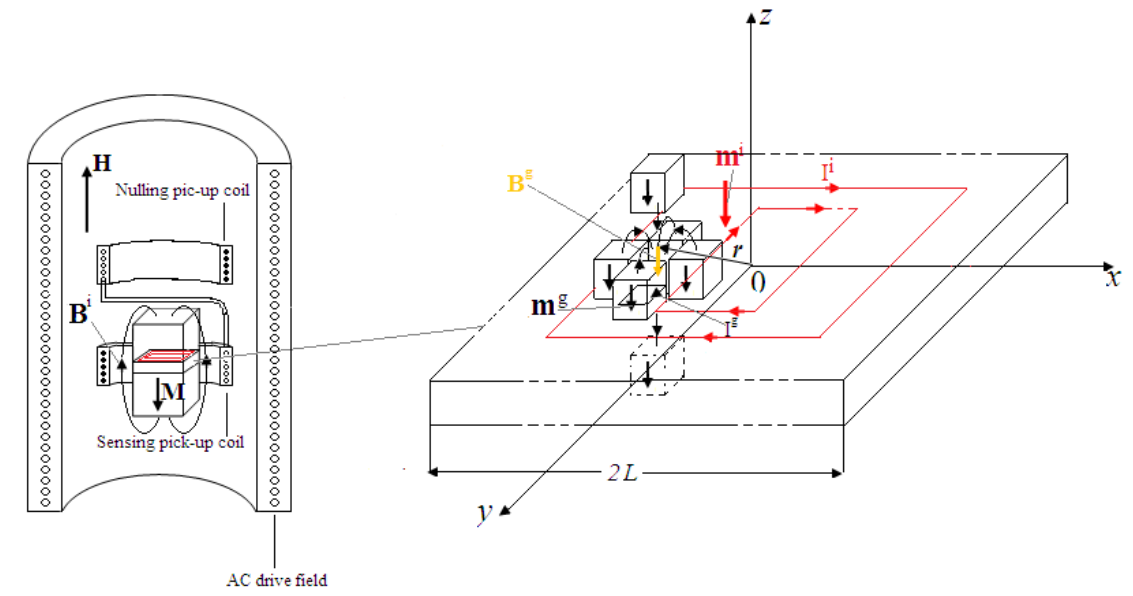

(a)

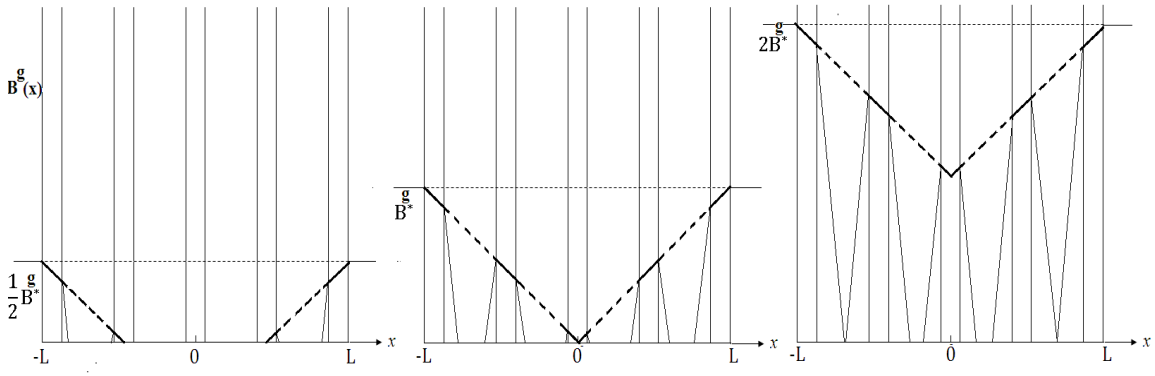

(b)

Figure IV.1 Figure 1. (a) Schematic diagram of the experimental set up for measuring the AC magnetization $\boldsymbol{M}$ of the sample, with $\boldsymbol{B^i}$ the effective magnetic field inductions acting on the sample's surface**.** An enlargement of a slab containing a single layer of grains is shown with the red and black lines indicating the inter- and intragranular shielding currents, respectively, and $\boldsymbol{B^g}$ the effective magnetic field inductions acting on the grains's surfaces due to both the total intergranular magnetic moment $\boldsymbol{m^i}$, and the intragranular magnetic moments $\boldsymbol{m^g}$ via the demagnetizing fields arising from adjacent grains. (b) Schematic diagram of the critical state dependence on position of the effective field inside the sample slab.

intergranular currents at $\boldsymbol{r}$. On the other hand, when considering the demagnetizing effects due to the shape of the grains an additional term has to be considered by taking into account the demagnetizing fields coming from adjacent grains, contained inside both the considered slab and adjacent slabs, in the region between them at position $\boldsymbol{r}$. This field can be taken as

$$B_d^g(t,\boldsymbol{r}) = k_d \frac{m^g(t,\boldsymbol{r})}{V^g}, \qquad \text{(IV.3)}$$

where k_d is an effective demagnetizing factor, and $m^g(t,\boldsymbol{r})$ is the magnetic moment produced at position $\boldsymbol{r}$ by the intragranular currents of an individual grain around $\boldsymbol{r}$, normalized to the volume of the grain V^g. By using the Eq. (IV.3), the Eq. (IV.2) becomes

$$B^g(t,\boldsymbol{r}) = B^i(t) + \frac{m^i(t,\boldsymbol{r}) + k_d n^g m^g(t,\boldsymbol{r})}{V}, \tag{IV.4}$$

which corresponds to an effective total magnetic moment of the sample $m^i(t,\boldsymbol{r}) + k_d n^g m^g(t,\boldsymbol{r})$ with $n^g = V/V^g$.

It is worth noting from the critical state profile of the magnetic flux inside the slab, shown in the Fig. IV.1b, that larger magnetic field inductions act on the outer grains with respect to their inner grains due to the effect of the intergranular shielding currents. Then, in a first approximation, one can consider the averaged value of the magnetic field induction expressed by the Eq. (IV.4) along the slab length in the x and y directions as the effective field governing the intragranular magnetic response. In this case, the Eq. (IV.4) can be written in the form

$$B^g(t) = B^i(t) + M^i(t) + k_d n^g M^g(t), \tag{IV.5}$$

where $M^i(t)$ and $M^g(t)$ are the mean values over the sample volume of the magnetic moments produced by the inter- and intragranular shielding currents on the grains's surfaces, respectively, normalized to the volume V of the sample. Then, since the difference between the internal effective field $B^g(t)$ and the external effective field $B^i(t)$ is the stray field escaping from the sample and acquired by means of the inductive technique of the Fig. IV.1a, from the Eq. (IV.5) the measured magnetic signal is given by

$$M(t) = M^i(t) + k_d n^g M^g(t). \tag{IV.6}$$

The Eqs. (IV.1), (IV.5) and (IV.6) indicate that both the fields $B^i(t)$ and $B^g(t)$ can be expressed in terms of the magnetization of the whole sample $M(T)$ as

$$B^{i,g}(t) = \mu_0\left[H(t) + D^{i,g}M(t)\right], \tag{IV.7}$$

which reduces to the Eqs. (IV.1) and (IV.5) with the intragranular effective demagnetizing factor D^g given by $D^g = 1 + D^i$.

According to the Eq. (IV.6), the harmonic voltage $v(t)$ detected by means of the AC susceptibility technique described in the Chapter II (see the Eq. (II.8)), in terms of the magnetizations of the inter- and intragranular volume fractions is given by

$$v(t) = -\frac{1}{\gamma}\frac{d}{dt}\left[M^i(t) + k_d n^g M^g(t)\right]. \quad \text{(IV.8)}$$

Here the inter- and intragranular magnetizations can be expressed in the form of the Eq. (II.4),

$$M^{i,g}(t) = \mathrm{Im}\left\{\sum_n \left(\chi^{i,g}{}_n{}' - i\chi^{i,g}{}_n{}''\right)\left[B^{i,g}(t)\right]^n\right\}, \quad \text{(IV.9)}$$

where we have introduced the inter- and intragranular nonlinear AC susceptibilities

$$\chi^{i,g} = \sum_n \chi^{i,g}{}_n = \sum_n \left(\chi^{i,g}{}_n{}' - i\chi^{i,g}{}_n{}''\right). \quad \text{(IV.10)}$$

Then, for $\gamma = -NSn\omega$ the Eq. (IV.8) reduces to

$$v(t) = \sum_n \left[M_n{}'(T)\cos(n\omega t) + M_n{}''(T)\sin(n\omega t)\right] = \mathrm{Im}\left\{\begin{matrix}\sum_n \left(\chi^i{}_n{}' - i\chi^i{}_n{}''\right)\left[B^i(t)\right]^n \\ +k_c n^g \sum_n \left(\chi^g{}_n{}' - i\chi^g{}_n{}''\right)[B^g(t)]^n\end{matrix}\right\}. \quad \text{(IV.11)}$$

IV.1.1.1 The effective demagnetizing factor k_d of grains

In order to exploit the effective demagnetizing factor k_d determining the demagnetizing field defined from the Eq. (IV.3) due to adjacent grains in the in the region between them, in the Fig. IV.2 we have assimilated individual grains to finite solenoids of width $\sim(a - \lambda^g)$ with $2a = 2b$ the dimensions of the grains in the plane perpendicular to external field and λ^g an effective penetration depth of the grains which has to be determined by correcting the critical state penetration depth[7-10]. In fact, these solenoids carry the shielding current of the grains $I^g = (2c)\, M^g(t)/\langle N_g\rangle$ with $2c$ the grains length and $\langle N_g\rangle$ an effective average number of turns.

It is easily to show that the magnetic field induction produced along the field direction z by one solenoid is given by

$$B_z(z,T) = \frac{\mu_0 I^g \langle N_g\rangle}{(2c)\lambda^g}\left[B_{z_1}(z) - B_{z_2}(z)\right] = \frac{1}{\lambda^g}\left[B_{z_1}(z) + B_{z_2}(z)\right], \quad \text{(IV.12)}$$

where

$$B_{z_1}(z) = \left(c + \frac{c}{2}\right) \ln \frac{a + \sqrt{a^2 + \left(c + \frac{c}{2}\right)^2}}{(a - \lambda^g) + \sqrt{(a - \lambda^g)^2 + (z + c)^2}}, \tag{IV.13a}$$

$$B_{z_2}(z) = \left(c - \frac{c}{2}\right) \ln \frac{a + \sqrt{a^2 + \left(c - \frac{c}{2}\right)^2}}{(a - \lambda^g) + \sqrt{(a - \lambda^g)^2 + \left(c - \frac{c}{2}\right)^2}}. \tag{IV.14b}$$

Then, the magnetic field induction acting in the region between adjacent grains at position $\boldsymbol{r}$ in the Fig. IV.1b can be taken as

$$k_d n^g M^g(t) = \frac{\mu_0 M^g}{\lambda^g} \left[B_{z_1}\left(\frac{c}{2}\right) + B_{z_2}\left(\frac{c}{2}\right) \right] - 4 d M^g, \tag{IV.15}$$

where the first term is the sum of the magnetic field inductions with form of the Eq. (IV.8) generated at position $\boldsymbol{r}$ of a slab by the first two neighbor grains along z contained in the up and down adjacent slabs, and the second term is the demagnetizing field due to the first four neighbor grains in the x-y plane of a slab with d the grain demagnetizing factor. The Eq. (IV.10) corresponds to an effective demagnetizing factor

$$k_d = \frac{\mu_0}{n^g \lambda^g} \left[B_{z_1}\left(\frac{c}{2}\right) + B_{z_2}\left(\frac{c}{2}\right) \right] - 4 d, \tag{IV.16}$$

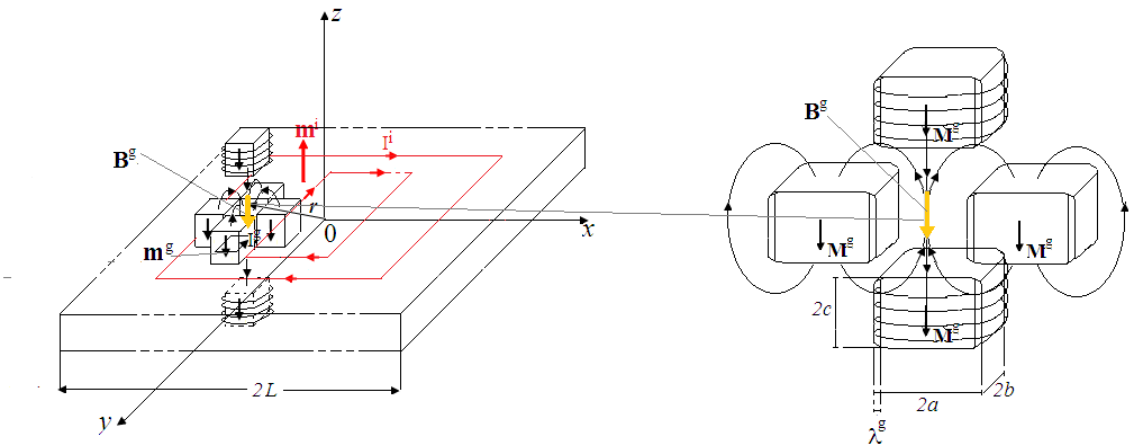

(a) (b)

Figure IV.2. Schematic diagram of (a) a slab of the sample containing a single layer of grains of the Fig. IV.1, and (b) the composition of the magnetic field induction coming from first two neighbor horizontal grains in the *x y* plane and the first two neighbor vertical grains contained in the up and down adjacent slabs at ***r***.

IV.2 Intermodulation Distortion (IMD) from demagnetizing fields

When considering the effects of demagnetizing fields produced from the in-phase and the out-of-phase components of the fundamental and higher harmonics of the sample magnetization, the effective fields acting on the sample's surface and on the grains's surfaces defined from the Eq. (IV.7) are given by

$$B^{i,g}(t) = \mu_0 \left[H_{ac} \sin(\omega t) + \sum_n D^{i,g} M_n^{'} \sin(n\omega t) + \sum_n D^{i,g} M_n^{''} \sin\left(\frac{\pi}{2} - n\omega t\right)\right]. \quad \text{(IV.17)}$$

In the following we will consider the effects of the demagnetizing fields arising from the first and third harmonics components $M_1^{'}$, $M_3^{'}$ and $M_1^{''}$, $M_3^{''}$ of the whole sample magnetization and of the inter- and intragranular first and third order nonlinear susceptibilities $\chi^{i,g}{}_1, \chi^{i,g}{}_3$. In this case, the contributions to the sample magnetization due to the inter- and intragranular fundamental susceptibilities $\chi^{i,g}{}_1$ are given by

$$\mathrm{Im}\left[\chi^{i,g}{}_1 B^{i,g}(t)\right] =$$

$$= \mathrm{Im}\left\{ \begin{array}{c} \left(\chi^{i,g^{'}}{}_1 - i\chi^{i,g^{''}}{}_1\right) \times \\ \mu_0 \left[H_{ac} \sin(\omega t) + \sum\limits_{n=1,3} D^{i,g} M_n^{'} \sin(n\omega t) + \sum\limits_{n=1,3} D^{i,g} M_n^{''} \sin\left(\frac{\pi}{2} - n\omega t\right)\right] \end{array} \right\} =$$

$$= M^{i,g^{'}}{}_{11} \sin(\omega t) + M^{i,g^{''}}{}_{11} \cos(\omega t) + M^{i,g^{'}}{}_{13} \sin(3\omega t) + M^{i,g^{''}}{}_{13} \cos(3\omega t), \quad \text{(IV.18)}$$

with

$$M^{i,g^{'}}{}_{11} = \mu_0 \left[H_{\mathrm{ac}} \chi^{i,g^{'}}{}_1 - D^{i,g} M^{'}{}_1 \chi^{i,g^{'}}{}_1 - D^{i,g} M^{''}{}_1 \chi^{i,g^{''}}{}_1 \right], \quad \text{(IV.19a)}$$

$$M^{i,g^{''}}{}_{11} = \mu_0 \left[-D^{i,g} \chi^{i,g^{'}}{}_1 M^{''}{}_1 + H_{\mathrm{ac}} \chi^{i,g^{''}}{}_1 - D^{i,g} M^{'}{}_1 \chi^{i,g^{''}}{}_1 \right], \quad \text{(IV. 19b)}$$

$$M^{i,g^{'}}{}_{13} = \mu_0 \left[-D^{i,g} M^{'}{}_3 \chi^{i,g^{'}}{}_1 - D^{i,g} M^{''}{}_3 \chi^{i,g^{''}}{}_1 \right], \quad \text{(IV. 19c)}$$

$$M^{i,g^{''}}{}_{13} = \mu_0 \left[-D^{i,g} \chi^{i,g^{'}}{}_1 M^{''}{}_3 - D^{i,g} M^{'}{}_3 \chi^{i,g^{''}}{}_1 \right]. \quad \text{(IV. 19d)}$$

For the 2-nd order nonlinear susceptibilities one obtains

$$\mathrm{Im}\left[\chi^{i,g}{}_2 B^{i,g}(t)^2\right] =$$

$$= \mathrm{Im}\left[\left\{ \begin{array}{c} \left(\chi^{i,g^{'}}{}_2 - i\chi^{i,g^{''}}{}_2\right) \times \\ \mu_0 \left[H_{ac} \sin(\omega t) + \sum\limits_{n=1,3} D^{i,g} M_n^{'} \sin(n\omega t) + \sum\limits_{n=1,3} D^{i,g} M_n^{''} \sin\left(\frac{\pi}{2} - n\omega t\right)\right] \end{array} \right\}^2 \right] =$$

$$= M^{i,g'}_{22}\sin(2\omega t) + M^{i,g''}_{22}\cos(2\omega t) + M^{i,g'}_{24}\sin(4\omega t) + M^{i,g''}_{24}\cos(4\omega t) + \\ + M^{i,g'}_{26}\sin(6\omega t) + M^{i,g''}_{26}\cos(6\omega t), \qquad \text{(IV.20)},$$

with

$$M^{i,g'}_{22} = {\mu_0}^2 {\chi^{i,g'}}_2 \left[{H_{ac}}^2 - 2D^{i,g} H_{\mathrm{ac}} {M'}_1 + {D^{i,g}}^2 {M'}_1 \quad + {D^{i,g}}^2 {M''}_1 \quad \right] + \\ {\mu_0}^2 {\chi^{i,g''}}_2 \left[-2{D^{i,g}}^2 {M'}_3 {M''}_1 - 2D^{i,g} H_{\mathrm{ac}} {M''}_3 + 2{D^{i,g}}^2 {M'}_1 {M''}_3 \right], \qquad \text{(IV.21a)}$$

$$M^{i,g''}_{22} = {\mu_0}^2 {\chi^{i,g'}}_2 \left[2{D^{i,g}}^2 {M'}_3 {M''}_1 - 2D^{i,g} H_{\mathrm{ac}} {M''}_3 + 2{D^{i,g}}^2 {M'}_1 {M''}_3 \right] \\ + {\mu_0}^2 {\chi^{i,g''}}_2 \left[H_{ac} - 2D^{i,g} H_{\mathrm{ac}} {M'}_1 + {D^{i,g}}^2 {M'}_1 \quad - {D^{i,g}}^2 {M''}_1 \quad \right], \qquad \text{(IV. 21b)}$$

$$M^{i,g'}_{24} = {\mu_0}^2 {\chi^{i,g'}}_2 \left[-2D^{i,g} H_{ac} {M'}_3 + 2{D^{i,g}}^2 {M'}_1 {M'}_3 + 2{D^{i,g}}^2 {M''}_1 {M''}_3 \right], \qquad \text{(IV. 21c)}$$

$$M^{i,g''}_{24} = {\mu_0}^2 {\chi^{i,g''}}_2 \left[-2D^{i,g} H_{ac} {M'}_3 + 2{D^{i,g}}^2 {M'}_1 {M'}_3 - 2{D^{i,g}}^2 {M''}_1 {M''}_3 \right], \qquad \text{(IV. 21d)}$$

$$M^{i,g'}_{26} = {\mu_0}^2 {\chi^{i,g'}}_2 \left[{D^{i,g}}^2 {M'}_3{}^2 + {D^{i,g}}^2 {M''}_3{}^2 \right], \qquad \text{(IV. 21e)}$$

$$M^{i,g''}_{26} = {\mu_0}^2 {\chi^{i,g''}}_2 \left[{D^{i,g}}^2 {M'}_3{}^2 - {D^{i,g}}^2 {M''}_3{}^2 \right], \qquad \text{(IV. 21f)}$$

and $M^{i,g'^{(\prime\prime)}}_{22} = M^{i,g'^{(\prime\prime)}}_{24} = M^{i,g'^{(\prime\prime)}}_{26} = 0$ since ${\chi^{i,g'}}_2 = {\chi^{i,g''}}_2 = 0$.

For the 3-rd order nonlinear susceptibilities one has

$$\mathrm{Im}\left[{\chi^{i,g}}_3 B^{i,g}(t)^3\right] = \\ = \mathrm{Im}\left[\begin{matrix} \left({\chi^{i,g'}}_3 - i{\chi^{i,g''}}_3\right) \times \\ \left\{ \mu_0 \left[H_{ac}\sin(\omega t) + \sum_{n=1,3} D^{i,g} M'_n \sin(n\omega t) + \sum_{n=1,3} D^{i,g} M''_n \sin\left(\frac{\pi}{2} - n\omega t\right) \right] \right\}^3 \end{matrix} \right]$$

$$= M^{i,g'}_{31}\sin(\omega t) + M^{i,g''}_{31}\cos(\omega t) + M^{i,g'}_{33}\sin(3\omega t) + M^{i,g''}_{33}\cos(3\omega t) + \\ + M^{i,g'}_{35}\sin(5\omega t) + M^{i,g''}_{35}\cos(5\omega t) + M^{i,g'}_{37}\sin(7\omega t) + M^{i,g''}_{37}\cos(7\omega t) + \\ M^{i,g'}_{39}\sin(9\omega t) + M^{i,g''}_{39}\cos(9\omega t), \qquad \text{(IV.22)},$$

with

$$M^{i,g'}_{31} = {\mu_0}^3 {\chi^{i,g'}}_3 \begin{bmatrix} 3{D^{i,g}}^2 H_{\mathrm{ac}} {M''}_1{}^2 - 3{D^{i,g}}^3 {M'}_1 {M''}_1{}^2 \\ +3{D^{i,g}}^3 {M'}_3 {M''}_1{}^2 - 6{D^{i,g}}^3 {M'}_3 {M''}_1 {M''}_3 \end{bmatrix} + \\ + {\mu_0}^3 {\chi^{i,g''}}_3 \begin{bmatrix} 3D^{i,g} H_{\mathrm{ac}} {M''}_1 - 6{D^{i,g}}^2 H_{\mathrm{ac}} {M'}_1 {M''}_1 + 3{D^{i,g}}^3 {M'}_1{}^2 {M''}_1 \\ -3D^{i,g} H_{\mathrm{ac}}{}^2 {M''}_3 + 6{D^{i,g}}^2 H_{\mathrm{ac}} {M'}_1 {M''}_3 - 3{D^{i,g}}^3 {M'}_1{}^2 {M''}_3 \\ -6{D^{i,g}}^2 H_{\mathrm{ac}} {M'}_3 {M''}_3 + 6{D^{i,g}}^3 {M'}_1 {M'}_3 {M''}_3 \end{bmatrix}, \qquad \text{(IV.23a)}$$

$$M^{i,g}{}''_{31} = \mu_0{}^3\chi^{i,g}{}'_3\begin{bmatrix} -3D^{i,g}H_{ac}{}^2M''_1 + 6D^{i,g}{}^2H_{ac}M'_1M''_1 - 3D^{i,g}{}^3M'_1{}^2M''_1 \\ -3D^{i,g}H_{ac}{}^2M''_3 + 6D^{i,g}{}^2H_{ac}M'_1M''_3 - 3D^{i,g}{}^3M'_1{}^2M''_3 \\ -3D^{i,g}{}^3M'_1{}^2M''_3 + 6D^{i,g}{}^2H_{ac}M'_3M''_3 - 6D^{i,g}{}^3M'_1M'_3M''_3 \end{bmatrix} +$$
$$+\mu_0{}^3\chi^{i,g}{}''_3\begin{bmatrix} -3D^{i,g}{}^2H_{ac}M''_1{}^2\chi''_3 + 3D^{i,g}{}^3M'_1M''_1{}^2\chi''_3 \\ +3D^{i,g}{}^3M'_3M''_1{}^2\chi''_3 + +6D^{i,g}{}^3M'_3M''_1M''_3\chi''_3 \end{bmatrix}, \quad \text{(IV.23b)}$$

$$M^{i,g}{}'_{33} = \mu_0{}^3\chi^{i,g}{}'_3\begin{bmatrix} H_{ac}^3 - 3D^{i,g}H_{ac}{}^2M'_1 + 3D^{i,g}{}^2H_{ac}M'_1{}^2 - D^{i,g}{}^3M'_1{}^3 \\ +6D^{i,g}{}^2H_{ac}M''_1M''_3 - 6D^{i,g}{}^3M'_1M''_1M''_3 - 3D^{i,g}{}^3M'_3M''_3{}^2 \end{bmatrix} +$$
$$+\mu_0{}^3\chi^{i,g}{}''_3\begin{bmatrix} -6D^{i,g}{}^2H_{ac}M'_3M''_1 + 6D^{i,g}{}^3M'_1M'_3M''_1 \\ +D^{i,g}{}^3M''_1{}^3 + 3D^{i,g}{}^3M'_1{}^2M''_3 \end{bmatrix}, \quad \text{(IV.23c)}$$

$$M^{i,g}{}''_{33} = \mu_0{}^3\chi^{i,g}{}'_3\begin{bmatrix} 6D^{i,g}{}^2H_{ac}M'_3M''_1 - 6D^{i,g}{}^3M'_1M'_3M''_1 \\ +D^{i,g}{}^3M''_1{}^3 - 3D^{i,g}{}^3M'_1{}^2M''_3 \end{bmatrix} +$$
$$+\mu_0{}^3\chi^{i,g}{}''_3\begin{bmatrix} H_{ac}{}^3 - 3D^{i,g}H_{ac}{}^2M'_1 + 3D^{i,g}{}^2H_{ac}M'_1{}^2 \\ -D^{i,g}{}^3M'_1{}^3 - 6D^{i,g}{}^2H_{ac}M''_1M''_3 \\ +6D^{i,g}{}^3M'_1M''_1M''_3 + 3D^{i,g}{}^3M'_3M''_3{}^2 \end{bmatrix}, \quad \text{(IV.23d)}$$

$$M^{i,g}{}'_{35} = \mu_0{}^3\chi^{i,g}{}'_3\begin{bmatrix} -3D^{i,g}H_{ac}{}^2M'_3 + 6D^{i,g}{}^2H_{ac}M'_1M'_3 - 3D^{i,g}{}^3M'_1{}^2M'_3 \\ +3D^{i,g}{}^2H_{ac}M''_3{}^2 - 3D^{i,g}{}^3M'_1M''_3{}^2 \end{bmatrix} +$$
$$\mu_0{}^3\chi^{i,g}{}''_3\left[3D^{i,g}{}^3M'_3{}^2M''_1 + 3D^{i,g}{}^3M''_1{}^2M''_3\right], \quad \text{(IV.23e)}$$

$$M^{i,g}{}''_{35} = \mu_0{}^3\chi^{i,g}{}'_3\left[-3D^{i,g}{}^3M'_3{}^2M''_1 + 3D^{i,g}{}^3M''_1{}^2M''_3\right] +$$
$$\mu_0{}^3\chi^{i,g}{}''_3\begin{bmatrix} -3D^{i,g}H_{ac}{}^2M'_3 + 6D^{i,g}{}^2H_{ac}M'_1M'_3 - 3D^{i,g}{}^3M'_1{}^2M'_3 \\ -3D^{i,g}{}^2H_{ac}M''_3{}^2 + 3D^{i,g}{}^3M'_1M''_3{}^2 \end{bmatrix}, \quad \text{(IV.23f)}$$

$$M^{i,g}{}'_{37} = \mu_0{}^3\chi^{i,g}{}'_3\left[3D^{i,g}{}^2H_{ac}M'_3{}^2 - 3D^{i,g}{}^3M'_1M'_3{}^2\right] + 3D^{i,g}{}^3\mu_0{}^3\chi^{i,g}{}''_3M''_1M''_3{}^2, \quad \text{(IV.23g)}$$

$$M^{i,g}{}''_{37} = 3D^{i,g}{}^3\mu_0{}^3\chi^{i,g}{}'_3M''_1M''_3{}^2 + \mu_0{}^3\chi^{i,g}{}''_3\left[3D^{i,g}{}^2H_{ac}M'_3{}^2 - 3D^{i,g}{}^3M'_1M'_3{}^2\right], \quad \text{(IV.23h)}$$

$$M^{i,g}{}'_{39} = -D^{i,g}{}^3\mu_0{}^3\chi^{i,g}{}'_3M'_3{}^2 + D^{i,g}{}^3\mu_0{}^3\chi^{i,g}{}''_3M''_3{}^2, \quad \text{(IV.23i)}$$

$$M^{i,g}{}''_{39} = D^{i,g}{}^3\mu_0{}^3\chi^{i,g}{}'_3M''_3{}^2 - D^{i,g}{}^3\mu_0{}^3\chi^{i,g}{}''_3M'_3{}^2. \quad \text{(IV.23l)}$$

By considering the Eqs. (IV.18), (IV.20) and (IV.22), the inter- and intragranular magnetizations can be written as

$$M(t) = \left[M^{i,g}{}'_{11} + M^{i,g}{}'_{31}\right]\sin(\omega t) + \left[M^{i,g}{}''_{11} + M^{i,g}{}''_{31}\right]\cos(\omega t) +$$
$$+\left[M^{i,g}{}'_{13} + M^{i,g}{}'_{33}\right]\sin(3\omega t) + \left[M^{i,g}{}''_{13} + M^{i,g}{}''_{33}\right]\cos(3\omega t) +$$

$$\left[M^{i,g}{}'_{35}\right]\sin(5\omega t) + M^{i,g}{}''_{35}\cos(5\omega t) + M^{i,g}{}'_{37}\sin(7\omega t) + M^{i,g}{}''_{37}\cos(7\omega t) + M^{i,g}{}'_{39}\sin(9\omega t) + M^{i,g}{}''_{39}\cos(9\omega t). \quad \text{(IV.24)}$$

The Eq. (IV.24) indicates that demagnetizing fields from the first and third harmonics of the inter- and intragranular magnetic responses produce not only harmonics with frequencies ω and 3ω, but also additional harmonics with frequencies 5ω, 7ω and 9ω. which are the result of the so called intermodulation distortion (IMD) phenomenon of the input demagnetizing fields. In general, these additional harmonics have to be taken into account in the analysis of the AC magnetic response.

By generalizing the Eq. (IV.24) to the case of first $N/2$ (N even) odd magnetization harmonics as the response to the applied field and to the demagnetizing fields arising from the first $(N-M)/2$ (M even) odd magnetization harmonics, one obtains

$$M(t) = \sum_{n=1,3,\ldots,N-1}\left[M^{i}{}'_{n} + k_d n^g M^{g}{}'_{n}\right]\sin(n\omega t) + \left[M^{i}{}''_{n} + k_d n^g M^{g}{}''_{n}\right]\cos(n\omega t)\ , \quad \text{(IV.25)}$$

where the $M^{i,g}{}'_{n}(T)$ and $M^{i,g}{}''_{n}(T)$ are the in-phase and out-of-phase components, respectively, of the inter- and intragranular magnetizations with respect to the external applied AC field, i.e.

$$M_n^{i,g}{}' = \frac{1}{\pi}\int_0^{2\pi} M^i(t)\sin(n\omega t)\ d\omega t, \quad \text{(IV.26a)}$$

$$M_n^{i,g}{}'' = \frac{1}{\pi}\int_0^{2\pi} M^g(t)\cos(n\omega t)\ d\omega t, \quad \text{(IV.26b)}$$

and

$$M^{i,g}(t) = \mathrm{Im}\left\{\sum_{n=1,,3,\ldots,N-1}\mu_0\chi_n^{i,g}\left(\begin{matrix}H_{ac}\,e^{i\omega t} + \\ D^{i,g}\sum_{m=1,3,\ldots,N-1-M}\left[\begin{matrix}M'_m e^{im\omega t} + \\ iM''_m e^{-im\omega t}\end{matrix}\right]\end{matrix}\right)^n\right\}. \quad \text{(IV.27)}$$

IV.3 Separation of the inter- and intragranular AC susceptibilities: the "magnetization-field (M-H)" equations

By equating like terms in both sides of the Eq. (IV.25) yields

$$M'_n = \left[M_n^{i}{}'(T) + k_d n^g M_n^{g}{}'(T)\right],\ n = 1,3,\ldots,N-1-M, \quad \text{(IV.28a)}$$

$$M'_n = \Delta M'_n + \left[M_n^{i}{}'(T) + k_d n^g M_n^{g}{}'(T)\right],\ n = N-M+1, N-M+2,\ldots,N-1, \quad \text{(IV.28b)}$$

$$M_n^{''} = \left[M_n^{i\,''}(T) + k_d n^g M_n^{g\,''}(T)\right], n = 1,3,\dots,N-1-M, \quad \text{(IV.28c)}$$

$$M_n^{'} = \Delta M_n^{''} + \left[M_n^{i\,''}(T) + k_d n^g M_n^{g\,''}(T)\right], n = N-M+1, N-M+2,\dots,N-1, \quad \text{(IV.28d)}$$

where we have included the additional contributions to the magnetization harmonics $\Delta M_n^{'}(T)$ and $\Delta M_n^{''}(T)$ for $n = 5,7,9$ due to the intermodulation of the input fields.

Since the coefficients $M_n^{i,g\,'}(T)$ and $M_n^{i,g\,''}(T)$, defined from the Eqs. (IV.26a)-(IV.26b) and (IV.27), are function of the effective magnetic field inductions acting on the sample's and grains's surfaces, the Eqs. (IV.28a)-(IV.28d) achieve a system of field-magnetization equations which are N linear equations for the set of variables given by the $2(N-M)$ susceptibilities harmonics parts $\chi^{i,g\,'}{}_1, \chi^{i,g\,'}{}_3, \dots, \chi^{i,g\,'}{}_{N-1-M}$ and $\chi^{i,g\,''}{}_1, \chi^{i,g\,''}{}_3, \dots, \chi^{i,g\,''}{}_{N-1-M}$, and the M magnetization harmonics components $\Delta M_{N-M+1}^{'}, \Delta M_{N-M+2}^{'}, \dots, \Delta M_{N-1}^{'}$ and $\Delta M_{N-M+1}^{''}, \Delta M_{N-M+2}^{''}, \dots., \Delta M_{N-1}^{''}$.

Then, starting from these measured magnetization harmonics components $M_n^{'}$ and $M_n^{''}$, the harmonics of the inter- and intragranular nonlinear susceptibilities and the additional contributions to the magnetization harmonics due to the intermodulation of the input fields can be determined by solving the system of equations (IV.28a)-(IV.28d) if additional $N-M$ equations are considered. In fact, these additional $N-M$ equations can be given by the theoretical expressions of the components of the susceptibilities first harmonic parts $\chi^{i,g\,'}{}_1$ and $\chi^{i,g\,''}{}_1$, for different flux dynamical regimes governing the penetration of magnetic flux inside the individual grains and the intergranular links. These expressions have been discussed in the chapter II for the main models describing the AC magnetic susceptibility of superconducting sample. In particular, the most general relaxational model can be considered which depends on the characteristic flux relaxation time τ and several dynamical and statistical parameters[11-16]. In fact, for the two processes of flux relaxation inside the intergranular contacts and the individual grains, respectively, the real and imaginary parts of the AC susceptibility first harmonics are given by

$$\chi^{i,g\,'}{}_1 = \mathrm{Im}\left\{-1 + \frac{1}{\left[1+\left(i\omega\tau^{i,g}\right)^{\alpha^{i,g}}\right]^{\beta^{i,g}}}\right\}, \quad \text{(IV.29a)}$$

$$\chi^{i,g\,''}{}_1 = \mathrm{Re}\left\{\frac{1}{\left[1+\left(i\omega\tau_{\tau^{i,g}}\right)^{\alpha^{i,g}}\right]^{\beta^{i,g}}}\right\}, \quad \text{(IV.29b)}$$

where τ^{i} and τ^{g} are the inter- and intragranular characteristic relaxation times, with $\alpha^{i,g}$ and $\beta^{i,g}$ (both varying in the range [0,1]) describing the distribution of the times $\tau_{i,g}$ around their spatial average values (nonlocality) and the asymmetry of the frequency spectrum as a nonlinear effect (nonlinearity), respectively. From the Eq. (IV.29b) the imaginary parts of fundamental susceptibilities have a maximum at a given frequency ν for $\alpha^{i,g}$ and $\beta^{i,g}$ given by

$$\tau^{i,g} = \left[\frac{\sin\left(\frac{\pi\alpha^{i,g}}{2\left(\beta^{i,g}+1\right)}\right)}{\sin\left(\frac{\pi\alpha^{i,g}\beta^{i,g}}{2\left(\beta^{i,g}+1\right)}\right)}\right]^{\frac{1}{\alpha^{i,g}}} (2\pi\nu)^{-1}. \qquad \text{(IV.30)}$$

As an example, we consider the case $N = 10$, that is the case of the magnetic response containing the first $N/2 = 5$ odd in-phase harmonics $M_1^{'}$, $M_3^{'}$, $M_5^{'}$, $M_7^{'}$, $M_9^{'}$ and out-of-phase harmonics $M_1^{''}$, $M_3^{''}$, $M_5^{''}$, $M_7^{''}$, $M_9^{''}$, as the response to the applied field and the demagnetizing fields arising from the first $(N-M)/2 = 2$ $(M = 6)$ magnetization harmonics components $M_1^{'}$, $M_3^{'}$ and $M_1^{''}$, $M_3^{''}$ governed by the nonlinear susceptibilities harmonics parts ${\chi^{i,g}}'_1, {\chi^{i,g}}'_3$ and ${\chi^{i,g}}''_1, {\chi^{i,g}}''_3$. In this case, the Eqs. (IV.28a)-(IV.28d) reduce to

$$M_n^{'} = \left[{M^{i}}'_n + k_d n^g {M^{g}}'_n\right], n = 1,3, \qquad \text{(IV.31a)}$$

$$M_n^{'} = \left[\Delta M_n^{'} + {M^{i}}'_n + k_d n^g {M^{g}}'_n\right], \quad n = 5,7,9, \qquad \text{(IV.31b)}$$

$$M_n^{''} = {M^{i}}''_n + k_d n^g {M^{g}}''_n, n = 1,3, \qquad \text{(IV.31c)}$$

$$M_n^{''} = \left[\Delta M_n^{''} + {M^{i}}''_n + k_d n^g {M^{g}}''_n\right], n = 5,7,9, \qquad \text{(IV.31d)}$$

with the coefficients ${M^{i,g}}'_n$ and ${M^{i,g}}''_n$ given by the Eqs. (IV.26a)-(IV.26b) and (IV.27) in terms of the variables ${\chi^{i}}'_1, {\chi^{i}}'_3, {\chi^{i}}''_1, {\chi^{i}}''_3$, and ${\chi^{g}}'_1, {\chi^{g}}'_3, {\chi^{g}}''_1, {\chi^{g}}''_3$, and $\Delta M_5^{'}, \Delta M_7^{'}, \Delta M_9^{'}, \Delta M_5^{''}, \Delta M_7^{''}, \Delta M_9^{''}$. The solution of the system of equations (IV.31a)-(IV.31d), together with the Eqs. (IV.29a) and (IV.29b) for ${\chi^{i,g}}'_1$ and ${\chi^{i,g}}'_1$, allows one to determine the intrinsic inter- and intragranular AC susceptibilities harmonics taking into account the demagnetizing effects.

IV.3.1 Quasi-linear approximation of the magnetization-field equations

In general, the intermodulation distortion increases with the amplitude of the exciting effective fields and it eventually swamps the magnetic response. For sufficiently low amplitudes of the field one can neglect the effect of the intermodulation distortion with respect to the intrinsic magnetic response in the measured signal. In fact, this corresponds to neglect the mixed terms in the n-th power of the effective field in right-side of the Eq. (IV.27), which reduces to

$$M^i(t) = \mathrm{Im}\left\{\sum_{n=1,,3,\ldots,,N-1} \mu_0 \chi_n^i \left(\begin{array}{c} (H_{ac}\, e^{i\omega t})^n + \\ \sum_{m=1,3,\ldots,N-1-M} \left[\begin{array}{c} (D^i M_m^{'} e^{im\omega t})^n + \\ (iD^i M_m^{''} e^{im\omega t})^n \end{array} \right] \end{array} \right) \right\}, \quad \text{(IV.32a)}$$

$$M^g(t) = \mathrm{Im}\left\{\sum_{n=1,,3,\ldots,,N-1} \mu_0 \chi_n^g \left(\begin{array}{c} (H_{ac}\, e^{i\omega t})^n + \\ \sum_{m=1,3,\ldots,N-1-M} \left[\begin{array}{c} (D^g M_m^{'} e^{im\omega t})^n \\ +(iD^g M_m^{''} e^{im\omega t})^n \end{array} \right] \end{array} \right) \right\}. \quad \text{(IV.32b)}$$

By inserting the Eqs. (IV.32a) and (IV.32b) into the Eqs. (IV.26a) and (IV.26b) one can calculate the coefficients ${M^{i,g}}_n^{'}$ and ${M^{i,g}}_n^{''}$ which enter the Eqs. (IV.28a)-(IV.28d).

The Eqs. (IV.32a) and (IV.32b) correspond to consider the inter- and intragranular magnetization as additions of nonlinear magnetic responses to effective magnetic fields given by the sum of the applied field and the demagnetizing fields arising from the in-phase and out-of-phase sample magnetization acting on the sample's and grains's surfaces, respectively. Since the superposition principle results partially applied, we refer to this situation as the "quasi-linear" approximation of the general calculation of the inter- and intragranular AC susceptibilities.

Bibliography

[1] F. Gomory, Supercond. Sci. Technol., 10 (1997) 523 and references therein.

[2] T. Ishida and H. Mazaki, Phys. Rev. B, 20 (197) 131.

[3] H. Kupfer, I. Apfelstedt, W. Schauer, T. Wolf and H. W¨uhl, Physica C, 153–155 (1988) 367.

[4] K. H. Muller, Physica C, 168 (1990) 585.

[5] R. I. Joseph and E. Schlömann, J. Appl. Phys., 36 (1965) 1579.

[6] J. Mrachkov and M. Kirov, Rev. Sci. Instrum., 62 (1991) 2469.

[7] D. X. Chen, C. Navau, N. Del Valle, A. Sanchez, Appl. Phys. Lett., 92 (2008) 202503.

[8] D. X. Chen, C. Navau, N. Del Valle, A. Sanchez, Physica C, 470 (2010) 89.

[9] J. Pearl, Appl. Phys. Lett., 5 (1964) 65.

[10] D.X. Chen, C. Navau, N. Del Valle, A. Sanchez, Supercond. Sci. Technol., 21 (2008) 105010.

[11] R. Kubo, M. Toda and N. Hashitsume, Statistical PhysicsII: Nonequilibrium Statistical Mechanics (Berlin: Springer, 1991) pp 120–5.

[12] S. Havriliak and S. Negami, J. Polym. Sci., C (1966) 14 99.

[13] G. Prando *et al*., J. Phys.: Condens. Matter, 25 (2013) 505701.

[14] G. Prando, P. Carretta, R. De Renzi, S. Sanna , A. Palenzona, M. Putti and M. Tropeano, Phys. Rev. B, 83 (2011) 174514.

[15] G. Prando, P. Carretta, R. De Renzi, S. Sanna , H. J. Grafe, S.Wurmehl and B. Büchner, Phys. Rev. B, 85 (2012) 144522.

[16] D. Mancusi, M. Polichetti, M. R. Cimberle and S. Pace, Supercond. Sci. Technol. 28 (2015) 095017.

Chapter V

Analysis of the temperature dependent AC magnetic response of the $FeSe_{0.5}Te_{0.5}$ granular sample

In order to probe the method described in the previous chapter for the interpretation of the AC magnetic response of a superconducting granular system, the AC magnetization first and higher harmonics relative to a $FeSe_{0.5}Te_{0.5}$ granular sample acquired by means of the AC susceptibility technique have been analyzed[1]. In fact, Fe-based superconductors are very suitable for the investigation of the effects of the flux dynamical regimes in the AC magnetic response since, due to a high degree of quenched disorder which corresponds to a high density of pinning sites, the relaxation of magnetic flux is strongly affected by thermally activated depinning of vortices[2-4]. The existence of leading thermally activated mechanisms of flux motion produces a frequency dependence of the AC magnetic response of these materials, which can be powerfully investigated by means of the AC measurements[13-157]. Moreover, from an applicative point of view, these superconducting compounds are very interesting especially since their properties induce large thermal fluctuations and depressed grain boundary superconductivity and they exhibit several characteristics similar to cuprate high-Tc superconductors being very useful also for understanding the superconductivity mechanism and flux penetration inside cuprate compounds.

FeX superconducting compounds, with X = As, P, S, Se, o Te, belong to the so-called 11 family for the 1:1 ratio of the two elements. In particular, the Tellurium in the FeSe base compound has been found to improve the superconductivity. In fact, T_c of $FeSe_{1-x}Te_x$ was found to be 14-20 K[1,5-12]. In this chapter we will analyze the temperature dependent AC magnetic response of a $FeSe_{0.5}Te_{0.5}$ granular sample in form of a slab acquired by using the AC insert of a 9 T Quantum Design PPMS. The sample was prepared by a multi-step process necessary to obtain dense polycrystals[6]. A preliminary magnetic characterization was also performed by means of hysteresis loops and temperature dependent magnetization measurements in DC field[1]. Then, the AC magnetic response fundamental and higher harmonics of the sample were measured by applying magnetic fields parallel to the sample's broader surface, at different AC field frequencies (ν = 107, 1077, 5385, 9693 Hz) and amplitudes ($\mu_0 H_{ac} = 0.05, 0.1, 0.2, 0.4, 0.8, 1.2$ mT), both in absence and in presence of a DC field ($\mu_0 H_{dc} = 1,3,5,7,9$ T).

The results of AC measurements will be first analyzed by using the method described in

the Chapter III. In fact, when the inter- and intragranular contributions to the temperature dependent magnetic response of a granular system are distinguishable, the method of analysis of the magnetic response of a homogeneous sample is typically used to interpret the two magnetic contributions. However, this kind of approach is not valid in presence magnetic interaction between the inter- and intragranular magnetic responses due to not negligible demagnetizing effects which produce effective magnetic fields acting on the sample's and grains's surfaces different from the applied one.

Then, in second part of this chapter, the AC magnetic response of the $FeSe_{0.5}Te_{0.5}$ granular sample will be analyzed by using the method of analysis introduced in the previous chapter, which takes into account the existence of demagnetizing effects and allows one to determine the intrinsic AC susceptibility of the intergranular links and of the grains in the whole range of measuring temperature, in order to extract the superconducting parameters and flux regimes governing the AC response as function of the external field parameters for the inter- and intragranular volume fractions.

V.1 Preliminary DC characterization of the $FeSe_{0.5}Te_{0.5}$ granular sample

The DC magnetic characterization of the investigated $FeSe_{0.5}Te_{0.5}$ sample has been preliminarily performed in order to extract some information which can be useful for the analysis of the AC magnetic response of the sample. The DC magnetic characterization has been made by means of the same measurements system used for AC susceptibility acquisition and described in the Chapter II. In fact, by moving the sample relative to the pick-up coil in a constant DC field parallel to the sample's broader surface, the temperature and field-dependent DC magnetization of the sample can be detected by the voltage induced in the pick-up coil due to the moving sample's magnetic moment.

Temperature dependent magnetization measurements were firstly performed in the zero-field cooling (ZFC) mode, with a magnetic DC field H_{dc} applied parallel to the sample surface. In fact, this curve, reported in the Fig. V.1a for $\mu_0 H_{dc} = 10$ mT, shows the characteristic behaviour of a superconducting sample with a transition from the diamagnetic state to the normal state with increasing temperature. The superconducting transition temperature $T_c \approx 14$ K was estimated as the temperature of the onset of the superconducting transition. This value of T_c is in full agreement with those obtained by electrical resistivity measurements on polycrystalline samples and resistivity, magnetic susceptibility and heat-capacity measurements on single crystals of the same batch compound[6]. Moreover, the demagnetizing factor of the whole sample geometry has

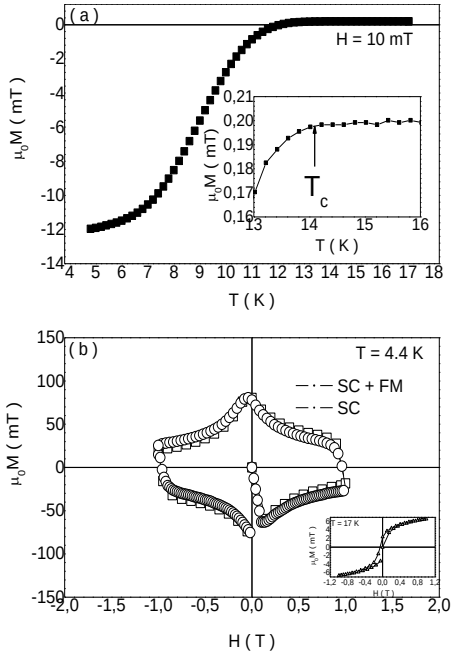

Figure V.1 (a) Experimental curves of the temperature dependent DC magnetization of the $FeSe_{0.5}Te_{05.}$ sample measured in the zero-field cooling (ZFC) mode, and in parallel field, with the inset showing an enlargement of the superconducting transition and T_c~14 K. (b) Experimental curves of the magnetic hysteresis loop in parallel field at $T < T_c$, (□) due to the superconducting and ferromagnetic phase, and (○) to the superconducting phase only[1]. The inset shows the magnetic loop measured above T_c.

been estimated from the low temperature magnetization value. In fact, an excess of ≈ 2 mT has been measured in the magnetic response at the lowest measured temperature $T = 5$ K, corresponding to a demagnetizing factor $D \approx 0.2$ according to the Eq. (II.29). This value of the demagnetizing factor results slightly smaller than the value reported in literature as calculated for the sample's geometry[16,17]. This can be ascribed to the not-fully completed diamagnetic transition at $T = 5$ K.

The DC characterization of the $FeSe_{0.5}Te_{0.5}$ sample was completed by measuring the magnetic hysteresis loops with the field applied parallel to the broader sample surface, at $T < T_c$ and $T > T_c$, reported in the Figure V.1b. This curve shows the superconducting hysteresis loop exhibiting the characteristic shape of a type II superconductor, with also a slight tilt suggesting the existence of a ferromagnetic phase along with the superconducting one as confirmed by the magnetic loop measured above T_c and reported in the inset of the Fig. V.1b. Then, the ferromagnetic contribution has been subtracted by the $M(H)$ curve measured below T_c in order to obtain the loop due to the superconducting phase only. From this loop, within the Bran critical state model, an estimation of the critical current density in the plane perpendicular to the magnetic applied field direction has been extracted as[18] $\mu_0 j_c \sim 20\Delta M(\mu_0 H_{dc})/t$, where t is the sample thickness and $\Delta M(H_{dc})$ is the difference between the volume magnetization in the upper

(demagnetization) and in the lower (magnetization) branches of the loop. The zero field value $\mu_0 j_c \sim 3 \times 10^3$ A/cm^2 obtained at $T = 4.4$ K is consistent with the values typically found in $FeSe_{0.5}Te_{0.5}$ polycrystals by using transport measurements and corresponding to the intergranular contribution[6].

V.2 Analysis of the temperature dependent AC magnetic response first harmonic

The curves of the temperature dependent AC magnetization real part $M'_1(T)$ and imaginary part $M''_1(T)$, measured on the $FeSe_{0.5}Te_{0.5}$ sample in absence of DC field, at a fixed AC field amplitude and different frequencies, are reported in the Fig. V.2a and V.2b, respectively. The corresponding curves measured at a fixed AC field amplitude and frequencies, with varying the DC field, are reported in the Figs. V.2c and V.2d.

Although the curves of $M'_1(T)$ show a single step diamagnetic transition, their temperature derivatives, not shown here, exhibit two maximums at the inter- and intragranular transitions. In the corresponding curves of $M''_1(T)$ two peaks appear which are associated with the maximum dissipation inside the sample, confirming the electromagnetic granularity of the sample. As described in the previous chapter, the peak at higher temperature and the peak at lower temperature in the $M''_1(T)$ curves can be associated to the maximum dissipation occurring when the magnetic flux reaches the center of the individual grains and of the intergranular links[19-22].

The curves of the Figs. V.2a and V.2c exhibit a dependence on the AC and DC field amplitude, with both the inter- and intragranular steps to the diamagnetic transition in the $M'_1(T)$ curve shifting towards lower temperatures and becoming broader with increasing the fields, as expected in the critical state models due to the effect of the magnetic field which tends to destroy the superconductivity[23-26]. However, this coincides with a shift towards lower temperatures and a raise of both peaks in the $M''_1(T)$ curves in the Figs. V.2b and V.2d, indicating that full penetration of the field inside both the sample and the individual grains can occur in correspondence to stronger pinning that is at lower temperatures. This suggests the existence of nonlinear flux dynamical regimes governing the AC responses in both the intergranular links and the individual grains. Moreover, although the curves of $M'_1(T)$ are not dependent on the AC field frequency as shown in the Fig. V.3a, the existence of a frequency dependence is more evident in the curves of $M''_1(T)$ in the Fig. V.3b where both peaks move to higher temperature and raise with increasing frequency suggesting the existence of creep phenomena In fact, the existence of flux creep phenomena are compatible with the above AC field [26,27].

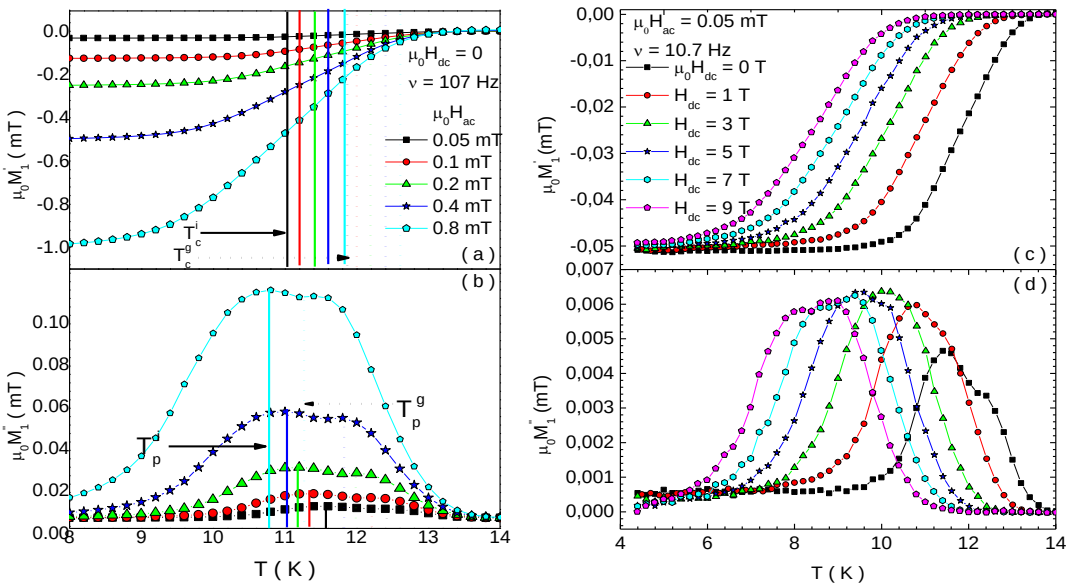

Figure V.2 Experimental curves of the $M'_1(T)$ and $M''_1(T)$ curves of the $FeSe_{0.5}Te_{0.5}$ sample: (a), (b) plots show the $\mu_0 H_{ac}$ dependence of $M'_1(T)$ and $M''_1(T)$, respectively, in absence of DC field and at a fixed AC frequency with the vertical line indicating (a) the critical temperature determined as the onset temperature of the transition in the $M'_1(T)$ curves and (b) the (soild) intergranular and (dashed) intragranular temperatures of the peaks in the $M''_1(T)$ curves; (c), (d) plots show the $M'_1(T)$ and $M''_1(T)$ curves at fixed AC field amplitude and frequency, and with varying the superimposed DC field, with the horizontal line indicating the transition to the normal state[1].

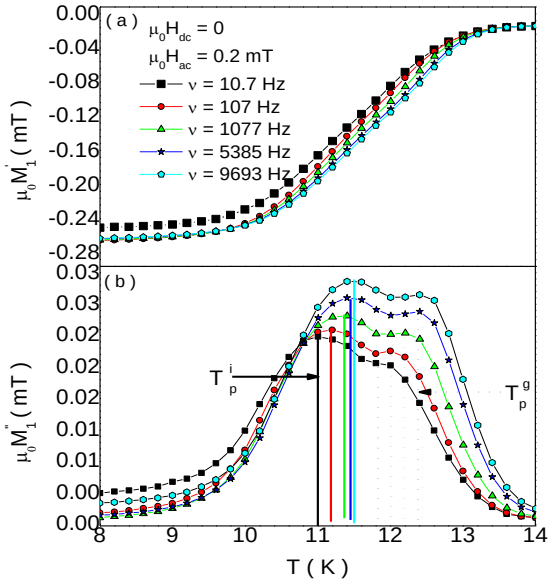

Figure V.3 Experimental curves of (a) $M'_1(T)$. and (b) $M''_1(T)$ of the $FeSe_{0.5}Te_{0.5}$ sample in absence of a DC field and at a fixed AC field amplitude, with varying the frequency[1].

V.2.1 Estimation of the superconducting critical temperatures $T_c^{i,g}$ and fields $H_c^{i,g}$

When cooling the sample the grains are expected to become superconducting first, while on cooling the sample further a change in the diminution rate of the sample magnetization is expected to occur when locking of the order parameter phases in different grains is reached[28]. Then, the inter- and intragranular critical temperatures T_c^i and T_c^g can be extracted from the onset and from the kink, respectively, of the temperature derivative of the $M_1'(T)$ curve.

These critical temperatures for the $FeSe_{0.5}Te_{0.5}$ sample have been obtained, with varying the AC field amplitude and the DC field, from the analysis of the $M_1'(T)$ curve in the Figs. V.2a and V.2b, respectively. This allowed us to determine the *T*-*H* critical lines for both the inter- and intragranular volume fractions of the sample, shown in the Figs. V.4a and V.4b. Both the $\mu_0 H_{ac}(T_c^{i,g})$ and $\mu_0 H_{ac}(T_c^{i,g})$ curves exhibit an upward curvature at lower temperature which cannot be described neither within the dirty one-gap superconductors WHH[29] model nor by power law expressions summarized in the Chapter I. In fact, an enhancement of the upper critical field at low temperature has been observed in Fe-based superconductors[6,12,30-33] and in the bismuth-oxysulfide layered compound $Bi_4O_4S_3$ analyzed in the Chapter III.

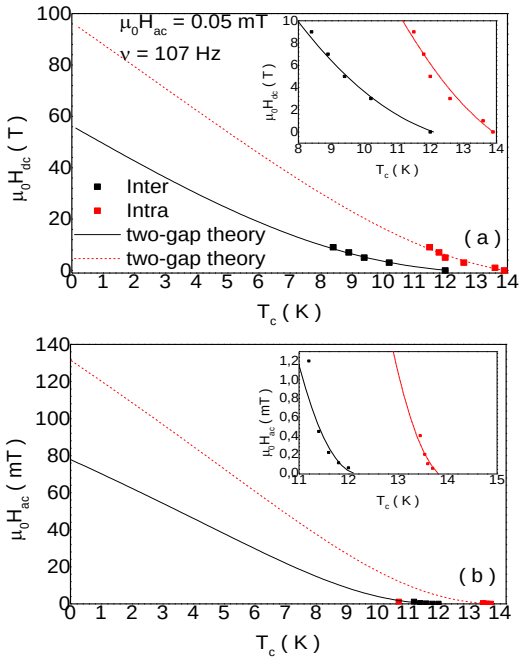

Figure V.4 Plot of the temperature dependence of the (black) inter- and (red) intragranular upper critical fields for the $FeSe_{0.5}Te_{05}$ sample, constructed by taking (a) the critical temperatures $T_c^{i,g}$ and the corresponding value of $\mu_0 H_{dc}$ from the curves in the Fig. V.3c and (b) the critical temperatures $T_c^{i,g}$ and the corresponding value of $\mu_0 H_{ac}$ from the curves in the Fig. V.3a. The lines indicate the fit of the data within the dirty two-gap theory. The inset show an enlargement at low temperature[1].

As for such systems, the curves of $\mu_0 H_{ac}(T_c^{i,g})$ and $\mu_0 H_{dc}(T_c^{i,g})$ for the $FeSe_{0.5}Te_{0.5}$ sample shown in the Fig. V.4 have been described within the theory of dirty two-gap superconductivity discussed in the Chapter II. In particular, we have found the diffusivity parameters $\eta^i \approx 10^{-5}$, $\lambda^i{}_{11} \approx 0.55$, $\lambda^i{}_{22} \approx 1$, $\lambda^i{}_{12} \approx 1$, $\lambda^i{}_{21} \approx 1.1$ and $\eta^g \approx 10^{-5}$, $\lambda^g{}_{11} \approx \lambda^g{}_{22} \approx 0.3$, $\lambda^g{}_{12} \approx \lambda^g{}_{21} \approx 0.8$. It is worth noting that in absence of DC field the $\mu_0 H_{ac}(T_c^{i,g})$ curves can be taken as effective AC field amplitudes determining the superconducting transition and so playing the role of effective upper critical fields[1].

V.2.2 Estimation of the superconducting critical current densities $j_c^{i,g}$

In first approximation the temperature dependence of the inter- and intragranular critical current densities $j_c^{i,g}$ of a granular sample can be obtained by taking the temperature $T_p^{i,g}$ of the corresponding dissipation peaks in the $M_1^{'}(T)$ curves measured at different AC field amplitudes, and the values of the field amplitude. In fact, the plots of $L\mu_0 j_c^i$ and $c\mu_0 j_c^g$ as function of the temperature $T_p^{i,g}$, with $2L$ the sample width and $2c$ the grains width, are reported in the Fig. V.5, as extracted from the plots of the Fig. V.4b. As expected, the critical current densities decrease with increasing temperature. In particular, the plots cannot be goodly described within the power laws discussed in the Chapter II and typically describing the temperature dependence of the critical current density for different pinning mechanisms in type II superconductors. On the other hand, as found for the $Bi_4O_4S_3$ sample analyzed in the Chapter III, an exponential decay law has been found to better describe the temperature dependence of $j_c^{i,g}$. It is worth underlining that, due to the effect of pinning, the value of $j_c^{i,g}$ at low temperatures is expected to tend to be lower

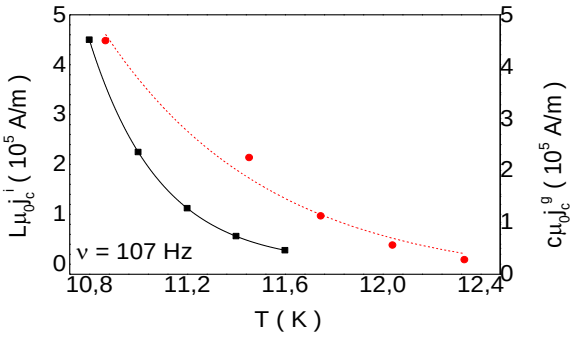

Figure V.5 Plot of the temperature dependence of (left scale) $L\mu_0 j_c^i$ and (right scale) $c\mu_0 j_c^g$ as function of the peak temperatures $T_p^{i,g}$ of the $FeSe_{0.5}Te_{05}$ sample, constructed from the curves of the Fig. V.2b by taking the peak temperature and the corresponding value of the AC field amplitude according with the Eq. (III.2). The lines are the fit of the data with an exponential decay.

than the prediction of the exponential decay. In particular, this trend is still valid at $T = 4.5$ K, since the value of the intergranular critical current density extrapolated at $T = 4.5$ K from the curves of $L\mu_0 j_c^i(T_p^i)$ in the Fig. V.5, $\mu_0 j_c^i(T) \approx 2 \times 10^7$ A/m^2, is in good agreement with the result obtained from the DC characterization of the $FeSe_{0.5}Te_{0.5}$ sample reported above.

V.2.3 Estimation of the vortex activation energies $U_a^{i,g}$

Since the field and frequency behaviours of the $M_1^{'}(T)$ and $M_1^{''}(T)$ of the $FeSe_{0.5}Te_{05}$ sample shown in the Figs. V.2 and V.3 suggest the existence of flux creep phenomena governing the AC magnetic response of both the individual grains and the intergranular contacts, the Arrhenius law discussed in the Chapter III is expected to be valid[34], i.e.

$$\nu = \nu_0^{i,g} e^{-\frac{U_a^{i,g}}{k_B T}}. \qquad \text{(V.1)}$$

where the activation energy $U_a^{i,g}$ depends on both temperature, and magnetic field and driving current, with $\nu_0^{i,g}$ a constant with dimensions of frequency.

As described in the Chapter III, the activation energies $U_a^{i,g}$ can be estimated from the analysis of the dissipation peaks in the $M_1^{''}(T)$ curves by assuming that these peaks occur when the relaxation times of the vortices inside the inter- and intragranular volume fractions match the inverse of the AC field frequency. In fact, according to the Eq. (V.1), the activation energies $U_a^{i,g}$ can be estimated from the slope of the Arrhenius plots of $\ln(\nu)$ as function of $1/T_p^{i,g}$ with T_p^i and T_p^g the temperatures of the inter- and intragranular peaks in the $M_1^{''}(T)$ curves measured at different frequencies. However, it is worth underlining that the hypothesis of resonance between the driving AC field and the microscopic oscillation of the vortices in the pinning wells requires very high measuring frequencies of the field and then it is not always valid.

The Arrhenius plots for the $FeSe_{0.5}Te_{05}$ sample in absence of DC field and at different AC field amplitudes are shown in the Figs. V.6a and V.6b for the inter- and intragranular volume fractions, respectively, as extracted from the curves of $M_1^{''}(T)$ measured with varying the AC frequency at a fixed AC field amplitude, for different values of the AC field amplitude. From these plots, the temperature and AC field amplitude dependences of the activation energies have been extracted by taking the intercepts and the slopes of the Arrhenius fit lines, respectively. The plots of $U_a^i(\mu_0 H_{ac})$ and $U_a^g(\mu_0 H_{ac})$ are reported in the Fig. V.7a. As expected, both the inter- and intragranular energies show a global

negative rate with increasing the AC field amplitude due to larger Lorentz force governing the vortex motion. However, an anomalous hump appear in the intermediate region of field amplitudes which will be discussed later after analyzing the electromagnetic granularity of the sample. Correspondingly, the plot of the intercepts of the Arrhenius plots at different AC field amplitudes as function of the slopes, shown in the Fig. V.7b, exhibit a possible linear trend. According to the Eq. (III.6), this linear dependence implies a linear temperature dependence of U_a with a law $U_a(T) \sim 1 - T/T_c$. y considering the Arrhenius plots at different AC fields, the dependence of U_a on $\mu_0 H_{ac}$ can be also extracted. The curves of $U_a(\mu_0 H_{ac})$ at different DC fields are reported in the Fig. III.8. The figure shows that U_a decreases with increasing $\mu_0 H_{ac}$ with a power law $U_a \sim (\mu_0 H_{ac})^{-\mu}$ and $\mu = 0.4$-0.6, expected in the collective flux creep of large flux bundles and in agreement with the previous results.

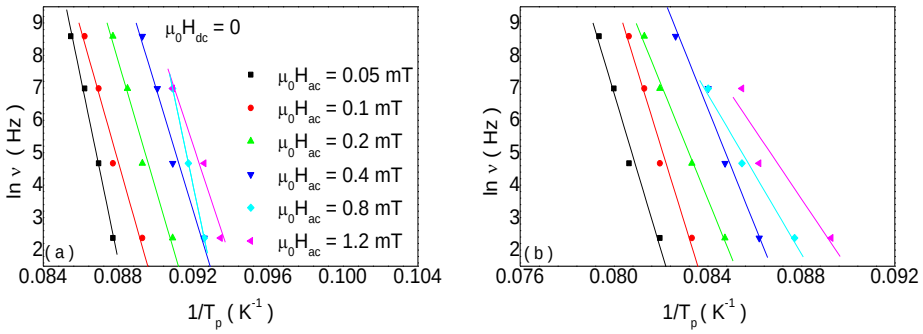

Figure V.6 The Arrhenius plots of the $FeSe_{0.5}Te_{05}$ sample ìn absence of DC field for (a) the inter- and (b) the intragranular volume fractions of the sample, constructed at different AC field amplitudes from the curves of $M_1''(T)$ measured with varying the AC frequency as in the Fig. V.3b, by taking the temperature of peaks and the corresponding value of the frequency according with the Eq. (V.1).

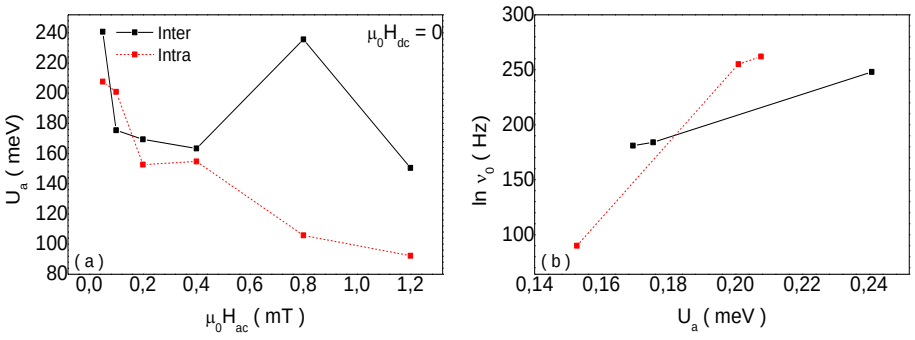

Figure V.7 (a) Plot of the activation energies as function of the AC field amplitude extracted as the slopes of the Arrhenius plots in the Figs. V.7a, for (black) the inter- and (red) the intragranular volume fractions. (b) Plot of the intercepts of the Arrhenius plots as function of the activation energies (slopes).

V.3 Analysis of the temperature dependent AC magnetic response third harmonic

The first higher harmonics until the 10-th order of the temperature dependent AC magnetization of the $FeSe_{0.5}Te_{05}$ granular sample have been measured. In particular, since the third harmonic is typically investigated among the higher harmonics of the AC magnetic response of superconducting samples due to its highest signal intensity, the following discussion will concentrate on the analysis of the AC magnetization third harmonic of the $FeSe_{0.5}Te_{05}$ sample in order to extract detailed information about the flux dynamics inside the sample. The curves of $M_3^{'}(T)$ and $M_3^{''}(T)$ for the $FeSe_{0.5}Te_{05}$ sample are reported in the Figs. V.8a and V.8b, respectively, measured in absence of DC field, at a fixed AC field frequency and with varying the AC field amplitude, and exhibit a dependence on H_{ac}. Moreover, nonzero values are present in the curves of $M_3^{'}(T)$ for $T < T_p(M_1^{''})$, contrarily to the Bean critical state prediction reported in the Fig. II.4 for a slab geometry[35], confirming the existence of flux dynamical regimes governing the AC magnetic response[36,37].

Due to the electromagnetic granularity of the sample observed in the analysis of the magnetic response first harmonic, two contributions are expected to combine in the $M_3^{'}(T)$ and $M_3^{''}(T)$ curves of the Figs. V.8a and V.8b. In fact, two large negative peaks are visible in the curves of $M_3^{'}(T)$ in proximity of the temperatures $T_p^{i,g}$ of the peaks in the corresponding $M_1^{'}(T)$ curves. These peaks shift towards lower temperatures and their height increases, while a small positive peak tend to appear at lower temperature, with increasing the AC field amplitude. On the other hand two negative peaks are visible in the curves of $M_3^{''}(T)$. Moreover, from the analysis of the $M_3^{'}(T)$ and $M_3^{''}(T)$curves measured in presence of a DC field $H_{dc} \gg H_{ac}$ and reported in the Fig. V.8c, the negative peak in the $M_3^{'}(T)$ curve at lower temperature tend to become lower than the negative peak at higher temperature and the near positive peak tends to raise with increasing the DC field. The field dependence of the curves of both $M_3^{'}(T)$ and $M_3^{''}(T)$indicates the existence of flux dynamical regimes governing the sample magnetic response, which are in particular nonlinear since give evidence also in presence of a DC field $H_{dc} \gg H_{ac}$ when the field is almost constant[38]. On the other hand, as found for the curves in absence of DC field, an evidence of critical state is present in the $M_3^{''}(T)$ curves of the Fig. V.8d that is the raising of a small positive peak near the onset temperature of $M_3^{'}(T)$[35].

Finally, we discuss the frequency dependence of the $M_3^{'}(T)$ and $M_3^{''}(T)$ curves measured in absence of DC field at a fixed AC field amplitude, and reported in the Figs. V.9a and V.9b, respectively. Here two negative peaks are visible both in the $M_3^{'}(T)$ curves at lower frequencies, whose height tends to increase with increasing frequency,

while the peak position is almost constant. However, a change in the frequency behavior is visible from the curves in the Figs. V.9a and V.9b at higher frequency. In fact, at frequency higher than $\nu = 1077$ Hz the height of the negative peaks in the $M_3^{'}(T)$ curves tend to decrease and the peaks become positive while tend towards higher temperatures with increasing frequency. A similar frequency behavior is exhibited by the $M_3^{''}(T)$ curves where, however, the peaks remain negative even at the highest frequency.

Although both the field and frequency behaviours of the curves of the temperature dependent sample magnetization third harmonic parts suggest the existence of nonlinear flux dynamical regimes governing the measured AC, due to the expected oscillating behavior of these curves and because of the electromagnetic granularity of the sample which produce temperature dependent effective magnetic fields on the sample's and grains's surfaces thus affecting the shape of the curves, it is not possible to identify inter- and intragranular contributions by using the procedure of comparison of the curves with the theoretical results discussed in the chapter II.

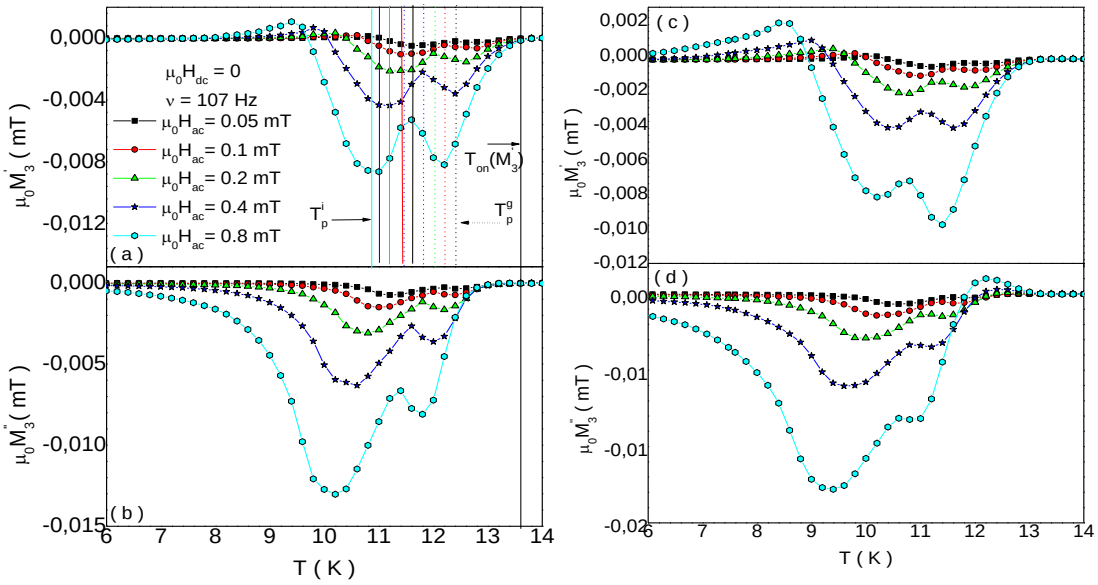

Fig. V.8 (Left) Plots of the experimental curves of (a) $M_3^{'}(T)$ and (b) $M_3^{''}(T)$ of the $FeSe_{0.5}Te_{05}$ sample measured in absence of DC field, at a fixed AC frequency with varying the AC amplitude, with the vertical lines indicating (a) the temperature of the (solid) intergranular and (dashed) intragranular peaks in the curves of $M_1^{''}(T)$ in the Figs. V.3b, and (b) the temperature of onset of the $M_3^{'}(T)$ curves. (Right) Plots of the experimental curves of (c) $M_3^{'}(T)$ and (d) $M_3^{''}(T)$ measured at fixed AC field amplitude and frequency, with varying a strong DC field.

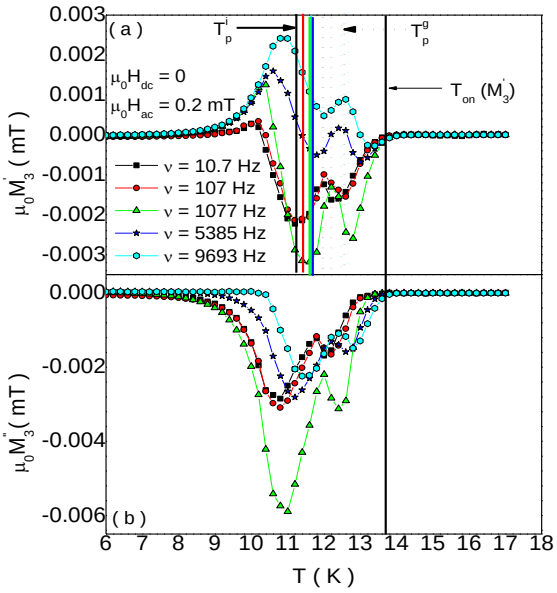

Fig. V.9 Plots of the experimental curves of (a) $M_3^{'}(T)$ and (b) $M_3^{''}(T)$, for the $FeSe_{0.5}Te_{05}$ sample, measured in absence of DC field, at a fixed AC amplitude with varying the AC frequency.

V.4 Influence of inter- and intragranular demagnetizing effects on the analysis of the AC magnetic response of the $FeSe_{0.5}Te_{05}$ granular sample

In the previous analysis of the magnetic response of the $FeSe_{0.5}Te_{05}$ granular sample, demagnetizing effects arising from the geometry of the whole sample and of the individual grains have not been considered. Then, several superconducting parameters and information about the flux dynamics have been extracted from the analysis of the inter- and intragranular contributions to the temperature dependent magnetization of the whole sample considered as the response to the applied AC and DC fields. However, due to the existence of demagnetizing fields coming from the whole sample and from the grains and to their magnetic interaction, the magnetic field induction acting on the sample's and grains's surfaces may be distorted with respect to the applied fields. Since this may produce the existence of temperature dependent effective fields governing the magnetic responses of the inter- and intragranular volume fractions of the material, respectively, the corresponding temperature dependent actual AC susceptibilities harmonics parts, obtained after dividing the whole sample magnetization harmonics to the temperature dependent effective fields amplitudes, may be considered. In fact, these could be very different from the AC susceptibilities harmonics parts obtained by dividing the whole sample magnetization harmonics to the constant applied fields amplitudes.

In the following the experimental curves of the magnetic response of the $FeSe_{0.5}Te_{05}$ granular sample will be analyzed taking into account the existence of demagnetizing effects in order to extract the actual superconducting parameters and flux dynamical information, and investigate as demagnetizing fields affect their evaluation. At this aim,

in the chapter IV we have developed a model for describing the total magnetization of a superconducting granular system acquired by means of the AC susceptibility technique in terms of the inter- and intragranular magnetic responses together with a numerical method, consisting in the solution of the system of Eqs. (IV.28a)-(IV.28b), for determining the actual inter-and intragranular AC susceptibilities.

V.4.1 Numerical demagnetizing correction of the sample AC magnetic response in absence of DC field

In the following analysis, we will consider the application of the method described in the Chapter IV for the case of the sample magnetic response containing the first $N/2 = 5$ odd in-phase harmonics $M_1^{'}$, $M_3^{'}$, $M_5^{'}$, $M_7^{'}$, $M_9^{'}$ and out-of-phase harmonics $M_1^{''}$, $M_3^{''}$, $M_5^{''}$, $M_7^{''}$, $M_9^{''}$, as the response to the applied AC field and the demagnetizing fields arising from the first $(N-M)/2 = 2$ $(M = 6)$ magnetization harmonics components $M_1^{'}$, $M_3^{'}$ and $M_1^{''}$, $M_3^{''}$, governed by the nonlinear susceptibilities harmonics parts $\chi^{i,g^{'}}{}_1, \chi^{i,g^{'}}{}_3$ and $\chi^{i,g^{''}}{}_1, \chi^{i,g^{''}}{}_3$. In this case, the Eqs. (IV.28a)-(IV.28d) reduce to the Eqs. (IV.31a)-(IV.31d), that are

$$M_n^{'}(T) = M^{i^{'}}{}_n(T) + k_d(T) n^g M^{g^{'}}{}_n(T),\ n = 1,3, \tag{V.2a}$$

$$M_n^{'}(T) = \Delta M_n^{'}(T) + M^{i^{'}}{}_n(T) + k_d(T) n^g M^{g^{'}}{}_n(T), \quad n = 5,7,9, \tag{V.2b}$$

$$M_n^{''}(T) = M^{i^{''}}{}_n(T) + k_d(T) n^g M^{g^{''}}{}_n(T),\ n = 1,3, \tag{V.2c}$$

$$M_n^{''}(T) = \Delta M_n^{''}(T) + M^{i^{''}}{}_n(T) + k_d(T) n^g M^{g^{''}}{}_n(T),\ n = 5,7,9, \tag{V.2d}$$

where we have considered the dependence on temperature. According to the Eqs. (IV.26a) and (IV.26b), the coefficients $M^{i,g^{'}}{}_n(T)$ and $M^{i,g^{''}}{}_n(T)$ are given by

$$M_n^{i,g^{'}}(T) = \frac{1}{\pi}\int_0^{2\pi} M^i(T,t)\sin(n\omega t)\ d\omega t, \tag{V.3a}$$

$$M_n^{i,g^{''}}(T) = \frac{1}{\pi}\int_0^{2\pi} M^g(T,t)\cos(n\omega t)\ d\omega t. \tag{V.3b}$$

with

$$M^{i,g}(T,t) = \mathrm{Im}\{\sum_{n=1,3} \mu_0 \chi_n^{i,g}(T) B^{i,g}(T,t)^n\}. \quad \text{(V.4)}$$

Here, according to the Eq. (IV.27) the effective fields are given by

$$B^{i,g}(T,t) = H_{ac}\, e^{i\omega t} + D^{i,g} \sum_{m=1,3} \left[M_m^{'}(T) e^{im\omega t} + i M_m^{''}(T) e^{-im\omega t} \right]. \quad \text{(V.5)}$$

where $D^i = -D$ and $D^g = 1 + D$ with D the demagnetizing factor of the whole sample geometry. Moreover, within the relaxational mode discussed in the Chapter IV, the expressions (IV.29a) and (IV.29b) can be used for the temperature dependent real and imaginary parts of the fundamental susceptibilities, respectively, i.e.[39-41]

$$\chi^{i,g}{}_1^{'}(\omega, T) = -1 + \frac{1}{\left\{1 + \left[i\omega\, \tau^{i,g}(T)\right]^{\alpha^{i,g}}\right\}^{\beta^{i,g}}}, \quad \text{(V.6a)}$$

$$\chi^{i,g}{}_1^{''}(\omega, T) = \frac{1}{\left\{1 + \left[i\omega\, \tau^{i,g}(T)\right]^{\alpha^{i,g}}\right\}^{\beta^{i,g}}}, \quad \text{(V.6b)}$$

where the temperature dependence is given by the temperature dependence of the inter- and intragranular flux relaxation times $\tau^i(T)$ and $\tau^g(T)$, respectively.

V.4.2Temperature dependence of the effective magnetic fields

From the Eq. (V.5) the temperature dependence of the amplitude of the in-phase and out-of-phase components of the effective magnetic fields first and third harmonics are given by

$$B_{ac}{}_1^{i,g^{'}}(T) = \mu_0 \left[H_{ac} + D^{i,g} M_1^{'}(T) \right], \qquad B_{ac}{}_1^{i,g^{''}}(T) = D^{i,g} M_1^{''}(T) \quad \text{(V.7a)}$$

$$B_{ac}{}_3^{i,g^{'}}(T) = D^{i,g} M_3^{'}(T), \qquad B_{ac}{}_3^{i,g^{''}}(T) = D^{i,g} M_3^{''}(T). \quad \text{(V.7b)}$$

These temperature dependences for the applied AC field amplitude $\mu_0 H_{ac} = 0.2$ mT and frequency $\nu = 107$ Hz are shown in the Figs. V.10a and V.10b, respectively, as calculated from the magnetization curves of the Figs. V.2a and V.8a. It is worth noting that the values of the in-phase field $B_{ac}{}_1^{i^{'}}(T)$ acting on the sample's surface (left scale in the Fig. V.10a) are larger than the AC field amplitude $\mu_0 H_{ac}$ at lower temperature and

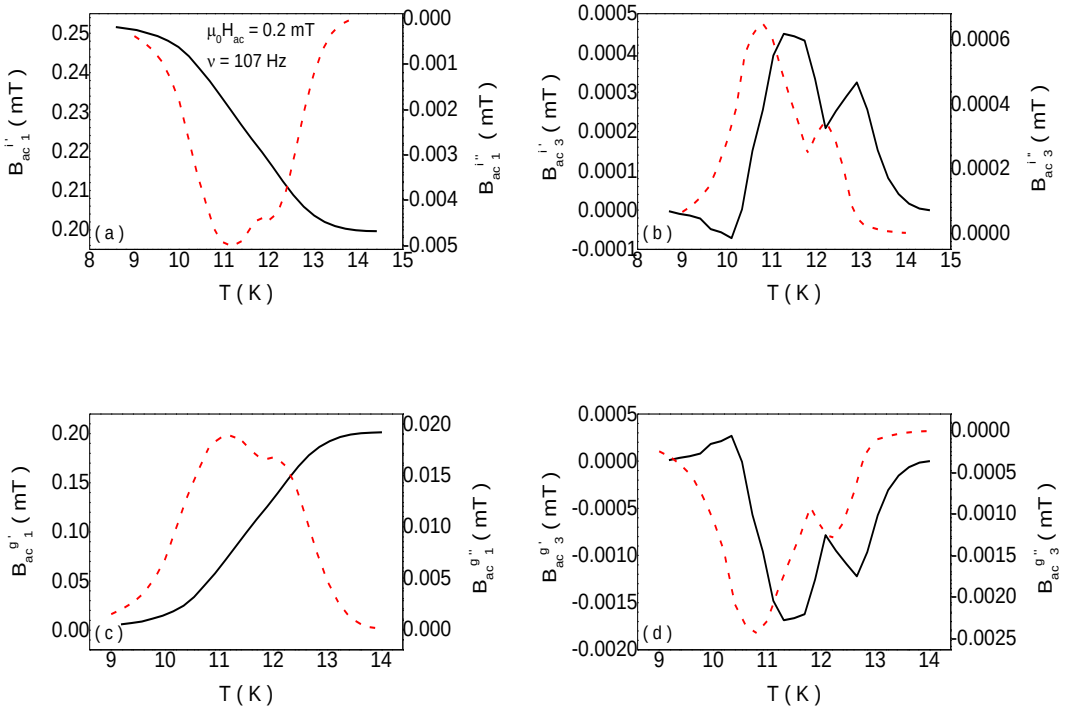

Figure V.10 Temperature dependence of the in-phase and out-of-phase effective magnetic fields first and third harmonics amplitudes, acting (a,b) on the sample's surface and (c,d) on the grains's surfaces; the curves have been calculated with the Eqs. (V.7) and by using the components of the first and third harmonic of the sample magnetization $M_1^{'}(T)$, $M_1^{''}(T)$ and $M_3^{'}(T)$, $M_3^{''}(T)$ reported in the Figs. V.2a and V.8a, respectively, for $\mu_0 H_{ac} = 0.2$ mT and $\nu = 107$ Hz. The left scale and the right scale are the in-phase and the out-of-phase components of the fields, respectively.

tend to $\mu_0 H_{ac}$ with increasing temperature due to the temperature dependence of the demagnetizing field arising from the whole sample in-phase magnetization $D^i M_1^{'}(T)$. However, the values of the field $B_{ac\,1}^{\;i\;'}(T)$ are much larger than the values of the out-of-phase field $B_{ac\,1}^{\;i\;''}(T)$ (right scale in the Fig. V.10a). Although the effect of this field on the in-phase component of the intergranular magnetization $M_1^{'}(T)$ can be neglected, one can be seen from the Eqs. (IV.19) and (IV.23) that it produces a not negligible contribution to the out-of-phase component of the magnetization first harmonic $M_1^{''}(T)$ and to both components of the magnetization third harmonic $M_3^{'}(T)$ and $M_3^{''}(T)$. These contributions add to the contributions due to the in-phase and out-of-phase third harmonic fields $B_{ac\,3}^{\;i\;'}(T)$ and $B_{ac\,3}^{\;i\;''}(T)$ shown in the Figs. V.10d.

On the other hand, the values of the in-phase field $B_{ac\,1}^{\;g\;'}(T)$ acting on the grains's surfaces (left scale in the Fig. V.2c) is zero at low temperature due to the shielding by the intergranular currents giving $D^g M_1^{'} = -\mu_0 H_{ac}$, and it increases towards $\mu_0 H_{ac}$ with increasing temperature towards the superconducting transition of the sample due to the

increase of $M_1^{'}(T)$. Unlike the intergranular case, the value of the out-of-phase field $B_{ac}{}_1^{g^{''}}(T)$ are not negligible with respect to the values of $B_{ac}{}_1^{g^{'}}(T)$ in the region of low temperature, where $B_{ac}{}_1^{g^{'}}(T) \approx 0$, thus producing not negligible effects on both the first and third harmonics of the sample magnetization.

V.4.2.1 Temperature dependence of the effective upper critical field

By taking the inter- and intragranular superconducting critical temperatures T_c^i and T_c^g estimated from the analysis of the whole sample magnetization first harmonic in the Fig. V.2a, and the values of the amplitudes of the effective fundamental AC magnetic fields in the Fig. V.10a and V.10c at the temperatures T_c^i and T_c^g, respectively, the curves $B_{ac}{}_1^{i^{'}}(T_c^i)$ and $B_{ac}{}_1^{g^{'}}(T_c^g)$ can be constructed, which play the role of the temperature dependent upper critical fields in absence of DC fields[1]. These curves at $\nu = 107$ Hz are reported in the Fig. V.11. As found for the DC H-T lines obtained without considering demagnetizing effects in the previous analysis, the curves of $B_{ac}{}_1^{i^{'}}(T_c^i)$ and $B_{ac}{}_1^{g^{'}}(T_c^g)$ have been best described within the dirty two-gap theory of superconductivity discussed in the Chapter I[29]. In particular, the intra- and interband coefficients have been taken $\lambda_{12} \approx 0.6$, $\lambda_{21} \approx 1$ and $\lambda_{11} = \lambda_{22} = 0$, and the ratio between the hole-band diffusivity and the in-plane electron-band diffusivity has been taken $\eta \approx 0.001$. These values are different from the values obtained without considering demagnetizing effects, while they are more consistent with the results reported in literature for the description of the upper critical fields of Fe-based superconductors especially for weak intraband coupling coefficient[42,43].

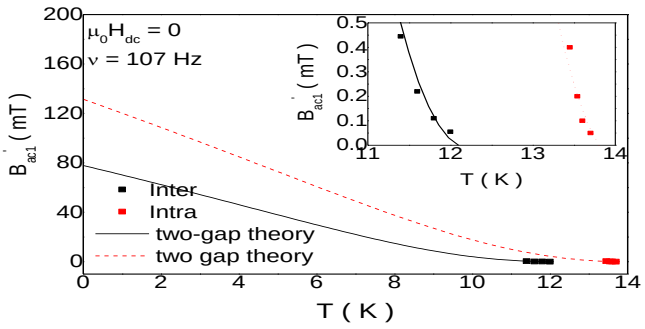

Figure V.11 Plots of the temperature dependence of the inter- and intragranular effective upper critical AC fields for the $FeSe_{0.5}Te_{05}$ sample in absence of DC fields constructed by taking the transition temperatures T_c^i and T_c^g from the curves of the Fig. V.2a and the values of the amplitude of the effective AC fields $B_{ac}{}_1^{i^{'}}(T_c^i)$ and $B_{ac}{}_1^{g^{'}}(T_c^g)$ from the Figs. V.10a and V.10c . The lines indicate the fit of the data with the dirty two-gap theory described in the Chapter I. The inset is an enlargement in the region of small field amplitudes[1].

V.4.3 Temperature dependence of the flux relaxation times $\tau^{i,g}$

The first and third harmonics components of the effective magnetic fields governing the inter- and intragranular magnetic responses can give different channels of flux relaxation inside the intergranular links and the individual grains, respectively. In this case, the first order and third order relaxation processes can be detected by means of the maximum dissipation peaks in the temperature dependent imaginary parts of the first and third harmonics of the sample magnetization, respectively. However, here we are interested to the characteristic times $\tau^{i,g}(T)$ of the first order process in order to calculate the corresponding AC susceptibility harmonics by means of the relaxational model expression (V.6a) and (V.6b).

According to the Eq. (IV.29), the plots of $\tau^{i}(T)$ and $\tau^{g}(T)$ can be constructed in the region of temperatures of the dissipation peaks in the experimental curves of $M_1^{''}(T)$ by taking the temperature of the peaks and the value of $\tau^{i,g} = f^{i,g}(\nu)$ with

$$f^{i,g}(\nu) = \left[\frac{\sin\left(\frac{\pi\alpha^{i,g}}{2\left(\beta^{i,g}+1\right)}\right)}{\sin\left(\frac{\pi\alpha^{i,g}\beta^{i,g}}{2\left(\beta^{i,g}+1\right)}\right)}\right]^{\frac{1}{\alpha^{i,g}}} (2\pi\nu)^{-1}, \tag{V.8}$$

where $\alpha^{i,g}$ and $\beta^{i,g}$ are parameters describing the distribution of the relaxation times around their spatial average value (nonlocality) and the asymmetry of the frequency spectrums as a nonlinear effect (nonlinearity), respectively, and can be taken in the interval[0,1][39-41]. Then, by taking the temperatures T_p^i and T_p^g of the peaks in the $M_1^{''}(T)$ curves measured at different frequencies ν and the values of $f^{i,g}(\nu)$ for each curve, a family of plots $\tau^{i}(T_p^i)$ and $\tau^{g}(T_p^g)$ can be constructed for different values of the parameters $\alpha^{i,g}$ and $\beta^{i,g}$, i.e.

$$\tau^{i,g}(T_p^{i,g}) = f^{i,g}(\nu)(2\pi\nu)^{-1}. \tag{V.9}$$

On the other hand, an universal law can be considered to describe the temperature dependence of the times in presence of regimes of thermally activated flux motion. In fact, according to the Eq. (III.6), one can take

$$\tau^{i,g}(T) = \tau_0^{i,g} e^{\frac{U_a^{i,g}}{k_B T}}, \tag{V.10}$$

where $\tau_0^{i,g}$ are the high temperature limit times, and $U_a^{i,g}$ are the activation energies depending on temperature, field and driving current due to the field. In absence of DC

field, the activation energy can be taken as

$$U_a^{i,g} = U_0^{i,g}\left(1-\frac{T}{T_c}\right)^{q^{i,g}}\left(1+p^{i,g}\frac{T}{T_c-T}\right)\left(j^{i,g}/j_c^{i,g}\right)^{-\mu^{i,g}}, \qquad \text{(V.11)}$$

with $U_0^{i,g}$ are the unperturbed pinning energy at zero temperature, and $q^{i,g}$, $p^{i,g}$ and $\mu^{i,g}$ characteristic exponents with describe the thermally activated flux flow (taff) and the flux creep(fc) regimes. In fact, for $q^{i,g} = 2 - n/2$, with $0 < n < 3$ depending on the dimensionality, and $p^{i,g} = 0$, $\mu^{i,g} \approx 0$ in the Eq. (V.11), the Eq. (V.10) gives the taff time

$$\tau_{taff}^{i,g}(T) = \tau_0^{i,g} e^{\frac{U_0^{i,g}\left(1-\frac{T}{T_c}\right)^{q^{i,g}}}{k_B T}}, \qquad \text{(V.12)}$$

where there is not dependence on the driving current .

On the other hand, for $q^{i,g} = p^{i,g} = 2 - n/2$ in the Eq. (V.10), the Eq. (V.11) gives the flux creep (fc) time

$$\tau_{fc}^{i,g}(T) = \tau_0^{i,g} e^{\frac{U_0^{i,g}\left(1-\frac{T}{T_c}\right)^{q^{i,g}}\left(1+q^{i,g}\frac{T}{T_c-T}\right)\left(j^{i,g}/j_c^{i,g}\right)^{-\mu^{i,g}}}{k_B T}}, \qquad \text{(V.13)}$$

Here the dependence on the current density $\left(j^{i,g}/j_c^{i,g}\right)^{-\mu^{i,g}}$ can be taken as $\left(j^{i,g}/j_c^{i,g}\right)^{-\mu^{i,g}} \sim \left[B_{ac}^{i,g}{}'_1(T)\right]^{-\mu^{i,g}}$ at $T = T_p^{i,g}$ within the Bean critical state model, since the maximums of the out-of-phase component of the $M_1''(T)$ curve are expected to occur when the field in the center of the sample and of the grains reaches the value of effective fields amplitude $B_{ac}^{i}{}'_1(T)$ and $B_{ac}^{g}{}'_1(T)_1$, respectively[19-21]. In particular, we expect that the out-of-phase components of the first harmonic and both components of the higher harmonics of the effective fields can be neglected for the calculation of the first order flux relaxation times.

A crossover to the flux creep regime to the taff regime is expected with increasing temperature, with a time

$$\tau_{ct}^{i,g}(T) = \tau_{fc}^{i,g}(T) + \theta(T - T_{ct}^{*})\tau_{taff}^{i,g}(T), \qquad \text{(V.14)}$$

where θ is a step-function and $T_{ct}^{*\,i,g}$ is a creep-taff (ct) crossover temperature. Moreover,

the existence of a flux flow regime in proximity of the superconducting transition can be also considered with a time

$$\tau_{ff}^{i,g}(T) = \tau_0^{i,g} \frac{B_{ac\,1}^{i,g'}(T)}{B_{c2}^{i,g}(T)}, \tag{V.15}$$

where, in absence of DC field, the temperature dependent upper critical fields $B_{c2}^{i}(T)$ and $B_{c2}^{g}(T)$ can be taken from the effective upper critical AC fields $B_{c2\,1}^{i\,'}(T)$ and $B_{c2}^{g}(T)_1^{'}$ reported in the Fig. V.11.

Finally, the existence of a regime of parallel between the flux creep channel and the flux flow channel (cf) of relaxation can be taken into account by means of a time

$$\tau_{cf}^{i,g}(T) = \tau_{cf}^{i,g}(T) + \theta\left(T - T_{cf}^{*}\right)\left[\tau_{fc}^{i,g}(T)^{-1} + \tau_{ff}^{i,g}(T)^{-1}\right]^{-1}, \tag{V.16}$$

with $T_{cf}^{*\,i,g}$ a creep-parallel crossover temperature.

By means of a numerical programmed algorithm, the best fits of the plots of $\tau^{i}(T_p^{i})$ and $\tau^{g}\left(T_p^{g}\right)$, given by the Eq. (V.9), to the universal theoretical expression of the temperature dependent relaxation times given by the Eqs. (V.12)-(V.16) have been obtained for each couple of values of the parameters $\alpha^{i,g}$ and $\beta^{i,g}$ in the range [0,1]. In fact, the criterion of minimization of the least squares has been used to determine the values of $\alpha^{i,g}$ and $\beta^{i,g}$ together with the values of dynamical parameters $q^{i,g}$ and $\tau_0^{i,g}$. On the other hand, the other parameters $U_0^{i,g}$, $\mu^{i,g}$ were preliminarily determined from the fit of the plot of the amplitudes of the in-phase components of the effective AC fields first harmonics $B_{ac\,1}^{i,g\,'}$ as function of the peak temperatures $T_p^{i,g}$ constructed by taking the $T_p^{i,g}$ in the $M_1^{''}(T)$ curves at different values of the AC field amplitude $\mu_0 H_{ac}$ in the Fig. V.2b and the values of the corresponding amplitudes of the effective AC field $B_{ac\,1}^{i,g\,'}$ at $T_p^{i,g}$ in the Figs. V.10a and V.10c. In fact, by inverting the flux creep temperature dependence of the time of the Eq. (V.13), yields

$$B_{ac\,1}^{i,g\,'}(T_p^{i,g}) = \left[\frac{U_0^{i,g}\left(1-\frac{T_p^{i,g}}{T_c}\right)^{q^{i,g}}\left(1+p^{i,g}\frac{T_p^{i,g}}{T_c-T_p^{i,g}}\right)}{k_B T_p^{i,g}\ln\left(\frac{\tau^{i,g}}{\tau_0^{i,g}}\right)}\right]^{\frac{1}{\mu^{i,g}}}. \tag{V.17}$$

Then, by considering possible crossovers from the flux creep regime to the taff and parallel regimes with increasing temperature, the Eqs. (V.17) have been used to fit the

plot of $B_{ac\,1}^{i\,\prime}(T_p^i)$ and $B_{ac\,1}^{g\,\prime}(T_p^g)$ at temperatures below the crossover temperatures T_{ct}^* and T_{cf}^*, respectively. This has given the parameters $U_0^{i,g}$, $\mu^{i,g}$ which have been used to fit the times plots with the Eqs. (V.12)-(V.16).

It is worth noting that such kind of determination of all the involved parameters by means of independent fits of data has reduced the uncertainty of the fits results. Moreover, the parameters $q^{i,g}$, $\mu^{i,g}$, $\alpha^{i,g}$ and $\beta^{i,g}$ can assume few fixed values and then have been varied among these quantized values, and this further reduced the uncertainty of the fits results. In fact, we have varied the dynamical parameters as $q^{i,g} = 1/2, 1, 3/2, 2$ related to the system dimensionality, $\mu^{i,g} = 1/7, 3/2, 7/9$ related to the dimensions of the creep flux bundles within the collective creep[38] and the relaxational parameters as $\alpha^{i,g} = 0.25,0.5,0.75,1$, $\beta^{i,g} = 0.25,0.5,0.75,1$. within the relaxational model.

As an example, the curves of $\tau^i(T_p^i)$ and $\tau^g(T_p^g)$ at $\mu_0 H_{ac} = 0.2$ mT are shown in the Fig. V.12a together with the best fit among the Eqs. (V.12)-(V.16) which was found the crossover from the flux creep regime to the taff regime inside both the inter- and intragranular volume fractions of the sample. The corresponding plots of $B_{ac\,1}^{i,g\,\prime}(T_p^{i,g})$ are shown in the Fig. V.12b together with the fits to the Eqs. (V.17). The value of parameters obtained from all these fit are reported in the TableV.1.

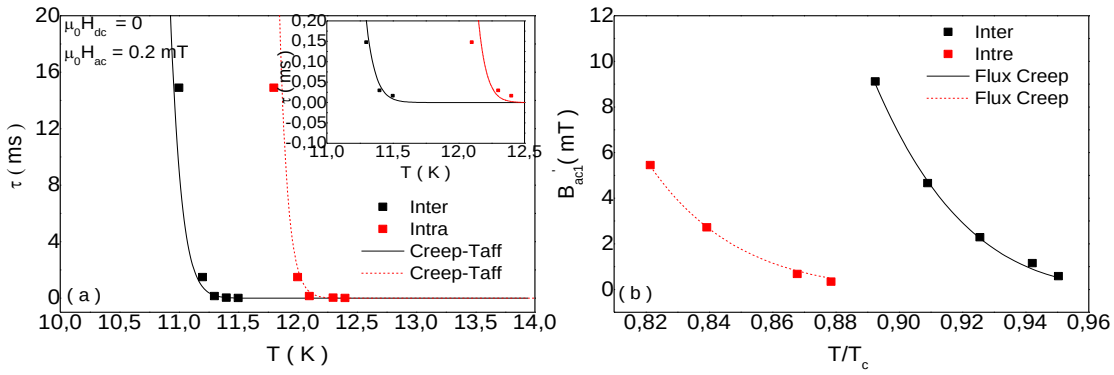

Figure V.12 (a) Plots of the temperature dependence of the inter- and intragranular relaxation times for the $FeSe_{0.5}Te_{05}$ sample extracted from the analysis of the $M_1''(T)$ curves of the Fig. V.2b according to the Eq. (V.9) together with the fit to the temperature dependence of the time in the case of crossover from the flux creep to the taff regime. (b) Plots of the temperature dependence of the amplitude of the in-phase effective AC field first harmonic acting on the sample's and grains's surfaces extracted from the $M_1''(T)$ curves in the Figs. V.10a and V.10c, together with the fit to the Eq. (V.17).

Parameter	Intergranular	Intragranular
q	$3/2$	$3/2$
μ	$1/7$	$1/7$
T_{ct}^{*}	11.2 K	12 K
α	0.25	0.75
β	0.25	0.75

Table V.1 Value of parameters involved in the Eqs. (V.10) and (V.12)-(V.16) obtained from the best fit with these equations of the plots of $\tau^{i}(T_p^{i})$ and $\tau^{g}(T_p^{g})$ in the Fig. V.11a.

V.4.4 Inter- and intragranular AC susceptibilities first harmonic

The temperature dependence of the first and third harmonic real and imaginary parts of the inter- and intragranular AC susceptibilities have been numerically calculated by solving the system of equations (V.2a)-(V.2d), together with the Eqs. (V.3a) and (V.3b) for the real and imaginary parts of the fundamental susceptibilities, respectively. In these last equations the temperature dependences of the flux relaxation times, preliminarily calculated from the analysis discussed above of the experimental curves of $M_1^{''}(T)$, have been used.

The solution of the system of equations (V.2a)-(V.2d) has been performed by means of a numerical programmed algorithm. As an example, the curves of ${\chi^{i,g}}_1^{'}(T)$, ${\chi^{i,g}}_1^{''}(T)$ and ${\chi^{i,g}}_3^{'}(T)$, ${\chi^{i,g}}_3^{''}(T)$, obtained as solutions of the system at $\mu_0 H_{ac} = 0.2$ mT and $\nu = 107$ Hz, are reported in the Figs. V.13. In particular, according with the Eqs. (V.3a) and (V.3b) are independent of the geometric profile of the grains. The influence of the grains geometry on the AC magnetic response will be discussed later.

The first harmonics curves ${\chi^{i,g}}_1^{'}(T)$ and ${\chi^{i,g}}_1^{''}(T)$, shown in the Figs. V.13a and V.13b, respectively, exhibit the typical behaviour expected for superconducting system and discussed in the Chapter II. In fact, the inter- and intragranular real parts ${\chi^{i}}_1^{'}(T)$ and ${\chi^{g}}_1^{'}(T)$ exhibit two steps at lower and higher temperatures, respectively, which are the inter- and intragranular superconducting critical temperatures T_c^{i} and T_c^{g}. Correspondingly, two peaks appear in the imaginary parts ${\chi^{i}}_1^{''}(T)$ and ${\chi^{g}}_1^{''}(T)$ at the lower and higher temperatures T_p^{i} and T_p^{g}, respectively.

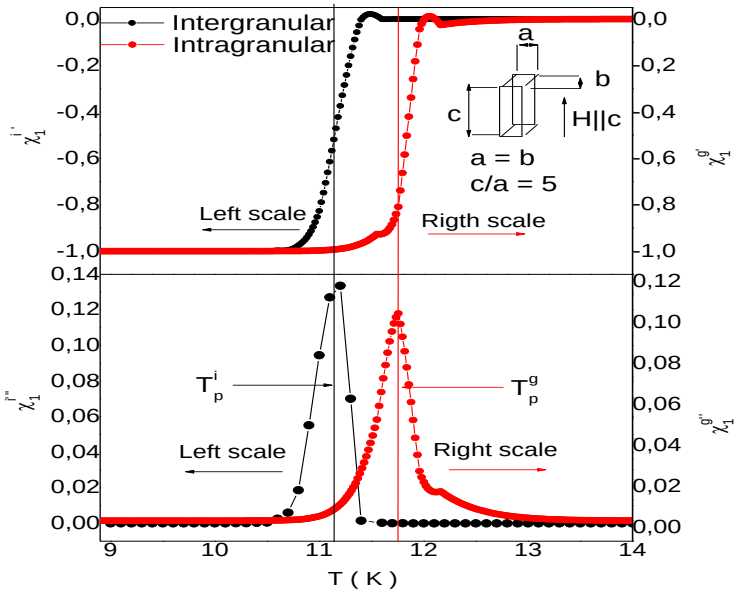

Figure V.13 Temperature dependence of the inter- and intragranular susceptibilities first harmonics (a) real and (b) imaginary parts of the $FeSe_{0.5}Te_{05}$ sample for $a = b$ and $c/a = 5$, as obtained by solving the system of Eqs. (V.2a)-(V.2d) for the flux dynamical regime of crossover from the flux creep to the taff as found from the fit of the plots of $\tau^i(T_p^i)$ and $\tau^g(T_p^g)$ in the Fig. V.12a, and $B_{ac\,1}^{i\,'}(T_p^i)$ and $B_{ac\,1}^{g\,'}(T_p^g)$ in the Fig. V.12b. The left and right scales refer to inter- and intragranular susceptibilities, respectively. The vertical lines indicate the peak temperatures in the $\chi^{i\,''}_1(T)$ and $\chi^{g\,''}_1(T)$.

4.4.4.1 Temperature dependence of the effective demagnetizing factor k_d of grains

The curves of the temperature dependences of the effective demagnetizing factor k_d and of the effective penetration depth of the grains λ^g, have been obtained from the curves of the intragranular AC susceptibility first harmonic determined by solving the system of equations (V.2a)-(V.2d) and shown in the Figs. V.13a and V.13b. In fact, an effective penetration depth of the grains as correction of the critical state has been calculated from the curves of $\chi^{g\,'}_1(T)$ and $\chi^{g\,''}_1(T)$ as[43-46]

$$\frac{\lambda^g(T)}{a} = 1 - \frac{\chi^{g\,'}_1(T) + \frac{15\pi}{32}\chi^{g\,''}_1(T)}{\chi^{g\,'}_1(0) + \frac{15\pi}{32}\chi^{g\,''}_1(0)}, \qquad \text{(V.18)}$$

where $2a$ is the grains width in the plane perpendicular to the magnetic field direction (see the Figs. IV.1 and IV.2). This effective penetration depth has been used to calculate the effective demagnetizing factor $k_d(T)$ of the grains introduced in the Chapter IV and quantifying the demagnetizing field in the intergranular region due demagnetizing fields. The plot of $k_d(T)$ calculated with the Eq. (IV.16) from the curves of the Fig. V.13a and V.13b for different values of the c/a ratio determining the geometric profile of the grains with $a = b$, are reported in the Fig. V.14a. The corresponding plots of $\lambda^g(T)$ is shown in

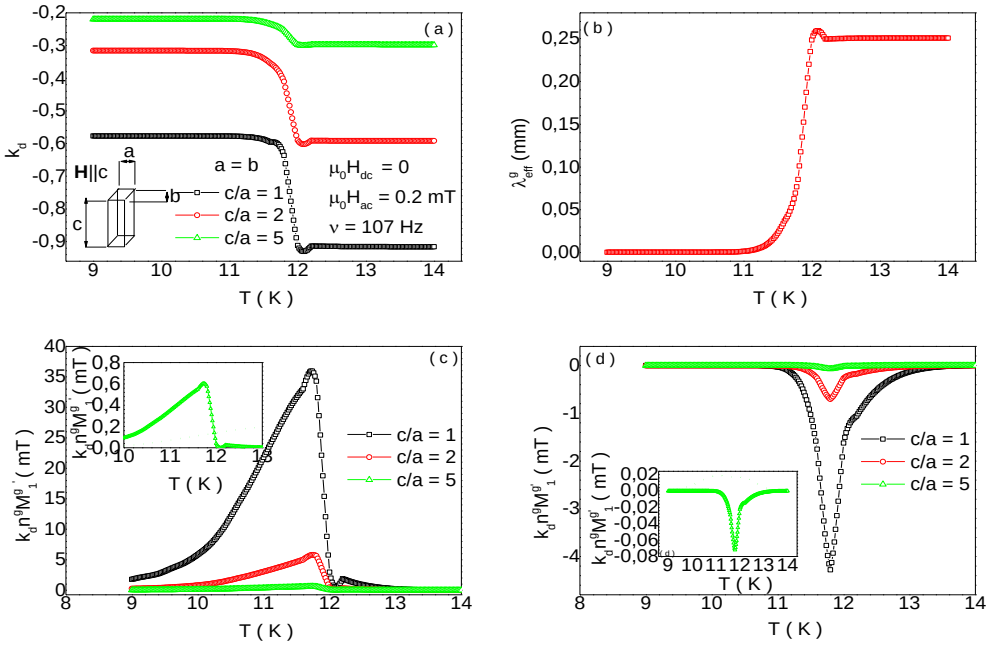

Figure V.14 Temperature dependence of (a) the effective demagnetizing factor for $a = b$ and with varying the c/a ratio, (b) the intragranular effective penetration depth (not depending on the grains geometry) for $c/a = 5$, (c) the in-phase demagnetizing field $k_d(T)n^g M^{g'}_1(T)$ and (d) the out-of-phase demagnetizing field $k_d(T)n^g M^{g''}_1(T)$ for $a = b$ and with varying the c/a ratio, as obtained from the curves of $\chi^{g'}_1(T)$ and $\chi^{g''}_1(T)$ in the Figs. V.13a and V.13b for the $FeSe_{0.5}Te_{05}$ sample. The insets show enlargements for the $c/a = 5$ curve together with (dashed lines) the effective field amplitudes.

the Fig. V.14b.

Although the AC susceptibility first harmonic curve is independent of the grains geometry, the curve of $k_d(T)$ is strongly dependent on the c/a ratio, as the curves of the temperature dependence of the corresponding demagnetizing fields coming from the grains in the intergranular region defined in the Eq. (IV.15). The in-phase and out-of-phase components of the first harmonic of this field, $k_d(T)n^g M^{g'}_1(T)$ and $k_d(T)n^g M^{g''}_1(T)$, are shown in the Figs. V.14c and V.19d, respectively, for different values of the c/a ratio. From these curves a focusing of the magnetic field induction is evident, of amount depending on the grains geometric profile. In particular, the absolute values both of $k_d(T)$ and of $k_d(T)n^g M^{g'}_1(T)$ and $k_d(T)n^g M^{g''}_1(T)$ decrease with increasing the height of the granular rectangular prism with respect to the area of base. This is expected since, with the elongation of the prism in the field direction, the contribution to the magnetic field induction outside the grains produced by both the intragranular shielding currents and the shape of the grains by means of stray fields decrease. The smallest absolute values of the in-phase and out-of-phase demagnetizing fields are ≈ 0.6 mT and ≈ 0.08 mT at $c/a = 5$, respectively.The effect of the magnetic

flux focusing is to increase the actual amplitude of the magnetic field induction at the grains's surfaces, which corresponds to the temperature dependent effective fields amplitudes $B_{ac\,1}^{g\,'}(T)$ and $B_{ac\,1}^{g\,''}(T)$ of the Figs. V.10c-d. Since this gives an effective magnetic response by the grains it also influence the whole sample measured magnetization and then the intergranular magnetic response via the corresponding effective magnetic field induction. In fact, the effects of the existence of demagnetizing effects have been analyzed on both the first and third harmonics of the inter- and intragranular AC susceptibilities. The curves of the $\chi^{i,g\,'}{}_1(T)$and $\chi^{i,g\,''}{}_1(T)$ calculated at different values of the c/a ratio of the grains geometric profile (not reported here) have been found not depending on the grains geometric profile. On the other hand, a considerable dependence on the grains prism c/a ratio has been found for the $\chi^{i,g\,'}{}_3(T)$ and $\chi^{i,g\,''}{}_3(T)$ curves, as will be discussed later.

V.5 Analysis of the inter- and intragranular AC susceptibilities first harmonics

In the following, the curves of $\chi^{i,g\,'}{}_1(T)$ and $\chi^{i,g\,''}{}_1(T)$, numerically calculated by solving the system of equations (V.2a)-(V.2d), will be analyzed in order to extract the superconducting parameters and flux dynamical information of the individual grains and of the intergranular contacts. In fact, it has been shown in the Chapter III as the analysis of the dissipation peaks in the curves of the temperature dependent imaginary part of the AC susceptibility of a homogeneous system can be used to estimate the temperature dependence of the superconducting critical current densities and of the activation energy governing the process of flux relaxation inside the system. Then, beyond the same kind of analysis performed in the initial part of this Chapter on the curves of the whole sample magnetization without considering demagnetizing effect, in the following we will analyze separately the inter- and intragranular intrinsic susceptibilities which have been determined taking into account the existence of effective magnetic fields due to demagnetizing effects.

At this aim the curves of $\chi^{i,g\,'}{}_1(T)$ and $\chi^{i,g\,''}{}_1(T)$ for different values of the applied AC field amplitude and at a fixed AC frequency have been numerically calculated by means of the solution of the system of equations (V.2a)-(V.2d), after determining the actual flux dynamical regime governing the AC responses of the grains and of the intergranular contacts, and are shown in the Fig. V.15a and V.15b, respectively, for a fixed geometric profile of the grains. As expected, the $\chi^{i,g\,'}{}_1(T)$ curves exhibit a shift of the

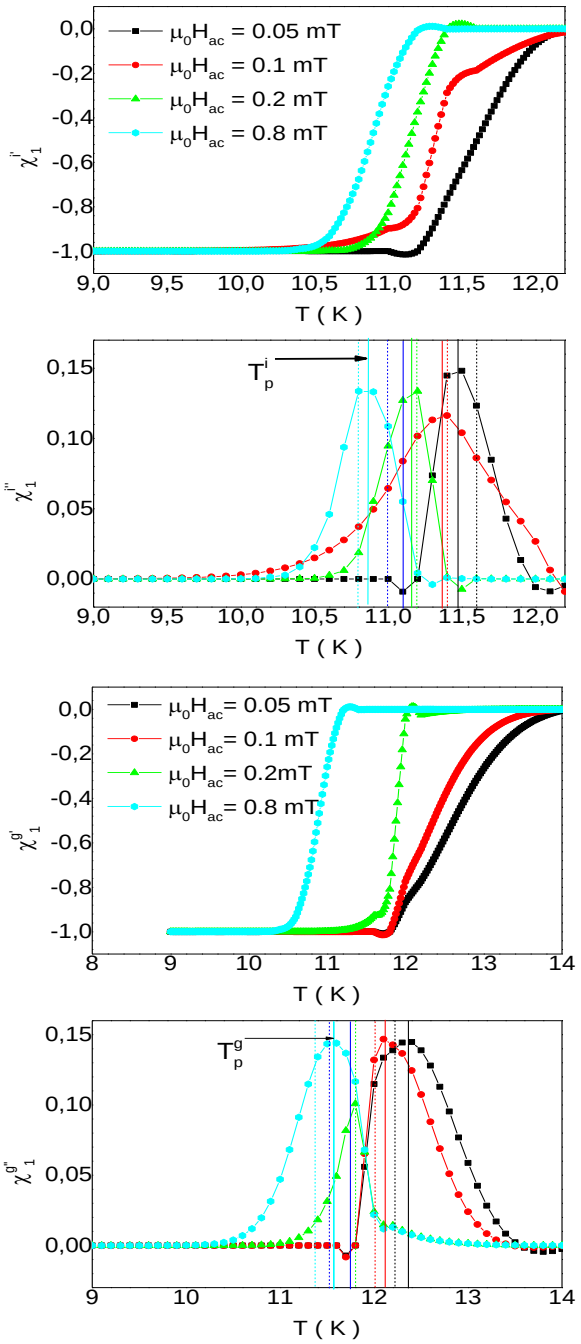

Figure V.15 Temperature dependence of (a) the real and (b) the imaginary parts of the intergranular susceptibility first harmonics and (c) the real and (d) the imaginary parts of the intragranular susceptibility first harmonics, for the $FeSe_{0.5}Te_{05}$ sample with $a = b$ and $c/a = 5$, as obtained by solving the system of Eqs. (V.2a)-(V.2d). The vertical lines indicate the peak temperatures in the $\chi^{i}{}_{1}^{''}(T)$ and $\chi^{g}{}_{1}^{''}(T)$ curves (solid) with and (dashed) without the demagnetizing effects.

superconducting transition towards lower temperature with increasing the AC field amplitude which oppose the superconductivity. In particular, a change in the aspect of the transition occurs with varying the AC field amplitude, which could be further investigated in relation with the flux dynamics governing the magnetic responses.

Moreover, the dissipation peaks in the $\chi^{i,g}{}_{1}^{''}(T)$ are move towards lower temperature with

increasing the field amplitude as found in the curves of the out-of-phase component of the whole sample magnetization (see the Fig. V.8b). However, these peaks are slightly shifted with respect to the peaks observed in the corresponding curves of the whole sample magnetization without considering the demagnetizing effects, especially for the intragranular magnetic response. This may affect the estimation of the effective critical current densities as it will be discussed in the following.

V.5.1 Estimation of the superconducting critical current densities $j_c^{i,g}$

According to the Eq.(III.2) the temperature dependence of the inter- and intragranular critical current densities of a granular superconducting system can be extracted from the analysis of the temperature dependent imaginary parts of the first harmonics of the inter- and intragranular AC susceptibilities. In fact, the peaks in ${\chi^i}_1''(T)$ and ${\chi^g}_1''(T)$ are expected when the field at the centre of the sample and of the gains, respectively, reaches the value of applied AC field amplitude. Then, when considering the existence of effective magnetic field inductions ${B^i_{ac}}_1'$ and ${B^g_{ac}}_1'$ due to demagnetizing effects, the plots of the temperature dependent critical current densities can be constructed by taking the peak temperatures $T_p^{i,g}$ in the ${\chi^{i,g}}_1''(T)$ curves and the values of ${B^i_{ac}}_1'(T_p^i)$ and ${B^g_{ac}}_1'(T_p^g)$. The figs. V.16a and V.16b show, respectively, the plots of $L\mu_0 j_c^i(T_p^i)$ and $c\mu_0 j_c^g(T_p^g)$, with $2L$ and $2c$ the width of the sample and of the grains, respectively, obtained from the analysis of the ${\chi^i}_1''(T)$ and ${\chi^g}_1''(T)$ curves in the Fig. V.3b and of the curves of ${B^i_{ac}}_1'(T)$ and ${B^g_{ac}}_1'(T)$ in the Figs. V.10a and V.10c. The plots of $L\mu_0 j_c^i(T_p^i)$ and $c\mu_0 j_c^g(T_p^g)$ obtained without consider the existence of demagnetizing effects from the analysis of the curves of the out-of-phase whole sample magnetization $M_1''(T)$ (see the Fig. V.5) have been also reported for a comparison, and all the plots are fitted with an exponential decay. In fact, a raise and a drop appear in the $L\mu_0 j_c^i(T_p^i)$ and $c\mu_0 j_c^g(T_p^g)$ curves, respectively, in the region of the dissipation peaks in the ${\chi^i}_1''(T)$ and ${\chi^g}_1''(T)$ curves when considering the demagnetizing effects. This is due to both the existence of effective magnetic field inductions ${B^i_{ac}}_1'(T_p^i)$ and ${B^g_{ac}}_1'(T_p^g)$ different from the applied field which produce also a shift of the dissipation peaks in the ${\chi^i}_1''(T)$ and ${\chi^g}_1''(T)$ Then, the inter- and intragranular critical current densities result under- and overestimated, respectively, in the region of intermediate temperature, when the existence of demagnetizing effects is neglected.

Related with the inter- and intragranular critical current densities it is very crucial for the application to known the AC losses inside both the inter- and intragranular volume

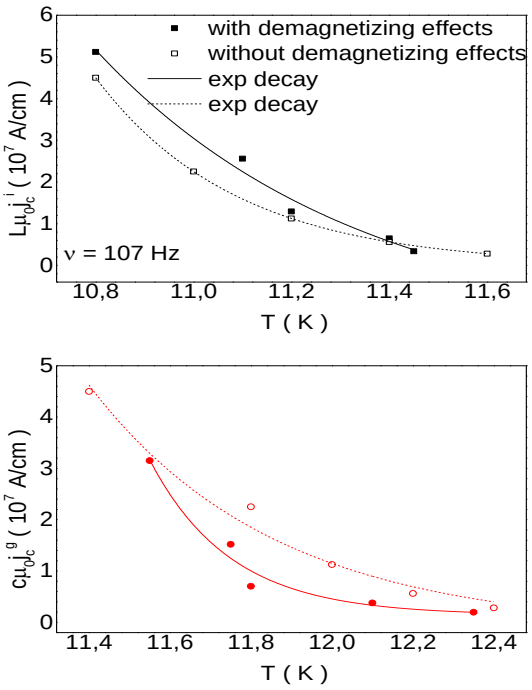

Figure V.16 Plots of the temperature dependence of (a, closed symbols) $L\mu_0 j_c^i$ and (b, closed symbols) $c\mu_0 j_c^g$ as function of the temperature of the $FeSe_{0.5}Te_{05}$ sample, constructed according to the Eq. (III.2) by taking the peak temperatures $T_p^{i,g}$ in the curves of the Figs. V.3b and the value of $B_{ac\,1}^{i,g\,\prime}(T_p^{i,g})$ in the Figs.V.10a and V.10c. The open symbols are the results obtained without considering the demagnetizing effects (see the Fig. V.5). The lines are the fit of the data with an exponential decay.

fractions of the sample. According to the Eq. (II.32), the energy converted into heat during a cycle of the AC field per unit volume of the inter- and intragranular fraction of the sample can be obtained from the analysis of the inter- and intragranular dissipation peaks height in the $\chi^{i}{}_1^{''}(T)$ and $\chi^{g}{}_1^{''}(T)$ curves, respectively. In fact, these heat losses are given by

$$W^{i,g}{}_q = -\pi\chi^{i,g}{}_1^{''}\left(T_p^{i,g}\right)\frac{B_{ac\,1}^{i,g\,\prime\,2}}{\mu_0}. \qquad \text{(V.19)}$$

The plots of $W^{i}{}_q$ and $W^{g}{}_q$ as function of the amplitude of the applied AC field amplitude $\mu_0 H_{ac}$ are shown in the Fig. V.17, as extracted from the curves of the Fig. V.2b. The plots of $W^{i}{}_q$ and $W^{g}{}_q$ as function of $\mu_0 H_{ac}$ obtained, without considering the existence of demagnetizing effects, from the analysis of the curve of the out-of-phase whole sample magnetization $M_1^{''}(T)$, are also reported for a comparison. The difference between the curves obtained with and without taking into account the existence of effective magnetic fields due to the demagnetizing effects indicates that on the peaks height and then on the estimation of the inter- and intragranular losses.

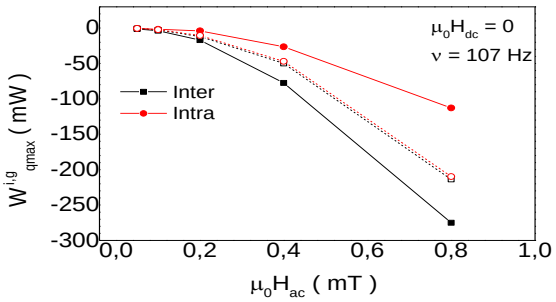

Figure V.17 Plots of the inter- and intragranular dissipations $W^{i,g}{}_q$ as function of the amplitude of the applied field of the of the $FeSe_{0.5}Te_{05}$ sample (closed symbols, solid lines) with and (open symbols, dash lines) without considering the existence of demagnetizing effects, constructed from the curves of the Fig. V.2b according to the Eq. (V.19).

V.5.2 Estimation of the vortex activation energies $U^{i,g}$

The temperature and field dependences of the activation energies, governing the relaxation of magnetic flux inside the inter- and intragranular volume fractions of the sample in presence of thermally activated flux dynamical regimes, have been extracted previously from the analysis of the experimental curves of the temperature dependent out-of-phase component of the whole sample magnetization $M_1^{''}(T)$ (see the Fig. V.7). In fact, the activation energies $U_a^{i,g}$ at a fixed amplitude of the AC field have been obtained as the slope of the Arrhenius plot of the $\ln(\nu)$, with ν the measuring frequency, as function of the inverse of the peak temperatures in the $M_1^{''}(T)$ curves. However, it is worth underline that the existence of temperature dependent effective magnetic field inductions governing the inter- and intragranular magnetic responses due to demagnetizing effects may influence the actual positions of the dissipation peaks in the inter- and intragranular AC susceptibility first harmonics imaginary parts. In this case, the estimation of the activation energies from the slopes of the Arrhenius plots is expected to be influenced.

In the current analysis the field and temperature dependences of the inter- and intragranular activation energies obtained from the curves of $\chi^{i}{}_1^{''}(T)$ and $\chi^{g}{}_1^{''}(T)$ calculated in presence of effective magnetic field inductions due to demagnetizing effect, will be discussed. In this case, the activation energies of the inter- and intragranular volume fractions are obtained as results of the fit of the temperature dependent relaxation times giving the actual flux dynamical regime governing the magnetic flux relaxation processes. The existence of temperature dependent effective magnetic field inductions is taken into account by means of the actual current dependence of the activation energy in the universal expression of the Eq. (V.11). In fact, from the time equation (V.10) the activation energies $U_a^{i,g}$ are given by

$$U_a^{i,g}(T, B_{ac}^{i,g'}{}_1) = k_B T \ln\left[\frac{\tau^{i,g}(T, B_{ac}^{i,g'}{}_1)}{\tau_0^{i,g}}\right], \quad \text{(V.20)}$$

where $\tau^{i,g}(T)/\tau_0^{i,g}$ is given by the result of the fits of the relaxation times plots in the Figs. V.12a which determined the actual flux dynamical regimes governing the inter- and intragranular AC responses. The plot of $U_a^i(T, B_{ac}^{i,g'}{}_1)$ and $U_a^g(T, B_{ac}^{i,g'}{}_1)$ calculated with the Eq. (V.20) at different amplitudes of the AC fields are shown in the Figs.V.18a and V.18b, respectively. Both energies decrease with increasing temperature in the region of temperatures between the full diamagnetic shielding and the superconducting transitions, as expected for thermally activated motion regimes. In particular, the obtained temperature behaviors are expected within the Anderson-Kim theory of flux creep discussed in the previous chapters[25,26] and they have been found in several high-T_c and Fe-based superconductors, where a power law temperature dependence have been considered[11,47-51]. Although similar results were found from the analysis of the whole sample magnetization without considering demagnetizing effects (see the Fig. V.7b), the current results are valid for the whole continue range of temperatures and for different AC fields amplitudes.

Moreover, with varying the amplitude of the AC field, the curves of $U_a^i(T)$ in the Fig. V.18a exhibit opposite nonmonotonic variations. In fact, the curves of $U_a^i(T)$ tend to low and to raise at lower and higher fields amplitudes, respectively, while the curves of $U_a^g(T)$ exhibit a contrary behavior, with increasing the AC field amplitude. These trends are confirmed from the plots of $U_a^i(\mu_0 H_{ac})$ and $U_a^g(\mu_0 H_{ac})$ at different temperatures, shown in the Figs. V.18c and V.18d, respectively, obtained by performing isothermal cuts at different temperatures of the curves in the Fig. V.18a and V.18b. It is well known that the field dependence of the activation energy of a superconducting system is typically described with a power law with a negative exponent depending on the pinning mechanism[14,38,47-51]. In fact, low absolute values of the exponent correspond to a strong single vortex pinning while higher absolute values correspond to a weak collective pinning. However, the results of the Fig. V.18a-d indicate a power law decay at lower temperature for the intergranular energy U_a^i, while an anomalous increase of this energy with the field amplitude occurs at higher field amplitudes. On the other hand, the intragranular energy U_a^g has been found to be almost constant at small AC field amplitudes, while at higher amplitudes it increases with the field up to a maximum followed by a diminution. It is worth noting that the same anomalous behaviours of both U_a^i and U_a^g with varying the AC field amplitude were also found from the analysis of the

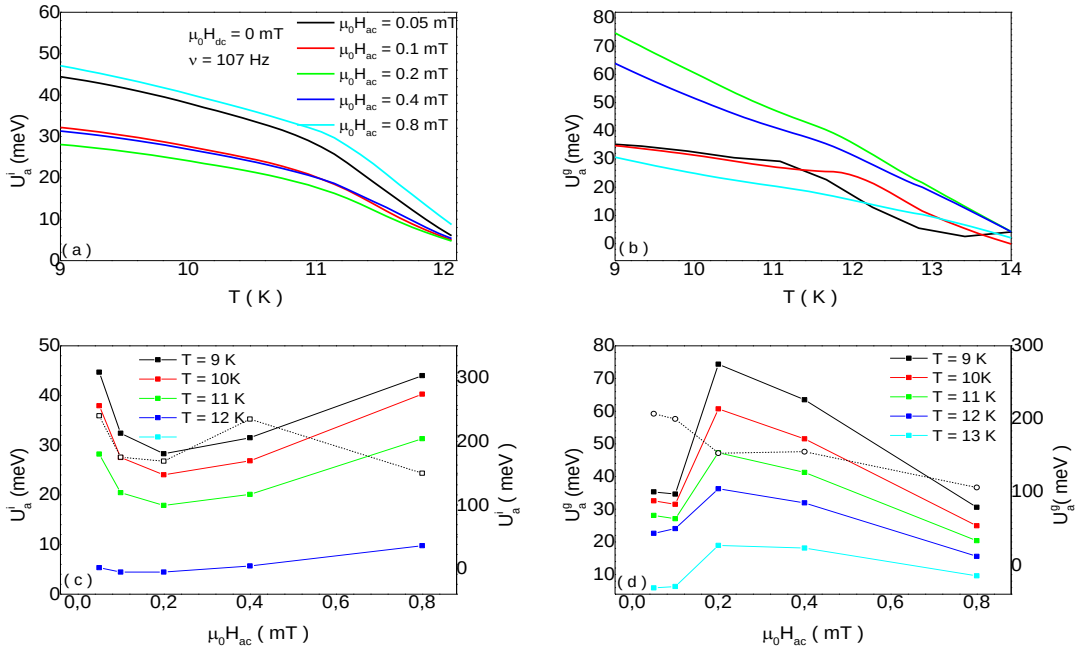

Figure V.18 (Up) Plots of the inter- and intragranular activation energies $U_a^{i,g}$ as function of the temperature for the $FeSe_{0.5}Te_{05}$ sample calculated with the Eq. (V.20) after determining the temperature dependence of the relaxation times $\tau^{i,g}$ for the actual flux dynamical regimes. (Down) Plots of $U_a^{i,g}$ as function of the applied AC field amplitude obtained from isothermal cuts of the $U_a^{i,g}(T)$ curves. The dashed lines and open symbols are the results obtained without considering the demagnetizing effects (see the Fig. V.7a).

Arrhenius plots without considering the demagnetizing effects in the initial part of this chapter. Beyond the need to investigate this kind of behaviors which could be related to the flux dynamics and system dimensionality[52-54], we found considerable deviations of the energies values with and without considering the existence of demagnetizing effects, as shown from the comparison of the curves obtained in the two kinds of analysis and shown in the Figs. V.18c and V.18d. In particular, one couple of curves of $U_a^i(\mu_0 H_{ac})$ and $U_a^g(\mu_0 H_{ac})$ there exist from the Arrhenius plots due to the way to perform these plots where the temperature is a variable.

V.6 Analysis of the inter- and intragranular AC susceptibilities third harmonics

The third harmonic curves of $\chi^{i,g}{}_3^{'}(T)$ and $\chi^{i,g}{}_3^{''}(T)$, obtained as solution of the system of Eqs. V.2a)-(V.2d) by using the Eqs. (V.3a) and (V.3b) for the real and imaginary parts of the fundamental susceptibilities with the temperature dependences of the flux relaxation times preliminarily calculated from the analysis of the experimental curves of $M_1^{''}(T)$, are shown in the Figs. V.19a and V.19b. These curves can be

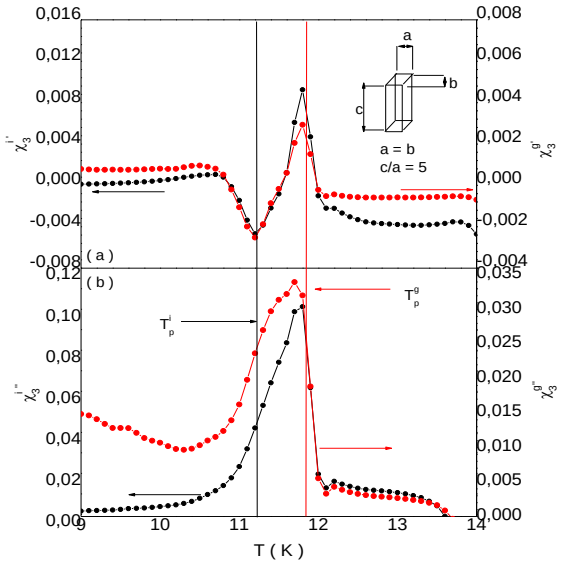

Figure V.19 Temperature dependence of the inter- and intragranular susceptibilities third harmonics (a) real and (b) imaginary parts of the $FeSe_{0.5}Te_{05}$ sample for $a = b$ and $c/a = 5$, as obtained by solving the system of Eqs. (V.2a)-(V.2d) for the flux dynamical regime of crossover from the flux creep to the taff with increasing temperature as found from the fit of the plots of $\tau^i(T_p^i)$ and $\tau^g(T_p^g)$ in the Fig. V.12a, and $B_{ac}^{i}{}_1'(T_p^i)$ and $B_{ac}^{g}{}_1'(T_p^g)$ in the Fig. V.12b. The left and right scales refer to inter- and intragranular susceptibilities, respectively. The vertical lines indicate the peak temperatures in the $\chi^{i}{}_1''(T)$ and $\chi^{g}{}_1''(T)$ of the Figs. V.13b.

interpreted in relation to the same curves theoretically predicted by solving the equation of diffusion of the magnetic flux for a homogeneous superconducting system discussed in detail in the Chapter II. In fact, a negative peak at a lower temperature and a positive peak at a higher temperature appear both in the intergranular real part $\chi^{i}{}_3'(T)$ and in the intragranular real part $\chi^{g}{}_3'(T)$. In particular, the intergranular negative peak appears at the peak temperature T_p^i of the $\chi^{i}{}_1''(T)$ curve, while the intragranular negative peak appears at a temperature lower than the peak temperature T_p^g of the $\chi^{g}{}_1''(T)$ curve. From the comparison of these features with the curves numerically calculated for a homogeneous sample by solving the diffusion equation and shown in the Figs. II.5a-h, the shapes of $\chi^{i,g}{}_3'(T)$ in the Fig. V.19a are compatible with the existence of a crossover from the flux creep regime to the taff regime with increasing temperature as found from the fit of the temperature dependent relaxation times discussed above. In fact, a negative peak is predicted at lower temperature due to the flux creep regime and at higher temperature due to the taff regime, as observed in the $\chi^{i}{}_3'(T)$ and $\chi^{g}{}_3'(T)$ curves of the Fig. V.13a. Moreover, a positive peak is predicted at lower temperature due to the flux creep regime and at higher temperature due to the taff regime, which are compatible with the presence of the large positive peaks in the $\chi^{i}{}_3''(T)$ and $\chi^{g}{}_3''(T)$ curves in the Fig.

V.13b. It is worth noting that the intragranular curves $\chi^{g'}{}_3(T)$ and $\chi^{g''}{}_3(T)$ appear more distant from the peak temperature of the corresponding $\chi^{g''}{}_1(T)$ curve, with respect to the intergranular curves $\chi^{i'}{}_3(T)$ and $\chi^{i''}{}_3(T)$ from the peak temperature of the $\chi^{i''}{}_1(T)$ curve. Since it is typically observed a shift towards lower temperatures, with increasing the AC field amplitude, of the temperature dependent third harmonic real and imaginary parts of the AC susceptibility of a superconducting system in presence of flux dynamical nonlinear regimes[36,37], it is useful to analyze the effect of the magnetic flux focusing in the intergranular region found from the Figs. V.14a-d on the $\chi^{i,g'}{}_3(T)$ and $\chi^{i,g''}{}_3(T)$ curves of the $FeSe_{0.5}Te_{05}$ sample.

In fact, although the first harmonic curves have been found not depending on the geometric profile of the grains determining the effective demagnetizing factor of the grains, a considerable dependence on the grains prism c/a ratio has been found for the $\chi^{i,g'}{}_3(T)$ and $\chi^{i,g''}{}_3(T)$ curves, as shown in the Figs. V.20a-d. In particular, the negative peak in the $\chi^{i'}{}_3(T)$ and $\chi^{g'}{}_3(T)$ curves in the regions of lower temperature tend to disappear while the positive peak at higher temperature tend to rise with increasing the c/a ratio (see the Figs. V.20a and V.20b), and an increase of the single positive peak occurs in the corresponding imaginary parts (see the Figs. V.20c and V.20d).

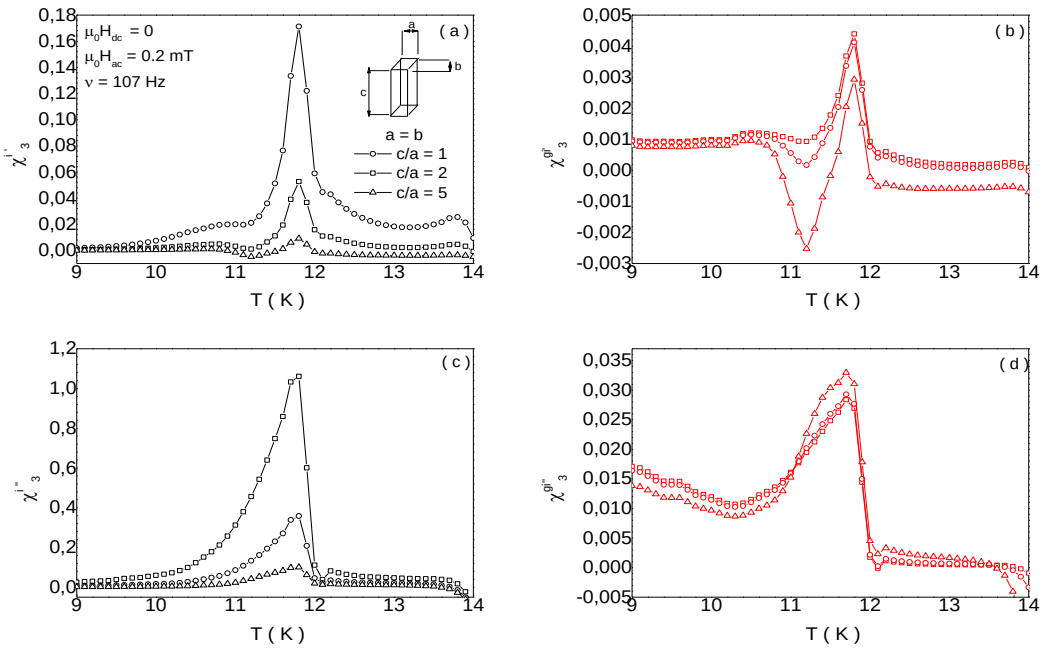

Figure V.20 Temperature dependence of (left) (a) the real and (b) the imaginary part of the intergranular susceptibility third harmonic and (right) (c) the real and (d) the imaginary part of the intragranular susceptibility third harmonic, calculated at different values of the c/a ratio by solving the system of Eqs. (V.2a)-(V.2d) for the $FeSe_{0.5}Te_{05}$ sample.

This can be considered as fingerprint of change in the flux dynamical regime, since it is well known that the third harmonic of the complex susceptibility is more sensitive than the first one to the variations in the flux dynamical regime governing the AC magnetic response of a superconducting system due to variations in the exciting field. In fact, variations in the effective magnetic field inductions acting on the grains's surfaces occur due to the focusing effect of the magnetic flux in the intergranular region deduced from the Figs. V.14c and V.14d. Since this influence the sample magnetization, it affects also the effective magnetic field acting on the sample's surface and governing the intergranular magnetic response.

Then, it is interesting to investigate the dependences of both the inter- and intragranular third harmonic curves on the amplitude of the applied AC field. In fact, the curves of $\chi^{i,g}{}'_3(T)$ and $\chi^{i,g}{}''_3(T)$ calculated by solving the system of equations (V.2a)-(V.2d) at different AC field amplitudes are shown in the Figs. V.21a and V.21b, respectively. All the curves move towards lower temperature with increasing the AC field

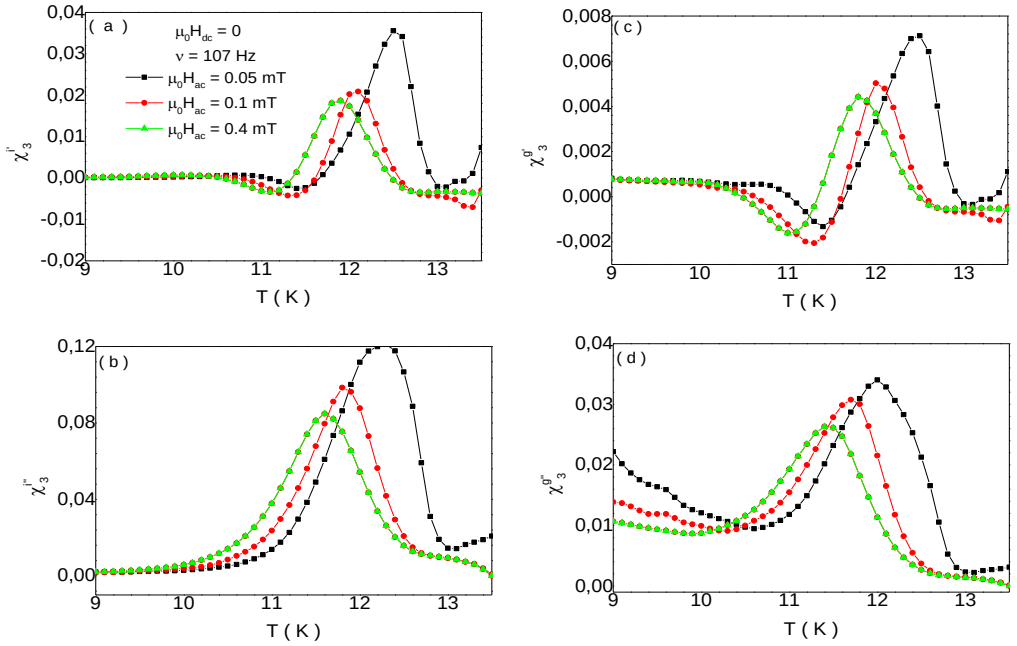

Figure V.21 Temperature dependence of (a) the real and (b) the imaginary parts of the intergranular susceptibility third harmonics and (c) the real and (d) the imaginary parts of the intragranular susceptibility third harmonics, for the $FeSe_{0.5}Te_{05}$ sample with $a = b$ and $c/a = 5$, as obtained by solving the system of Eqs. (V.2a)-(V.2d) at different AC field amplitudes. The vertical lines indicate the peak temperatures in the $\chi^{i}{}''_1(T)$ and $\chi^{g}{}''_1(T)$.

amplitude. Moreover, in the both the real part $\chi^{i}{}'_3(T)$ and $\chi^{g}{}'_3(T)$ the negative peak at lower temperature is almost constant while the positive peak at higher temperature tend to

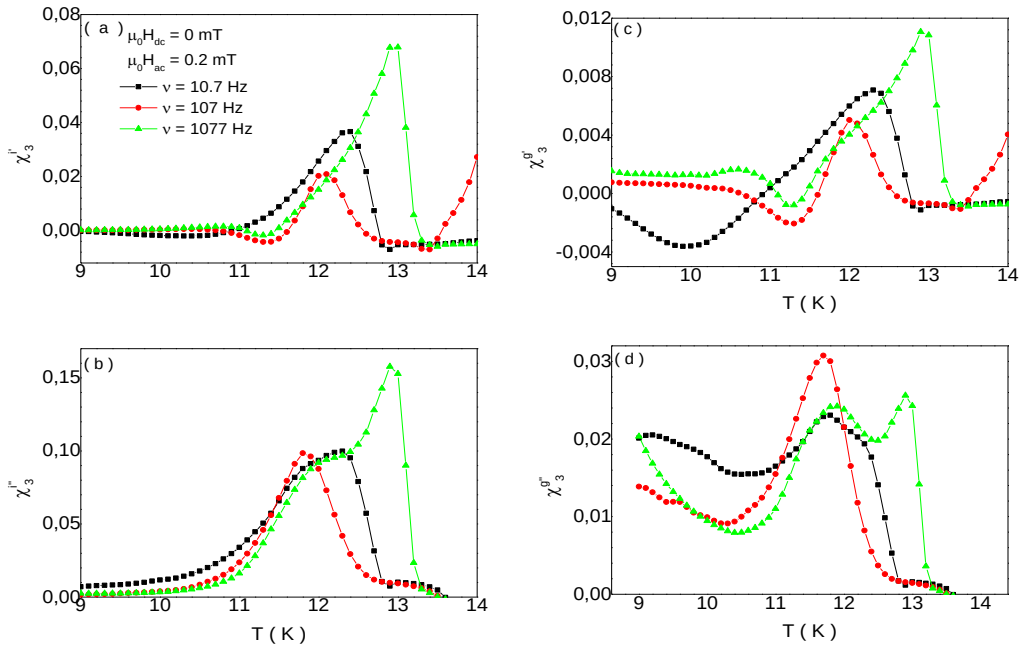

Figure V.22 Temperature dependence of (a) the real and (b) the imaginary parts of the intergranular susceptibility third harmonics and (c) the real and (d) the imaginary parts of the intragranular susceptibility third harmonics, for the $FeSe_{0.5}Te_{05}$ sample with $a = b$ and $c/a = 5$, as obtained by solving the system of Eqs. (V.2a)-(V.2d) at different AC field frequencies. The vertical lines indicate the peak temperatures in the $\chi^{i}{}_{1}^{''}(T)$ and $\chi^{g}{}_{1}^{''}(T)$.

low as the peak in the corresponding imaginary parts $\chi^{i}{}_{3}^{''}(T)$ and $\chi^{g}{}_{3}^{''}(T)$ with the increase of the AC field amplitude. We mention that from the calculation of the temperature dependence of the flux relaxation time in both the inter- and intragranular volume fractions the positive peak at higher temperature in the curves of $\chi^{i}{}_{3}^{'}(T)$ and $\chi^{g}{}_{3}^{'}(T)$ is expected to be governed by taff regime. In fact, the field behaviour of the higher temperature peak in the $\chi^{i,g}{}_{3}^{'}(T)$ and $\chi^{i,g}{}_{3}^{''}(T)$ curves is compatible with the field dependence of the taff regime in absence of DC field.

Finally, in order to look for a confirmation of the existence of the regime of crossover between the flux creep and taff from the frequency behaviour of the inter- and intragranular AC susceptibilities third harmonics, we report the curves of $\chi^{i,g}{}_{3}^{'}(T)$ and $\chi^{i,g}{}_{3}^{''}(T)$ at different AC frequencies and fixed AC field amplitude in the Figs. V.22a and V.22b, respectively, as calculated by solving the system of equations (V.2a)-(V.2d). All the curves exhibit a change of behaviour at $\nu = 1077$ Hz, as observed in the curves of the AC magnetic response third harmonic of the whole sample (see the Figs. V.9a and V.9b). In particular, above this frequency the motion of the curves towards higher temperature and their rise with increasing frequency are compatible with a crossover regime from the

flux creep to the taff. In fact, as expected, the negative peak in the real parts $\chi^{i'}{}_3(T)$ and $\chi^{g'}{}_3(T)$ rise and slightly move due to the flux creep behaviour, while the following positive peak in the same curves rise and move towards higher temperatures, with increasing frequency (see the Figs. III.12a-h)[57]. Moreover, in the imaginary parts $\chi^{i''}{}_3(T)$ and $\chi^{g''}{}_3(T)$ a double positive peak tends to emerge with increasing frequency, that could be due to the predominance of the positive peak expected for the taff with respect to the positive peak expected for the flux creep at higher and lower temperatures, respectively (see the Figs. III.12a-h).

Bibliography

[1] D. Mancusi, M. Polichetti, M. R. Cimberle and S. Pace, Supercond. Sci. Technol. 28 (2015) 095017.

[2] L. Bossoni, P. Carretta, M. Horvatić, M. Corti, A. Thaler and P. C. Canfield, Eur. Phys. Lett., 102 (2013) 17005.

[3] G. Prando *et al*., Physica C, 469 (2009) 529.

[4] L. M. Wang, U. C. Sou, H. C. Yang, L. J. Chang, C. M. Cheng, K. D. Tsuei, Y. Su, T. Wolf and P. Adelmann, Phys. Rev.B, 83 (2011) 134506.

[5] K. W. Yeh et al., Europhys. Lett., 84 (2008) 37002.

[6] A. Palenzona, A. Sala, C. Bernini, V. Braccini, M. R. Cimberle, C. Ferdeghini, G. Lamura, A. Martinelli, I. Pallecchi, G. Romano, M. Tropeano, R. Fittipaldi, A. Vecchione, A. Polyanskii, F. Kametani and M. Putti, Supercond. Sci. Technol., 25 (2012) 115018.

[7] T. Taen, T. Tsuchiya, Y. Nakajima and T. Tamegai, Phys.Rev. B, 80 (2009) 092502.

[8] Q. Li, W. Si and I. K. Dimitrov, Rep. Prog. Phys., 74 (2011) 124510.

[9] E. Bellingeri et al., Supercond. Sci. Technol., 27 (2014) 044007.

[10] E. Bellingeri et al, Appl. Phys. Lett., 96 (2010) 102512.

[11] A. Leo, G. Grimaldi, A. Guarino, F. Avitabile, A. Nigro, A. Galluzzi1, D. Mancusi, M. Polichetti, S. Pace, K. Buchkov, E. Nazarova, S. Kawale, E. Bellingeri, C. Ferdeghini Supercond. Sci. Technol., 28 (2015) 125001.

[12] M. Putti, R. Vaglio and J. M. Rowell, Supercond. Sci.Technol., 21 (2008) 043001.

[13] G. Prando, P. Carretta, R. De Renzi, S. Sanna, A. Palenzona, M. Putti and M. Tropeano, Phys. Rev. B, 83 (2011) 174514.

[14] A. P. Malozemoff, T. K. Worthington, Y. Yeshurun, F. Holtzberg and P. H. Kes, Phys. Rev. B, 38 (1988) 7203.

[15] M. K. Lee, E. V. Charnaya, C. Tien, L. J. Chang andY. A. Kumzerov, J. Appl. Phys., 113 (2013) 113903.

[16] R. I. Joseph and E. Schlömann, J. Appl. Phys., 36 (1965) 1579.

[17] J. Mrachkov and M. Kirov, Rev. Sci. Instrum., 62 (1991) 2469.

[18] E. M. Gyorgy, R. B. Van Dover, K. A. Jackson, L. F. Schneermeyer and J. V. Waszczak, Appl. Phys. Lett., 55 (1989) 283.

[19] F. Gomory, Supercond. Sci. Technol., 10(1997) 523 and references therein.

[20] T. Ishida and H. Mazaki, Phys. Rev. B, 20 (197) 131.

[21] H. Kupfer, I. Apfelstedt, W. Schauer, T. Wolf and H. W¨uhl, Physica C, 153–155 (1988) 367.

[22] K. H. Muller, Physica C, 168 (1990) 585.

[23] C. P. Bean, Phys. Rev. Lett., 8 (1962) 250.

[24] C. P. Bean, Rev. Mod. Phys., 36 (1964) 31.
[25] Y. B. Kim, C.F. Hempstead, A.R. Strnad, Phys. Rev., 129 (1963) 528.
[26] Y. B. Kim, Phys. Rev. Lett., 9 (1962) 306.
[27] E. H. Brandt, in: R. Nicolsky (Ed.), High Temperature Superconductivity, vol. 26, World Scientific, Singapore, 1996, p. 97.
[28] P. W. Anderson, Phys. Rev. Lett., 36 (1962) 309.
[28] J. R. Clem, Physica C, 153–155 (1988) 50.
[29] N. R. Werthamer, E. Helfand and P. C. Hohenberg,. Phys. Rev., 147 (1966) 295–302.
[30] C. C. Homes, A. Akrap, J. Wen, Z. Xu, Z. W. Lin, Q. Li and G. Gu, arXiv:1007.1447v2 (2010).
[31] C. Tarantini, A. Gurevic, J. Jaroszynski, F. Balakirev, E. Bellingeri, I. Pallecchi, C. Ferdeghini, B. Shen, H. H. Wen and D. C. Larbalestier, Phys. Rev. B, 84 (2011) 184522.
[32] J. Jaroszynski et al., Phys. Rev. B, 78 (2008) 174523.
[33] F. Hunte, J. Jaroszynski, A. Gurevich, D. C. Larbalestier, R. Jin, A. S. Sefat, M. A. McGuire, B. C. Sales, D. K. Christen and D. Mandrus, Nature, 453 (2008) 903.
[34]] M. Nikolo, R. B. Goldfarb, Phys. Rev. B, 39 (1989) 6615.
[35] R. Grissen, W. Hai-hu, A. J. J. van Dalen, B. Dam, J. Rector, H.G. Schnack, S. Libbrecht, E. Osquiguil, Y. Bruynseraede, Phys. Rev. Lett., 72 (1994) 1910.
[36] M. Polichetti, M. G. Adesso, T. Di Matteo, A. Vecchione, S. Pace, Physica C, 332 (2000) 378.
[37] M. Polichetti, M. G. Adesso, S. Pace, Physica C, 401 (2004) 196.
[38] G. Blatter et al., Rev. Mod. Phys., 66 (1994) 1125.
[39] R. B. Goldfarb, M. Lelental, C.A. Thompson, in: R.A. Hein, T.L. Francavilla, D.H. Liebenberg (Eds.), Magnetic Susceptibility of Superconductors and Other Spin
(Systems, Plenum, New York, 1991), p. 120-5 and references therein.
[41] S. Havriliak and S. Negami, J. Polym. Sci., C (1966) 14 99.
[42] Y. Lubashevsky, E. Lahoud, K. Chashka, D. Podolsky and A. Kanigel, Nature Physics,309 (2012) 312.
[43] D. X. Chen, C. Navau, N. Del Valle, A. Sanchez, Appl. Phys. Lett., 92 (2008) 202503.
[44] D. X. Chen, C. Navau, N. Del Valle, A. Sanchez, Physica C, 470 (2010) 89.
[45] J. Pearl, Appl. Phys. Lett., 5 (1964) 65.
[46] D. X. Chen, C. Navau, N. Del Valle, A. Sanchez, Supercond. Sci. Technol., 21 (2008) 105010.
[47] J. R. Thompson, Y. R. Sun, L. Civale, A. P. Malozemoff, M. W. McElfresh, A. D. Marwick, and F. Holtzberg, Phys. Rev. B, 47 (1993)14440.

[48] L. Miu and D. Miu, Supercond. Sci. Technol., 23 (2010) 025033.

[49] T. Taen, Y. Nakajima, T. Tamegai, and H. Kitamura, Phys. Rev. B, 86 (2012) 094527.

[50] Y. Sun, S. Pyon , T. Tamegai, R. Kobayashi, T. Watashige, K. S. Kasahara, Phys. Rev. B, 92 (2015) 144509.

[51] Y. Sun, T. Taen, Y. Tsuchiya, S. Pyon, Z. Shi, and T. Tamegai, Europhys. Lett., 103 (2013) 57013.

[52] E. K. Nazarova, A. J. Zaleski, K. A. Nenkov , A. L. Zahariev, Physica C, 468 (2008) 955–960.

[53] O. Brunner, L. Antognazza, J. M. Triscone, L. Mieville, O. Fischer, Phys. Rev. Lett., 67 (1991) 1354.

[54] X. Xu, L. Fu,L. Wang, Y. Zhang, F. Jun, X. Cao, K. Li, S. Hisashi, Phys. Rev. B, 59 (1999) 608.

[55] K. Buchkov, M. Polichetti, K. Nenkov, E. Nazarova, D. Mancusi, N. Balchev, D. Kovacheva, A. Zahariev and S. Pace, Supercond. Sci. Technol. 28, (2015) 035009.

[56] D. Mancusi, F. Giubileo, Y. Mizuguchi, S. Pace, M. Polichetti, Physica C 507 (2014) 47-54.

[57] D. Di Gioacchino, F. Celani, P. Tripodi, A.M. Testa, S. Pace, Phys. Rev. B, 59 (1999) 11539.

Conclusions

In this thesis, the development of a method for the analysis of the temperature dependent harmonics of the nonlinear AC magnetic response of a granular superconducting system, acquired by means of the AC susceptibility technique, has been presented. In fact, although the analysis of the AC magnetic response measured on a homogeneous type II superconducting system is most commonly used for the investigation of the superconducting properties and flux dynamics, particular attention may be given to the effects of demagnetizing fields in the case of superconducting granular systems. Since typically the temperature dependent fundamental and higher harmonics of the AC magnetic susceptibility of a superconducting sample are given by dividing the measured magnetization by the amplitudes of the applied field, deviations from the actual susceptibility may occur due to the existence of an effective temperature dependent magnetic field governing the magnetic response of the sample. In fact, this can occur both for a homogenous superconductor due to the demagnetizing factor of the sample and for granular systems due to the demagnetizing factors both of the whole sample and of the grains. This also results in the measurement of a field dependent critical current density which can influence the analysis.

That being said, we have first reviewed the principle of measurement of the AC magnetic susceptibility on homogeneous superconducting systems. In this cases, the existence of demagnetizing effects can be taken into account by applying a demagnetizing correction on the curves of the AC measured magnetization. In fact, after correcting the measured magnetization curves of type II superconductors, the curves can be analyzed within different models describing the mixed state of the materials in terms of thermally activated flux motion inside them. In particular, the analysis of the first harmonic curves of the AC susceptibility measured as function of temperature allows one to extract several superconducting parameters such as the critical current density, the superconducting upper critical fields and the activation energy over pinning barriers of vortices penetrating the sample. Moreover, when regarding the third harmonic curves of the AC susceptibility, detailed information about the actual flux dynamical regimes governing the sample magnetic response can be obtained by means of the comparison of the experimental curves with theoretical curves obtained for bulk samples and evidencing particular features related to the different flux dynamical regimes.

High-T_c and Fe-based superconducting materials reveal very adapt to be investigated by this kind of approach since their magnetic response is particularly leaded by thermally activated mechanisms. However, we have shown the results of the analysis of the AC magnetic response of a polycrystalline sample of the bismuth-oxysulfide layered

compound $Bi_4O_4S_3$ which exhibits several properties similar to the more recently discovered Fe-based superconductors due to their common layered crystal structure. In particular, we concentrate our first investigation on the $Bi_4O_4S_3$ sample since it also exhibits a high quality in terms of electromagnetic granularity.

In the second part of this dissertation we focused our attention on the development of a model for describing the magnetic response of a granular system, measured by means of the AC susceptibility technique, in terms of the magnetic contributions from the individual grains and from the intergranular contacts. This has been made by taking into account the existence of demagnetizing fields arising from both the whole sample and the grains, and the magnetic interaction between such fields. This may produce effective magnetic field inductions governing the inter- and intragranular magnetic responses and determined by the whole sample magnetization itself through the sample and grains demagnetizing factors. In particular, we found that the focusing of the magnetic field induction in the intergranular regions occurs due to the demagnetizing fields arising from the grains and depending on their geometric profile which determines the amount of stray fields outside the grains. This influences the magnetic response of the grains which contributes to the magnetization of the whole sample and then also affects the effective magnetic field induction on the sample's surface via the demagnetizing field.

All this allowed us to formulate a self consistent system of equations which can be solved by assuming different flux dynamical regimes governing the inter- and intragranular responses to the corresponding effective fields. The solutions of this system are the real and imaginary parts of the intrinsic AC susceptibilities first and higher harmonics of the two volume fractions. As an example, this kind of calculation has been performed starting from the magnetization measured on a $FeSe_{0.5}Te_{05}$ granular sample, whose intrinsic AC susceptibilities of the inter- and intragranular volume fractions have been determined together with the actual temperature dependences of the corresponding effective magnetic field inductions. Moreover, the temperature dependence of the flux relaxation times inside the sample given by both the effect of thermal activation and of the Lorentz force of the effective fields have been determined and give the actual flux dynamical regimes governing the inter- and intragranular magnetic responses.

All the calculations have been performed by means of a numerical programmed algorithm. The determination of the inter- and intragranular AC susceptibilities taking into account the existence of demagnetizing effects allowed us to the extract the actual superconducting parameters and flux dynamical information from the analysis of both the first and third harmonics, and to evaluate the demagnetizing fields effects on such estimations. In fact, within the developed method of analysis and the corresponding numerical algorithm, the critical current densities, upper critical fields and activation

energies for the inter- and intragranular volume fractions have been determined. From the comparison of these results with the results of the analysis performed without considering the existence of demagnetizing effects and then without separating the intrinsic magnetic contributions of the grains and of the intergranular regions in the whole sample magnetization, we found noteworthy deviations even for the grains geometry producing the least focusing of magnetic field in the intergranular regions. Moreover, we were able to exploit the superconducting properties of the grains and of the intergranular contacts separately which is not always possible starting from the total magnetic response and is very useful to investigate when the superconductivity is a bulk or granular mechanism. This suggests that demagnetizing fields can considerably affect the extraction of the superconducting and magnetic properties and flux dynamics information from the analysis of the AC magnetic response of a superconducting granular system, and that the proposed method could be used to both take these effects into account and to usefully separate the inter- and intragranular contributions to the magnetic response and their AC susceptibilities for a more detailed characterization.

Acknowledgments

I would like to express my great thanks to my supervisors Prof. Massimiliano Polichetti and Prof. Sandro Pace for leading and encouraging my scientific formation and research activities. I would also like to thank my coauthors in scientific publications and my colleagues for useful scientific discussions and collaborations.

A special thanks to my loved ones for supporting and encouraging me in job and private life.